TECHNISCHE UNIVERSITÄT MÜNCHEN

WALTHER-MEISSNER-INSTITUT

BAYERISCHE AKADEMIE DER WISSENSCHAFTEN

Superconducting Microwave Resonators for Spin-Based Quantum Memories

Master's thesis

Julian Franz

Supervisor: Priv.-Doz. Dr. Hans Huebl

Advisor: Patricia Oehrl

Garching – June 16, 2023

Abstract

Quantum information networks have recently made huge progress for quantum computation [1]. Quantum computers promise to be able to solve highly complex problems that conventional computers cannot [2]. To further enhance quantum computing, quantum memories are required to store and retrieve information [3]. Solid-state spin ensembles are promising candidates for quantum memories [4]. In this thesis, we focus on phosphorous donor spin ensembles in a silicon host matrix, which consist of an electronic spin with $S = \frac{1}{2}$ coupled via Fermi-contact hyperfine interaction to the $I = \frac{1}{2}$ nuclear spin of the phosphorous atom. Both spin species show exceptionally large coherence times of up to $10\,\mathrm{s}$ for the electron spins and $39\,\mathrm{min}$ for the nuclear spins embedded in isotopically purified ^{28}Si [5, 6]. The electron spin system in an external magnetic field can be manipulated by electron spin resonance (ESR) using the oscillating magnetic field B_1 of a planar superconducting lumped-element resonator [7]. Such a hybrid system exhibits frequency compatibility to quantum networks since the resonator operates in the microwave regime. We employ a novel chip design with NbTiN resonators that are coupled to a feedline in reflection geometry, thus theoretically exhibiting an increase in the signal-to-noise ratio by a factor of two compared to resonators coupled to transmission type feedlines [8, 9]. The behavior of the resonators is characterized under various conditions such as external magnetic fields and different temperatures. We then employ the resonators in ESR experiments on phosphorous dopants in natural silicon. We show continuous wave ESR measurements in the weak and strong coupling regimes and employ the Hahn-echo pulse sequence to demonstrate the storage of multiple microwave pulses in the spin system in pulsed ESR measurements [10, 11]. We measure an electron spin coherence time of $T_2 = 80\,\mu\mathrm{s}$ in natural silicon at liquid helium temperatures, which is comparable to similar samples [12]. Furthermore, we conceptually discuss how we could extend our hybrid system to be able to also address the nuclear spin system. By combining ESR and nuclear magnetic resonance (NMR), one can exploit the larger coherence times of the nuclear spins for quantum memory applications [13].

Contents

„Wer seine Lage erkannt hat,
wie soll der aufzuhalten sein?“

"Who can stop those,
who have realized their predicament"

Bertolt Brecht,
Lob der Dialektik (1934)

Chapter 1

Introduction

Quantum information and communication has recently made huge advancements up to the point, where large scale quantum networks can be envisioned [1]. In a smaller and more local framework, the research field of quantum computing aims to realize quantum computers, which promise to solve complex problems that super computers fail to [2]. In analogy to classical computation, memory units are a crucial part for enhancing quantum computation [3]. One branch of research focuses on solid-state spin ensembles as candidates for quantum memories. Such spin ensembles are addressed either optically or by usage of microwaves [14, 15].

A candidate for such a storage unit are phosphorous donors donors in silicon (Si:P) [4]. Donor spins in silicon can be used for storage [16]. Each phosphorous donor atom embedded in silicon provides an electron spin $S = \frac{1}{2}$ and nuclear spin $I = \frac{1}{2}$ system, which can be addressed for storage of quantum information. The spin systems of Si:P promises large coherence times, as values up to $10\,\mathrm{s}$ at $1.8\,\mathrm{K}$ for the electron spin and up to $39\,\mathrm{min}$ at room temperature for nuclear spin system have been reported [5, 6].

In order to store and read out information using phosphorous doped silicon, one can address the electron spins with pulsed electron spin resonance (ESR) in a magnetic field B_0. This is done by coupling the spin ensemble to a planar superconducting microwave resonator which provides the magnetic field B_1 to manipulate the spins [7]. This resulting hybrid system is suited for implementation in quantum networks as it provides frequency compatibility due to operating with frequencies in the microwave regime [17]. The usually employed microwave resonators made of either NbTiN or Nb represent lumped-element LC circuits that are capacitively coupled to and driven by a signal line in transmission geometry [9, 18]. However, planar superconducting microwave resonators that are coupled to a signal line in reflection geometry promise to increase the signal-to-noise ratio by a factor of two [8].

The hybrid system of a microwave resonator coupled to a solid-state spin ensemble is characterized by a variety of coupling rates and also the spin cooperativity. In order to reach the critical or strong coupling regime of the system, a profound understanding of the defining coupling and loss rates of resonator, spin ensemble and between the two is needed.

Additionally to ESR one can also practice nuclear magnetic resonance (NMR) with an additional device providing the magnetic field B_2 to further address the nuclear spins of Si:P [19]. By combining the two measurement techniques, the storage time is only limited by the large coherence time of the nuclear spins [13].

For this thesis, we focus on planar superconducting lumped-element microwave resonators and the applicability for ESR experiments using ^{nat}Si:P. We start with a discussion on the theoretical background necessary to understand the physical concepts included in this work. In particular, we consider general characteristics of the resonators and derive expressions for their complex scattering parameters when coupled to a transmission or reflection type feedline in the framework of input-output formalism [20]. We also present the solid-state spin ensemble of phosphorous doped silicon in terms of its spin states. The derivation of the system Hamiltonian in the Tavis-Cummings Model is shown to describe the hybrid system of microwave resonator and spin ensemble as two coupled quantum mechanical harmonic oscillators [21]. With this result, we also derive expressions for the scattering parameters of the hybrid system. In addition, the concept of kinetic inductance and two-level systems that limit the resonator performance under certain conditions are introduced. The thermal spin polarization, power dependent saturation behaviour of Si:P and the spin dynamics for ESR measurements are also discussed.

Subsequently, we focus on the experimental implementation of superconducting microwave resonators. To start with, we introduce simulations of the resonator characteristics based on CST microwave studio [22]. This includes a first impression of the scattering parameter, resonance frequency and generated B_1-field, which is of great interest as a driving field for ESR applications. Following that, we present the fabrication procedure of those resonators.

The following chapter is all about the characterization of the superconducting microwave resonators. We characterize the used NbTiN and Nb thin films in terms of critical temperature and width of transition by means of the Van-der-Pauw method before moving on with actual resonators [23]. We employ the capacitively shunted lumped element resonator design of [9] and highlight the differences when coupling these resonators to signal lines in reflection instead of transmission geometry. Furthermore, we characterize the performance of the resonators in terms of coupling rates and quality factors when exposed to variations of magnetic field, temperature and applied microwave power. Additionally, we show measurements of resonators with variations of geometric parameters and discuss their influence on the coupling rates of the resonators.

The application of the resonators in ESR experiments on phosphorous doped silicon is presented in the fifth chapter. Here, we first deal with continuous wave ESR and discuss measurements with resonators coupled to transmission and reflection type feedlines at liquid helium and millikelvin temperatures. We also deal with the influence of applied microwave power leading to saturation of the spin ensemble and a reduced collective coupling rate of the hybrid system. In the second part, we show pulsed ESR measurements with Hahn-echo sequences using a resonator coupled to a feedline in transmission geometry at liquid helium temperatures [10]. We demonstrate the storage of multiple microwave pulses and measure the spin coherence time of the applied phosphorous doped silicon sample.

In the sixth chapter, we theoretically discuss the addition of NMR to our hybrid system. The differences to ESR and a possible quantum memory pulse sequence are presented. Furthermore, we analyze different possibilities on how to experimentally implement NMR on our existing hybrid system. In particular, we present three different ways for the implementation of NMR experiments: an on-chip solution based on a planar RF coil, an additional air coil which one could put on top of the spin ensemble and a flip-chip solution using an additional chip for the application of the RF signal.

Finally, we summarize the outcomes of this thesis within the last chapter. Here, we give an overview of our results towards the realization of a storage unit based on solid-state spin ensembles. In addition, we present an outlook of this work, including ideas for further research.

Chapter 2

Theoretical Concepts

This chapter presents the physical concepts relevant for understanding the approaches and results of this thesis. Section 2.1.2 discusses superconducting microwave resonators in terms of characterizing properties, geometries, equations of motion and scattering parameters. Section 2.2 focuses on the properties of phosphorus donor spin ensembles hosted in a silicon crystal. The spin Hamiltonian with its eigenenergies and the Tavis-Cummings model are discussed. In section 2.3, the results of the first two parts are combined to describe the hybrid quantum system consisting of resonator coupled to spin ensemble in terms of scattering parameters. In the subsequent two sections, kinetic inductance and two-level systems that limit the performance of the resonators are introduced. Section 2.6 deals with the temperature dependent thermal spin polarization of the spin ensemble. Finally, the fundamental spin dynamics necessary for pulsed ESR experiments are presented.

2.1 Superconducting Microwave Resonators

2.1.1 Planar Lumped Element Resonators

In many electron spin resonance (ESR) experiments, manipulation of the spin states is realized by a microwave magnetic field $\vec{B}_1$ which is provided by microwave resonators. These resonantly amplify the driving magnetic field of a microwave source and focus it at the position of the sample to excite spins.

In general, microwave resonators are often realized as three-dimensional cavities [24]. These cavities provide the required boundary conditions to maintain a standing microwave magnetic field and are in particular advantageous when homogeneous microwave magnetic fields are required at the position of the sample [25, 26]. However, microwave cavities are not optimal, when investigating samples of small size as their dimensions are governed by the boundary conditions of the standing waves and the propagation speed of the electromagnetic waves, i.e. the speed of light. When not turning to alternative resonator designs, this results in very low filling factors and therefore typically poor sensitivities [27]. For samples as small as those studied in this work, planar microwave resonators offer a more suitable alternative. Resonators in planar geometries are oscillating LC circuits with the resonance frequency [28]

$$\omega_{\mathrm{r}} = \frac{1}{\sqrt{LC}}. \tag{2.1}$$

There exist various types of resonators in planar geometry, i.e. based on coplanar waveguides

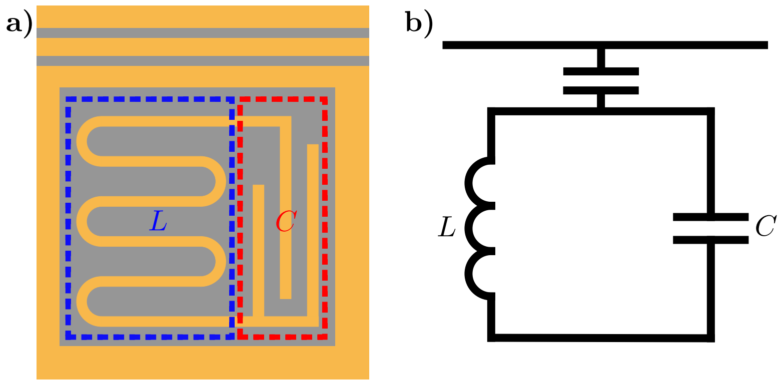

Figure 2.1.1: Schematics of the applied capacitively-shunted meander resonator. **a)**: Schematic of the resonator design consisting of a meander shaped inductance L and an interdigital capacitance C. It is coupled to a signal line. The superconducting material is shown in ochre and the silicon substrate is shown in grey. **b)**: Circuit diagram of the resonator on the left. It is a series LC circuit that is capacitively coupled to the signal line.

and based on lumped-elements. Conceptually, coplanar waveguide resonators (CPWRs) are the planar counterparts to cavities since they also represent standing wave resonators. They have capacitance C and inductance L continuously distributed over their whole length [29]. In this thesis, we employ lumped-element resonators (LER). In contrast to CPWRs, they have discrete L and C in elements called inductor and capacitor. This can result in compact resonator designs because it is releaved from geometric constraints originating from the boundary conditions of the standing waves. Different designs and variations of LERs have already been studied in ref. [9, 30] and many more. In this work, the design of choice is the capacitively-shunted meander resonator. This is schematically sketched in Figure 2.1.1 alongside its equivalent circuit diagram. It consists of a meandering inductor L and an interdigital capacitor C. As equation 2.1 implies, the resonance frequency can be tuned by adjusting the geometric parameters of these structures. This is mostly done by adjusting the capacitor in terms of number of branches and the length of the inner branch of the capacitor to keep the magnetic field generated by the inductor constant.

Planar microwave resonators are driven damped harmonic oscillators. An important quantity to describe the performance and the damping of these resonators is the dimensionless quality factor Q which is defined via [28]

$$Q = 2\pi \frac{\text{stored energy}}{\text{energy dissipated per period}}. \tag{2.2}$$

It is defined by the quotient of the energy stored in the resonator and the energy dissipated per oscillation period. The larger Q, the lower the damping of the resonator. In order to describe the system consisting of planar microwave resonator coupled to a feedline, the quality factors Q_{int}, Q_{ext} and Q_{tot} are introduced. The quality factor Q_{int} summarizes the intrinsic loss mechanisms of the resonator excluding effects related to the coupling into the electrical circuit used for the excitation and measurement of the microwave resonator. It characterizes internal losses that are of radiative, dielectric and resistive nature [25]. This quality factor is greatly increased by using superconducting materials, which minimizes resistive losses at low temperatures. Further enhancements can be achieved by optimizing material properties such as thin film quality. Q_{ext} describes the coupling of the resonator to the electric circuit. It represents losses that occur due to signal coupling out from the resonator into the feedline and can therefore be tuned by adjusting the coupling geometry. Finally, Q_{tot} is the so called total quality factor. It describes the whole system of resonator and feedline and is related to the other quality factors via

$$\frac{1}{Q_{\text{tot}}} = \frac{1}{Q_{\text{int}}} + \frac{1}{Q_{\text{ext}}}. \tag{2.3}$$

In the following, we refer to the total quality factor Q_{tot} as just Q. In this context, we also define the relative coupling rate g_{res} via

$$g_{\text{res}} = \frac{Q_{\text{int}}}{Q_{\text{ext}}}, \tag{2.4}$$

which allows to relate internal and external quality factor [25]. When $g_{\text{res}} < 1$ the resonator is "undercoupled" to the feedline whereas it is "overcoupled" to the feedline when $g_{\text{res}} > 1$. For the case $g_{\text{res}} = 1$, the resonator is "critically" coupled to the signal line. The resonators in this work are designed to operate in the strongly overcoupled regime, which implies $Q_{\text{int}} \gg Q_{\text{ext}}$. This ensures efficient coupling between feedline and resonator and make sure that resonator losses do not provide a dominant loss channel.

2.1.2 Derivation of Scattering Parameters

To characterize the microwave resonators, determine their resonance frequency, quality factors, and coupling constants, we measure the complex scattering parameter, also named S-parameter. To derive expressions for these S-parameters, a fundamental understanding of the equations of motion of the resonator-feedline system is required. The following procedure is closely orientated by the works of Greifenstein [31] and the one of Gardiner and Collett [32]. The formalism used here is the so called input-output formalism that was originally developed in the field of quantum optics [20].

The dynamics of a classical oscillating LC resonator can be described by either magnetic or electric field. While the magnetic field $B(t)$ is a real valued quantity, it is favorable to describe it with two complex quantities $\tilde{B}$ and $\tilde{B}^*$ via $B = \tilde{B} + \tilde{B}^*$. This makes the transition to the quantum regime more intuitive, where the quantum mechanical equivalent of these complex quantities is used. These are the annihilation and creation operators a and $a^\dagger$, respectively. These describe the excitation and relaxation of a photon in the resonator. Since they are connected to the magnetic field via $B \propto \left(a + a^\dagger\right)$, they are referred to as the resonator field in the following.

The Hamiltonian describing the whole system consisting of the resonator, the external bath of modes, and the interaction between the two is [32]

$$\mathcal{H}_{\text{sys}} = \underbrace{\hbar\omega_{\text{r}}\left(a^\dagger a + \frac{1}{2}\right)}_{\text{resonator}} + \underbrace{\int \hbar\omega b_\omega^\dagger b_\omega \,\mathrm{d}\omega}_{\text{external bath of modes}} \underbrace{- i\hbar \int g\left(\omega\right)\left(a^\dagger b_\omega - b_\omega^\dagger a\right)\mathrm{d}\omega}_{\text{interaction}}. \tag{2.5}$$

The first term describes the isolated resonator as a quantum mechanical harmonic oscillator.

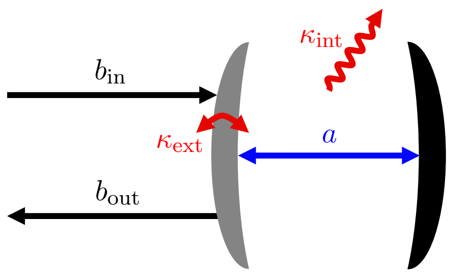

Figure 2.1.2: Schematic of a resonator that is directly coupled to an external bath of modes via a semitransparent mirror (grey). Incoming signal b_{in} can couple into the resonator via the coupling rate κ_{ext} and excite the resonator field a, which suffers from the internal loss rate κ_{int}. Signal can couple back out of the resonator and be detected as b_{out}.

The external bath of modes is described by the second term of the right hand side. Here, b_ω and $b_\omega^\dagger$ are the annihilation and creation operators of the electromagnetic field corresponding to the bath mode with frequency ω. The last term in the Hamiltonian of the system describes the interaction between resonator and the external bath of modes. This form of interaction is the most simplistic approach possible and is assumed to be linear in the field operators. The parameter $g(\omega)$ describes the frequency dependent coupling constant between the bath of modes and the resonator. The situation for the following general derivation is schematically shown in Figure 2.1.2 where a microwave resonator is directly coupled to an external bath of modes. The transition to the employed geometries for resonators coupled to a feedline is made at a later point.

For any operator A, its time evolution or equation of motion is given via the Heisenberg equation [33]

$$\dot{A} = \frac{i}{\hbar}\left[\mathcal{H}, A\right]. \tag{2.6}$$

In order to calculate the commutator in the equation above, the common commutation relations of the creation and annihilation operators are used. These commutation relations are

$$\left[b_\nu, b_\omega^\dagger\right] = \delta_{\nu\omega}, \tag{2.7}$$

$$\left[a, a^\dagger\right] = 1. \tag{2.8}$$

Applying equation (2.6) to the creation operators $b_\omega^\dagger$ and $a^\dagger$ results in [32]

$$\dot{b}_\omega^\dagger = i\omega b_\omega^\dagger + g(\omega)a^\dagger \tag{2.9}$$

$$\text{and} \quad \dot{a}^\dagger = i\omega_{\text{r}} a^\dagger - \int g(\omega) b_\omega^\dagger \mathrm{d}\omega, \tag{2.10}$$

respectively. In the following, the derivation is done by using the equations above for the creation operators, which is why for reasons of convenience, the dagger is omitted from these operators, which are denoted as b and a in the following. Assuming the signal to be sent in the past at a time $t_0 < 0$, the solution of equation (2.9) reads

$$b_\omega(t) = b_\omega(t_0)e^{i\omega(t-t_0)} + g(\omega)\int_{t_0}^{t} e^{i\omega(t-\tau)}a(\tau)\mathrm{d}\tau. \tag{2.11}$$

On the other side, assuming the outgoing signal is received by a detector in the future at a time $t_1 > 0$, the integrated solution of equation (2.9)

$$b_\omega(t) = b_\omega(t_1)e^{-i\omega(t_1-t)} - g(\omega)\int_{t}^{t_1} e^{i\omega(t-\tau)}a(\tau)\mathrm{d}\tau. \tag{2.12}$$

The two times corresponding to sending the incoming signal and receiving the outgoing signal t_0 and t_1 are set to occur far away from the time of the interaction, to prevent the propagating signal from coupling to the source or the detector. These points in time are therefore set to $t_0 \to -\infty$ and $t_1 \to +\infty$. In the following, both solutions are treated in parallel. Equations (2.11) and (2.12) are now plugged into equation (2.10) each. This yields the following expressions for the integral term in the two resulting equations for $\dot{a}$:

$$-\int g(\omega)b_\omega = -\int g(\omega)b_\omega(t_0)e^{i\omega(t-t_0)}\mathrm{d}\omega - \int g(\omega)^2\int_{t_0}^{t} e^{i\omega(t-\tau)}a(\tau)\mathrm{d}\tau\mathrm{d}\omega \tag{2.13}$$

$$\text{and} \quad -\int g(\omega)b_\omega = -\int g(\omega)b_\omega(t_1)e^{-i\omega(t_1-t)}\mathrm{d}\omega + \int g(\omega)^2\int_{t}^{t_1} e^{i\omega(t-\tau)}a(\tau)\mathrm{d}\tau\mathrm{d}\omega, \tag{2.14}$$

respectively. Now, the Markov approximation is deployed, which assumes the coupling constant for the interaction between external bath of modes and resonator to be independent of frequency [32]:

$$g(\omega) = g = \sqrt{\frac{2\kappa_{\text{ext}}}{2\pi}} = \text{const.} \tag{2.15}$$

κ_{ext} describes the transition rate of a photon between the external bath of modes and the resonator. It is also referred to as the external coupling rate of the resonator to its environment. This definition is identical for both feedline geometries that are later introduced, since the coupling mechanism is given by a notch port geometry in both cases. The expressions (2.13) and (2.14) can be further simplified by using the relations $\int \frac{\mathrm{d}\omega}{2\pi}e^{i\omega(x-x')} = \delta(x-x')$, $\int_{-\infty}^{x}\delta(x'-x)\mathrm{d}x' = \frac{1}{2}$ and the definitions for an input field b_{in} and an output field b_{out}:

$$b_{\text{in}}(t) = \frac{1}{\sqrt{2\pi}}\int e^{i\omega(t-t_0)}b_\omega(t_0)\mathrm{d}\omega \tag{2.16}$$

$$\text{and} \quad b_{\text{out}}(t) = \frac{1}{\sqrt{2\pi}}\int e^{i\omega(t-t_1)}b_\omega(t_1)\mathrm{d}\omega, \tag{2.17}$$

respectively. Equations (2.13) and (2.14) correspond to the external losses of the resonator and can be expressed for both solutions in terms of input and output field:

$$\left(\frac{\mathrm{d}}{\mathrm{d}t}a(t)\right)_{\text{ext}} = -\sqrt{2\kappa_{\text{ext}}}b_{\text{in}}(t) - \kappa_{\text{ext}}a(t) \tag{2.18}$$

$$\text{and} \quad \left(\frac{\mathrm{d}}{\mathrm{d}t}a(t)\right)_{\text{ext}} = -\sqrt{2\kappa_{\text{ext}}}b_{\text{in}}(t) + \kappa_{\text{ext}}a(t), \tag{2.19}$$

respectively. The terms proportional to input and output field describe the driving influence of the external bath of modes and the term proportional to the resonator field describes the dissipation of resonator photons into the external bath of modes. This model does not consider internal losses of the resonator, so they are taken into account by introducing the internal coupling rate κ_{int}, which describes the relaxation of the amplitude of the resonator field. The internal losses for both solutions are described by

$$\left(\frac{\mathrm{d}}{\mathrm{d}t}a(t)\right)_{\text{int}} = -\kappa_{\text{int}}a(t). \tag{2.20}$$

Consequently, all these steps result in two expressions for $\dot{a}$ in terms of the input field and the output field:

$$\dot{a} = i\omega_{\text{r}}a + (\kappa_{\text{ext}} - \kappa_{\text{int}})a - \sqrt{2\kappa_{\text{ext}}}b_{\text{out}}, \tag{2.21}$$

$$\dot{a} = i\omega_{\text{r}}a - \underbrace{(\kappa_{\text{ext}} + \kappa_{\text{int}})}_{=\kappa}a - \sqrt{2\kappa_{\text{ext}}}b_{\text{in}}. \tag{2.22}$$

Here, the total loss rate of the resonator $\kappa = \kappa_{\text{ext}} + \kappa_{\text{int}}$ is introduced as the sum of external and internal coupling rate. This coupling rate is defined to represent the half width at half maximum of the resonator peak in angular units.

Subtracting equation (2.22) from equation (2.21) yields the general boundary condition for the system

$$b_{\text{out}} = b_{\text{in}} + \sqrt{2\kappa_{\text{ext}}}a. \tag{2.23}$$

The different geometries applied in this thesis are not yet included in this derivation and will be described in the following. The resonator is coupled to a feedline by being placed in its vicinity as shown in Figure 2.1.1. This is called a notch port. A continuous signal line that is terminated by two ports leads to resonators in transmission geometry. These resonators are also called hanger type resonators. The other geometry has one end of the feedline terminated in open circuit geometry. This end reflects any signal back to the input port, therefore leading to reflection type resonators. These two geometries are shown in Figure 2.1.3.

For the case of a transmission feedline, that is shown in Figure 2.1.3 a), one measures the transmission scattering parameter S_{21} that is defined as

$$S_{21} = \frac{b_{\text{out}}^{(2)}}{b_{\text{in}}^{(1)}}, \tag{2.24}$$

with $b_{\text{in}}^{(1)}$ denoting the input field sent by port 1 and $b_{\text{out}}^{(2)}$ denoting the detected signal at port

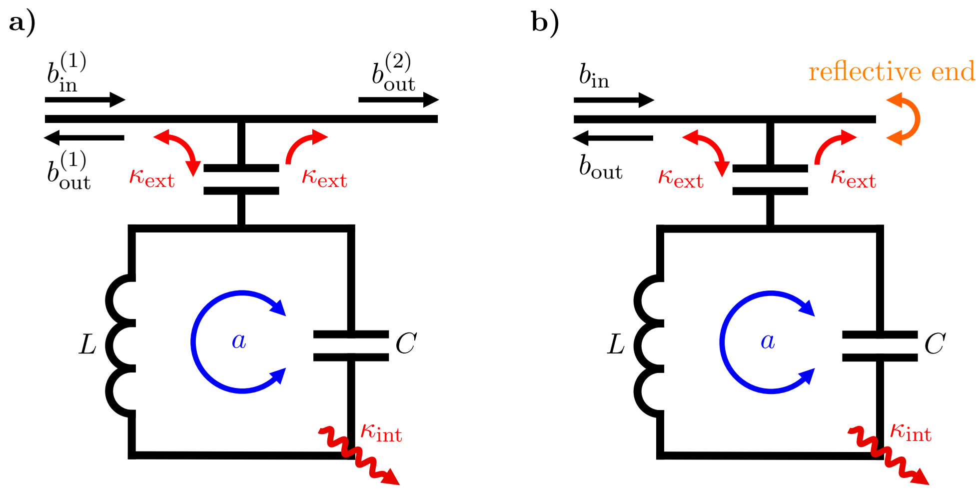

Figure 2.1.3: Schematics for a LER coupled to different feedline geometries. **a)** The resonator is coupled to a feedline in transmission geometry. The ends of the feedline are connected to the two ports 1 and 2. The incoming signal $b_{\text{in}}^{(1)}$ can couple to the resonator with the coupling rate κ_{ext} and excite a resonator field a, that is damped by the internal coupling rate κ_{int}. The resonator excitation can also couple back into the feedline and has two equal probable possibilities in which direction it propagates, back to port 1 as $b_{\text{out}}^{(1)}$ or towards port 2 as $b_{\text{out}}^{(2)}$. Only the latter is measured in transmission geometry. **b)** The resonator is coupled to the feedline in reflection geometry. The feedline is connected to only one port, which serves as signal source and detector simultaneously. Analogue to the case of transmission, the signal coupling back out of the resonator has two options concerning the direction of propagation.

2. Given the transmission geometry, it is evident that the signal coupling back out from the resonator into the feedline has two possibilities concerning the direction of propagation. It can propagate back to port 1, where it is not detected or it propagates to port 2 as part of $b_{\text{out}}^{(2)}$ and is actually measured. The probability for each direction is the same and therefore $\frac{1}{2}$. Taking this into account results in the modified boundary conditions for hanger type resonators

$$b_{\text{out}}^{(2)} = b_{\text{in}}^{(1)} + \frac{1}{2}\sqrt{2\kappa_{\text{ext}}}a, \tag{2.25}$$

$$b_{\text{out}}^{(1)} = \frac{1}{2}\sqrt{2\kappa_{\text{ext}}}a. \tag{2.26}$$

Plugging the new boundary condition into the expression for S_{21} does not yield an analytical result yet as it still contains the unknown resonator field a. To obtain an expression for the latter, the equation of motion (2.22) is solved in the frequency domain. Thus, we next consider the

Fourier transformation of the following operators:

$$a(t) = \frac{1}{\sqrt{2\pi}} \int e^{i\omega t} a(\omega) \mathrm{d}\omega, \tag{2.27}$$

$$b_{\text{in}}^{(1)}(t) = \frac{1}{\sqrt{2\pi}} \int e^{i\omega t} \underbrace{e^{-i\omega t_0} b_\omega(t_0)}_{=b_{\text{in}}(\omega)} \mathrm{d}\omega, \tag{2.28}$$

$$b_{\text{out}}^{(2)}(t) = \frac{1}{\sqrt{2\pi}} \int e^{i\omega t} \underbrace{e^{-i\omega t_1} b_\omega(t_1)}_{=b_{\text{out}}(\omega)} \mathrm{d}\omega. \tag{2.29}$$

Plugging these expressions into equation (2.22) results in the differential equation becoming completely algebraic:

$$i\omega a(\omega) = i\omega_{\text{r}} a(\omega) - \kappa a(\omega) - \sqrt{2\kappa_{\text{ext}}} b_{\text{in}}^{(1)}(\omega). \tag{2.30}$$

Rearranging this equation leads to an expression of the resonator field $a(\omega)$ in terms of $b_{\text{in}}^{(1)}$

$$a(\omega) = \frac{\sqrt{2\kappa_{\text{ext}}}}{i(\omega_{\text{r}} - \omega) - \kappa} b_{\text{in}}^{(1)}(\omega), \tag{2.31}$$

that is then plugged into the boundary condition in equation (2.25), which is subsequently divided by $b_{\text{in}}^{(1)}$ to yield the expression for S_{21} in transmission geometry:

$$S_{21}(\omega) = 1 + \frac{\kappa_{\text{ext}}}{i(\omega_{\text{r}} - \omega) - \kappa}. \tag{2.32}$$

The expression above can also be written in terms of quality factors. Any quality factor Q_{x} is linked to its corresponding coupling constant κ_{x} by the relation

$$Q_{\text{x}} = \frac{\omega_{\text{r}}}{2\kappa_{\text{x}}}. \tag{2.33}$$

One obtains

$$S_{21}(\omega) = 1 - \frac{\frac{Q}{Q_{\text{ext}}}}{1 + 2iQ\frac{(\omega - \omega_{\text{r}})}{\omega_{\text{r}}}}. \tag{2.34}$$

The expression above describes the ideal response of a resonator in transmission geometry. In reality, a variety of factors modify the measured response of the resonator and need to be taken into account to yield the correct results. According to [34], the introduction of an amplitude A, a phase shift α and an electronic delay τ accounts for cable losses. Additionally, one defines the external quality factor to be a complex quantity

$$Q_{\text{ext}} = |Q_{\text{ext}}| e^{-i\phi}. \tag{2.35}$$

With the additional phase ϕ, asymmetries of the resonator line shape due to impedance mismatches or similar effects are taken into account [35]. With these additions, equation (2.34) becomes the expression describing the real measured data best [34]

$$S_{21}(\omega) = \underbrace{Ae^{i\alpha}e^{-i\omega\tau}}_{\text{environment}} \underbrace{\left(1 - \frac{\frac{Q}{|Q_{\text{ext}}|}e^{i\phi}}{1 + 2iQ\frac{(\omega-\omega_{\text{r}})}{\omega_{\text{r}}}}\right)}_{\text{resonator}}. \tag{2.36}$$

Next, the derivation of the scattering parameter S_{11} for reflection type resonators is discussed:

$$S_{11} = \frac{b_{\text{out}}}{b_{\text{in}}}. \tag{2.37}$$

Since there is only one port, the indices in round brackets indicating the port number are omitted. The procedure for deriving S_{11} is completely analogue to the one of S_{21} for transmission geometry described above but with the different boundary condition given by equation (2.23). The ideal response described by the S_{11}-parameter is then

$$S_{11}(\omega) = 1 + \frac{2\kappa_{\text{ext}}}{i(\omega_{\text{r}} - \omega) - \kappa}, \tag{2.38}$$

and the result for S_{11} expressed in terms of quality factors and respecting measurement imperfections that describes real measurement data is given by

$$S_{21}(\omega) = \underbrace{Ae^{i\alpha}e^{-i\omega\tau}}_{\text{environment}} \underbrace{\left(1 - \frac{2\frac{Q}{|Q_{\text{ext}}|}e^{i\phi}}{1 + 2iQ\frac{(\omega-\omega_{\text{r}})}{\omega_{\text{r}}}}\right)}_{\text{resonator}}. \tag{2.39}$$

Comparing equation (2.36) with (2.39) yields the only difference being the factor 2 in the numerator of equation (2.39). The factor 2 in the resonator term indicates that resonators coupled to a feedline in reflection geometry offer a higher amplitude in the detected signal compared to the ones coupled to a transmission type feedline as used above [8].

2.2 Phosphorous Donor Spins in Silicon

The solid-state spin ensemble examined in this thesis is phosphorus donors in silicon. First, the spin Hamiltonian of this system and its energy levels are discussed. In the second part, the derivation of the Tavis-Cummings model is sketched, which yields a Hamiltonian describing the spin system coupled to a resonator for ESR experiments.

2.2.1 Spin Hamiltonian

When a phosphorous atom replaces a silicon atom in the lattice, the resulting defect acts as a donor providing an extra electron to the system. In the limit of low temperatures, the additional electron becomes localized at the donor atom and represents a $S = \frac{1}{2}$ system [36]. Additionally, phosphorous atoms only have one stable isotope ^{31}P which has a nuclear spin $I = \frac{1}{2}$. The spin

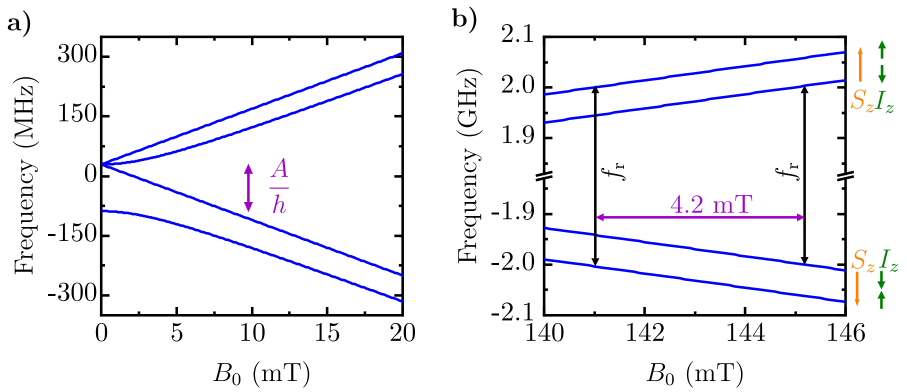

Figure 2.2.1: Breit-Rabi diagram of the energy levels of phosphorus donors in silicon plotted for different external magnetic fields B_0. **a)** Breit-Rabi diagram for low external magnetic fields. At zero field, the singlet and triplet states are split by $A/h = 117.53\,\mathrm{MHz}$. **b)** At larger magnetic fields, the four energy levels are linear with B_0. For a given driving frequency f_{res}, electron spin transitions are denoted with black arrows and are spaced by $4.2\,\mathrm{mT}$.

Hamiltonian for a single phosphorus donor in silicon with electron spin $\vec{S}$ and nuclear spin $\vec{I}$ in an external magnetic field $\vec{B}_0 = B_0\vec{e}_z$ reads [37]

$$\mathcal{H}_{\text{spin}} = \underbrace{\frac{g_{\mathrm{e}}\mu_{\mathrm{B}}}{\hbar}B_0 S_z}_{\text{electron Zeeman effect}} + \underbrace{\frac{g_{\mathrm{n}}\mu_{\mathrm{N}}}{\hbar}B_0 I_z}_{\text{nuclear Zeeman effect}} + \underbrace{\frac{A}{\hbar^2}\vec{S}\cdot\vec{I}}_{\text{hyperfine interaction}} \tag{2.40}$$

Here, $g_{\mathrm{e}} = 1.9985$ and $g_{\mathrm{n}} = 2.2632$ are the electron and nucleus Landé factors, respectively [36, 38], μ_{B} is the Bohr magneton, μ_{N} is the nuclear magneton and $A/h = 117.53\,\mathrm{MHz}$ is the hyperfine constant of phosphorus [36].

Solving the spin Hamiltonian for the eigenenergies yields four solutions, that correspond to singlet and triplet states. The eigenenergies are given by [39]:

$$E_1 = \frac{A}{4} + \frac{B_0}{2}\left(g_{\mathrm{e}}\mu_{\mathrm{B}} + g_{\mathrm{n}}\mu_{\mathrm{N}}\right), \tag{2.41}$$

$$E_2 = -\frac{A}{4} + \frac{1}{2}\sqrt{A^2 + B_0^2\left(g_{\mathrm{e}}\mu_{\mathrm{B}} - g_{\mathrm{n}}\mu_{\mathrm{N}}\right)^2}, \tag{2.42}$$

$$E_3 = \frac{A}{4} - \frac{B_0}{2}\left(g_{\mathrm{e}}\mu_{\mathrm{B}} + g_{\mathrm{n}}\mu_{\mathrm{N}}\right), \tag{2.43}$$

$$E_4 = -\frac{A}{4} - \frac{1}{2}\sqrt{A^2 + B_0^2\left(g_{\mathrm{e}}\mu_{\mathrm{B}} - g_{\mathrm{n}}\mu_{\mathrm{N}}\right)^2}. \tag{2.44}$$

The eigenfrequencies and their corresponding spin states are displayed in Breit-Rabi diagrams in Figure 2.2.1. The singlet and triplet states are separated by the hyperfine interaction A/h at zero magnetic field in Figure 2.2.1a). The three triplet states are degenerate. Their degeneracy is lifted in an external magnetic field B_0. As a consequence, the four eigenenergies split up in two groups of the same electron spin orientation. For larger fields as shown in Figure 2.2.1b), the energy levels behave linearly as a function of the field.

This region is of importance for electron spin resonance (ESR) experiments. Since the energy difference between levels with the same nuclear spin is in the range of few gigahertz, ESR-transitions of the electron spin can be driven with microwave resonator photons. Given a resonator with frequency f_r, there exists a magnetic field $B_{0,\mathrm{lf}}$ so that the energy difference between $|\downarrow, \Uparrow\rangle$ and $|\uparrow, \Uparrow\rangle$ state matches the energy of the resonator photon hf_r. This photon can be absorbed resonantly and flips the electron spin from down to up state. The same logic applies to the $|\Downarrow\rangle$ states at a higher field $B_{0,\mathrm{hf}}$ with the same resonator. The spacing between both fields of the transitions is $4.2\,\mathrm{mT}$. The indices "lf" and "hf" denote low field and high field transition.

In addition to the ESR-transitions, the goal is to drive nuclear magnetic resonance transitions (NMR) as well. The target frequencies of NMR transitions in the example of Figure 2.2.1b) are in the range of MHz and can therefore be driven by appropriate radio frequency (RF) magnetic fields.

2.2.2 The Tavis-Cummings Model

In this section, the derivation of an ESR Hamiltonian in the Tavis-Cummings model is discussed [21]. The Tavis-Cummings model describes the coupling of a harmonic oscillator or a mode to an ensemble of two-level systems. In certain approximations, the Tavis-Cummings model then can be interpreted as two coupled harmonic oscillators, where one of the oscillators represents the spin ensemble. To this end, the number of excitations in the spin ensemble m needs to be significantly smaller than the number of spins N participating. These N addressable spins result from an effective spin polarization of the whole spin system.

It was originally introduced to obtain a quantum electrodynamical description of molecules exposed to a resonant radiation field. The molecules are assumed to represent identical two-level systems (TLS). In the following derivation, the spins of phosphorous donors in silicon in an external magnetic field are modelled as TLSs. The radiation field is given by the resonator, whose photons are described by bosonic operators.

First, the case of a single spin coupled to a resonator is discussed by setting up the Jaynes-Cummings Hamiltonian, the transition to the ensemble follows later on [40]. The Hamiltonian describing the isolated systems of single spin and resonator without any interaction can be written as

$$\mathcal{H}_0 = \hbar\omega_\mathrm{r}\left(a^\dagger a + \frac{1}{2}\right) + \hbar\omega_\mathrm{s}\frac{\sigma_z}{2}. \tag{2.45}$$

Here, $a, a^\dagger$ are the bosonic resonator annihilation and creation operators, ω_r denotes the resonator frequency, ω_s describes the spin transition frequency and σ_z is the Pauli spin matrix of the z component. The resonator operators and the Pauli matrices commutate with each other and fulfill the following commutation relations:

$$[a, a^\dagger] = 1, \tag{2.46}$$

$$[\sigma_i, \sigma_k] = 2i\varepsilon_{ikl}\sigma_l. \tag{2.47}$$

The Hamiltonian $\mathcal{H}_\mathrm{int}$ describes the interaction between the magnetic field of the resonator $\vec{B}_1$

and the magnetic moment of the spin $\vec{\mu}_\mathrm{s}$ by

$$\mathcal{H}_\mathrm{int} = -\vec{\mu}_\mathrm{s} \cdot \vec{B}_1. \tag{2.48}$$

The interaction is reduced to the dominating dipole interaction term for simplicity. By using $\vec{S} = \frac{\hbar}{2}\vec{\sigma}$, one can express the magnetic moment of the spin $\vec{\mu}_\mathrm{s}$ as:

$$\vec{\mu}_\mathrm{s} = -g_\mathrm{e}\frac{\mu_\mathrm{B}}{\hbar}\vec{S} = -\frac{g_\mathrm{e}}{2}\mu_\mathrm{B}\vec{\sigma}, \tag{2.49}$$

where the components of $\vec{\sigma}$ are the pauli spin matrices. One can then define the magnetic field in the most simplistic approach as [41]

$$\vec{B}_1(\vec{r},t) = c(\vec{r})\left(a(t) + a^\dagger(t)\right) \cdot \vec{e}_x. \tag{2.50}$$

Here, $c(\vec{r})$ denotes the field amplitude normalized to the vacuum magnetic field of the resonator at the site of the spin. This polarization of the field is chosen since the transition dipole element for ESR is maximum for a microwave magnetic $\vec{B}_1$-field perpendicular to the static magnetic field $\vec{B}_0$ assumed to be aligned along the z-axis. The relevant component of the resonator field for the interaction has to be perpendicular to $\vec{B}_0$. All in all, the Hamiltonian describing the interaction can be written as:

$$\mathcal{H}_\mathrm{int} = -\vec{\mu}_\mathrm{s} \cdot \vec{B}_1 = \frac{g_\mathrm{e}}{2}\mu_\mathrm{B} c(\vec{r})\left(a + a^\dagger\right)\vec{\sigma} \cdot \vec{e}_x = \hbar g_\mathrm{s}\left(a + a^\dagger\right)\sigma_x. \tag{2.51}$$

The coupling rate to a single spin g_s is hereby introduced to conclude most of the constants, resulting in a more compact expression. Additionally, the Pauli spin matrix σ_x can be expressed in a more convenient way. To do so, the ladder operators σ_+, σ_- for raising and lowering the spin are introduced as

$$\sigma_\pm = \frac{1}{2}\left(\sigma_x \pm i\sigma_y\right) \tag{2.52}$$

and the interaction Hamiltonian is subsequently written as

$$\begin{aligned}\mathcal{H}_\mathrm{int} &= \hbar g_\mathrm{s}\left(a + a^\dagger\right)\underbrace{\left(\sigma_+ + \sigma_-\right)}_{=\sigma_x} \\ &= \hbar g_\mathrm{s}\left(a\sigma_+ + a\sigma_- + a^\dagger\sigma_+ + a^\dagger\sigma_-\right).\end{aligned} \tag{2.53}$$

This Hamiltonian can be simplified by applying the rotating wave approximation (RWA) [42]. Assuming $g_\mathrm{s} \ll \omega_\mathrm{r} + \omega_\mathrm{s}$, one can neglect the fast oscillating terms of the interaction Hamiltonian in the framework of RWA. It can be shown, that these terms are $\sigma_- a$ and $\sigma_+ a^\dagger$ in equation (2.53) [43]. The remaining terms describe the absorption of a resonator photon while exciting the spin and the inverse process.

Finally, the Hamiltonian of the Jaynes-Cummings model describing a resonator coupled to a single two-level spin system is obtained:

$$\mathcal{H}_{\text{JC, single}} = \hbar\omega_{\text{r}}\left(a^{\dagger}a + \frac{1}{2}\right) + \hbar\omega_{\text{s}}\frac{\sigma_z}{2} + \hbar g_{\text{s}}\left(\sigma_{+}a + \sigma_{-}a^{\dagger}\right) \tag{2.54}$$

Next, the transition to an ensemble of N spins is made and yields [43]

$$\mathcal{H}_{\text{JC}} = \hbar\omega_{\text{r}}\left(a^{\dagger}a + \frac{1}{2}\right) + \hbar\sum_{i=1}^{N}\omega_{\text{s},i}\frac{\sigma_{z,i}}{2} + \hbar\sum_{i=1}^{N}g_{\text{s},i}\left(\sigma_{+,i}a + \sigma_{-,i}a^{\dagger}\right). \tag{2.55}$$

In the following, the spin states of this Hamiltonian and its corresponding operators are discussed. As mentioned earlier, N spins are assumed to be polarized in the ground state and addressable. Furthermore, one can assume $\omega_{\text{s},i} = \omega_{\text{s}}$ and $g_{\text{s},i} = g_{\text{s}}$. Instead of describing each of the N polarized spins of the ensemble with its own set of Pauli spin matrices, it is beneficial to introduce a macroscopic spin J to collectively describe the spins. One therefore introduces the operators

$$J_z = \frac{1}{2}\sum_{i=1}^{N}\sigma_{z,i}, \tag{2.56}$$

$$J_{\pm} = \sum_{i=1}^{N}\sigma_{\pm,i} = J_x \pm iJ_y, \tag{2.57}$$

and simplifies the Jaynes-Cummings Hamiltonian to:

$$\mathcal{H}_{\text{JC}} = \hbar\omega_{\text{r}}\left(a^{\dagger}a + \frac{1}{2}\right) + \hbar\omega_{\text{s}}J_z + \hbar g_{\text{s}}\left(J_{+}a + J_{-}a^{\dagger}\right) \tag{2.58}$$

By assigning the macroscopic spin J to the ensemble, the states of the ensemble can be characterized with two quantum numbers: J for the total spin and M for the orientation of the z-component of J. This description is similar to the Zeeman effect of a single atom in an external magnetic field. A state of the spin ensemble is expressed as $|J, M\rangle$ with $J = 0, \ldots, \frac{N}{2}$ and $M = -J, \ldots, J$. J and M are either integer or half integer valued. The corresponding states are also referred to as Dicke states [44]. The ground state $|\downarrow \ldots \downarrow\rangle$ is consequently the Dicke state $\left|\frac{N}{2}, -\frac{N}{2}\right\rangle$. Applying the ladder operator J_+ to the ground state, which corresponds to adding an excitation to the system, yields the following:

$$J_{+}\left|\frac{N}{2}, -\frac{N}{2}\right\rangle = J_{+}\left|\downarrow \ldots \downarrow_i \ldots \downarrow\right\rangle = \sum_i \left|\downarrow \ldots \uparrow_i \ldots \downarrow\right\rangle \tag{2.59}$$

The expression above describes a single spin excitation that is delocalized over all spins of the system. It is evident, that these states show bosonic characteristics and that the operator J_+ is not normalized. Consequently, this operator and its counterparts can be expressed by a normalized set of operators $s, s^\dagger$ via

$$s = \frac{1}{\sqrt{N}} J_- \tag{2.60}$$

$$s^\dagger = \frac{1}{\sqrt{N}} J_+ \tag{2.61}$$

A better quantity than M to describe the excited spins of the ensemble is the number of excitations m, which is introduced as

$$m = M + \frac{N}{2},\ m = 0, 1, \ldots, N \tag{2.62}$$

For the next approximations, it is once again noted that the number of excitations m is significantly lower than the total number of polarized spins N, so $m \ll N$. Then, the characteristics of $s, s^\dagger$ are examined by using the following relations of the J operators:

$$[J_+, J_-] = 2J_z, \tag{2.63}$$

$$J_+ J_- |J, M\rangle = (J + M)(J - M + 1) |J, M\rangle, \tag{2.64}$$

$$J_z |J, M\rangle = M |J, M\rangle. \tag{2.65}$$

By expressing M in terms of m and using equation (2.64), the expectation value $\langle s^\dagger s\rangle$ can be approximated:

$$\begin{aligned}
\langle s^\dagger s\rangle &= \frac{1}{N} \left\langle \frac{N}{2}, m - \frac{N}{2} \right| J_+ J_- \left| \frac{N}{2}, m - \frac{N}{2} \right\rangle \\
&= \frac{1}{N} \left(\frac{N}{2} + m - \frac{N}{2} \right) \left(\frac{N}{2} - m + \frac{N}{2} + 1 \right) \\
&= \frac{1}{N} m \underbrace{(N - m + 1)}_{\approx N} \approx m
\end{aligned} \tag{2.66}$$

When looking at equation (2.65), it is evident that $\langle J_z \rangle = M$. Hence, J_z can be approximated by means of equation (2.66) as

$$J_z = m - \frac{N}{2} \approx s^\dagger s - \frac{N}{2}. \tag{2.67}$$

This result and equation 2.63 are used to also calculate the commutator

$$\left[s, s^\dagger \right] = \frac{1}{N} [J_-, J_+] = -\frac{2}{N} J_z = -\frac{2}{N} \left(m - \frac{N}{2} \right) \approx 1. \tag{2.68}$$

To conclude, the results obtained by equations (2.66) and (2.68) show that the operators $s, s^\dagger$ correspond to bosonic annihilation and creation operators of a quantum mechanical harmonic oscillator for $m \ll N$.

One can rewrite the Jaynes-Cummings Hamiltonian from equation (2.58) and derive the Tavis-

Cummings Hamiltonian [21]:

$$\mathcal{H}_{\mathrm{TC}} = \underbrace{\hbar\omega_{\mathrm{r}}\left(a^{\dagger}a + \frac{1}{2}\right)}_{\text{resonator}} + \underbrace{\hbar\omega_{\mathrm{s}}\left(s^{\dagger}s - \frac{N}{2}\right)}_{\text{spin ensemble}} + \underbrace{\hbar g_{\mathrm{s}}\sqrt{N}\left(s^{\dagger}a + sa^{\dagger}\right)}_{\text{interaction}} \tag{2.69}$$

This rather simple model describes two interacting harmonic oscillators.

Eventually, this derivation showed that the spin ensemble can be modelled as a harmonic oscillator with an energy offset under the condition $m \ll N$. This condition is also called the Holstein-Primakoff approximation [45]. By using an ensemble of N spins instead of a single one, the effective coupling rate $g_{\mathrm{eff}} = g_{\mathrm{s}}\sqrt{N}$ is enhanced by a factor of $\sqrt{N}$. This is due to collective excitations which are shared by all spins as described by the Dicke states.

2.3 Hybrid Quantum System

The system of a driven resonator coupled to a solid-state spin ensemble is also called a hybrid quantum system due to the coupling dynamics. The derivation of the S-parameters for such a hybrid quantum system follows the logic described in Chapter 2.1.2. As derived in the previous section, the starting point is the Tavis-Cummings Hamiltonian for the case of few excitations [46]:

$$\mathcal{H}_{\mathrm{TC}} = \underbrace{\hbar\omega_{\mathrm{r}}\left(a^{\dagger}a + \frac{1}{2}\right)}_{\text{resonator}} + \underbrace{\hbar\omega_{\mathrm{s}}\left(s^{\dagger}s - \frac{N}{2}\right)}_{\text{spin-ensemble}} + \underbrace{\hbar g_{\mathrm{eff}}\left(s^{\dagger}a + a^{\dagger}s\right)}_{\text{interaction}} \tag{2.70}$$

The spin system is hereby modelled as a quantum mechanical harmonic oscillator with eigenfrequency ω_{s} and the creation and annihilation operators $s^{\dagger}, s$. These operators fulfill the commutation relation $\left[s, s^{\dagger}\right] = 1$ and commutate with the operators of the resonator. The effective coupling rate g_{eff} is related to the coupling rate of a single spin g_{s} via $g_{\mathrm{eff}} = g_{\mathrm{s}}\sqrt{N}$, where N is the total number of spins and the coupling rate to each spin is assumed to be the same. As derived in [9], one can also write $g_{\mathrm{eff}} = \frac{g_{\mathrm{s}}\mu_{\mathrm{B}}}{2\hbar}\sqrt{\frac{1}{2}\mu_0\hbar\omega_{\mathrm{r}}\rho P(T)V\nu}$, where ρ is the spin density, $P(T)$ is the thermal polarization of the spins, V is the volume of the ensemble and ν is the filling factor, which was already mentioned in the beginning of this chapter. Applying equation (2.6) to the operators $s^{\dagger}$ and $a^{\dagger}$ and omitting the dagger signs again for convenience yields the equations of motion

$$\dot{s} = i\omega_{\mathrm{s}}s + ig_{\mathrm{eff}}a, \tag{2.71}$$

$$\dot{a} = i\omega_{\mathrm{r}}a + ig_{\mathrm{eff}}s. \tag{2.72}$$

The spins do not stay excited and relax with time. To account for that, a term with the spin relaxation rate γ_{s} is introduced

$$\left(\frac{\mathrm{d}}{\mathrm{d}t}s\right)_{\text{relaxation}} = -\gamma_{\mathrm{s}}s. \tag{2.73}$$

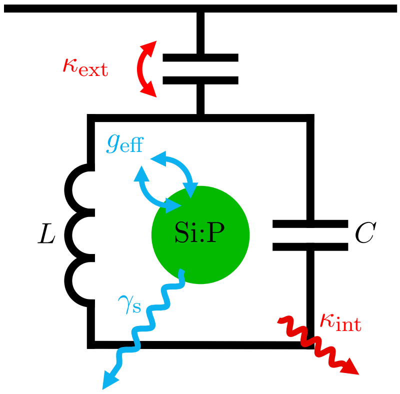

Figure 2.3.1: Schematic of a LER coupled to a spin ensemble. The resonator is coupled to the feedline at a rate $\kappa_{\rm ext}$ and suffers from internal losses described by the loss rate $\kappa_{\rm int}$. The coupling rate between resonator and spin ensemble (here: Si:P, depicted in green) is given by $g_{\rm eff}$. The spin sytem itself also suffers internal losses, which are described by a spin relaxation rate $\gamma_{\rm s}$.

Consequently, the loss term and the driving term of the resonator-bath system from equation (2.22) are added to equation (2.72) to receive the equation of motions

$$\dot{s} = i\omega_{\rm s}s - \gamma_{\rm s}s + ig_{\rm eff}a, \tag{2.74}$$
$$\dot{a} = i\omega_{\rm r}a - \kappa a + ig_{\rm eff}s - \sqrt{2\kappa_{\rm ext}}b_{\rm in}. \tag{2.75}$$

The situation is visualized in Figure 2.3.1. With the Fourier transformations from equations (2.27), (2.28) and an analogue expression for s, one obtains the equations above in the frequency domain

$$i\omega s(\omega) = i\omega_{\rm s}s(\omega) - \gamma_{\rm s}s(\omega) + ig_{\rm eff}a(\omega), \tag{2.76}$$
$$i\omega a(\omega) = i\omega_{\rm r}a(\omega) - \kappa a(\omega) + ig_{\rm eff}s(\omega) - \sqrt{2\kappa_{\rm ext}}b_{\rm in}(\omega). \tag{2.77}$$

Equation (2.76) is solved for the spin operator s

$$s(\omega) = \frac{ig_{\rm eff}}{i(\omega - \omega_{\rm s}) + \gamma_{\rm s}}a(\omega), \tag{2.78}$$

which is then plugged into equation (2.77):

$$a(\omega) = \frac{\sqrt{2\kappa_{\rm ext}}}{i(\omega_{\rm r} - \omega) - \kappa + \frac{g_{\rm eff}^2}{i(\omega_{\rm s}-\omega)-\gamma_{\rm s}}}b_{\rm in}(\omega) \tag{2.79}$$

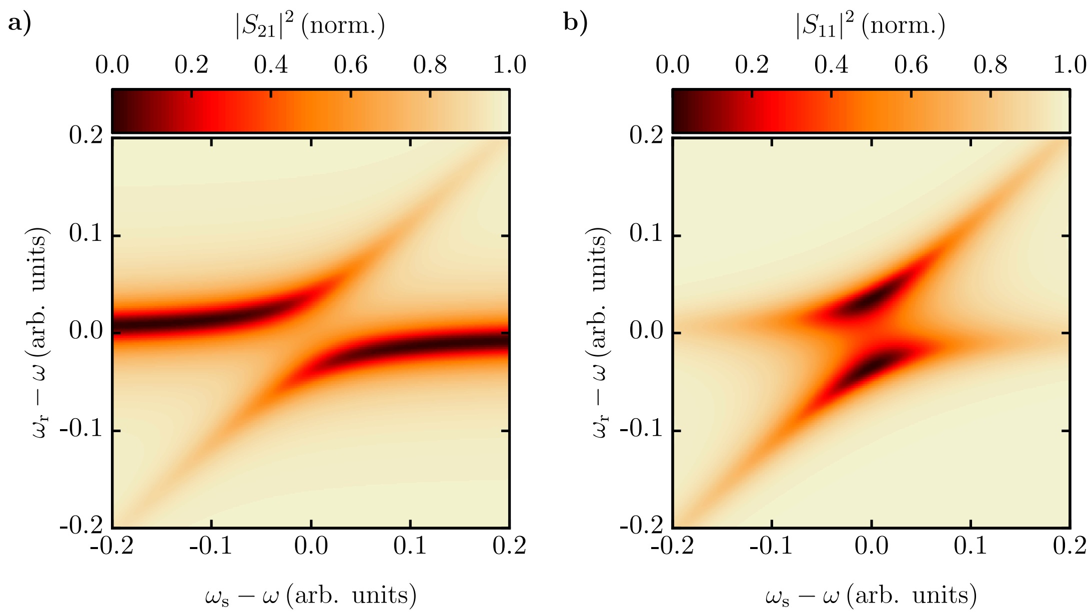

Figure 2.3.2: Simulated data of the absolute value squared of **a)** equation (2.80) and **b)** equation 2.81. The simulated $|S_{xx}|^2$ data is normalized for good contrast. The simulation is run with the dimensionless parameters $\omega_\mathrm{r} = 1$, $\kappa = \kappa_\mathrm{ext} = \gamma_\mathrm{s} = 0.02$ and $g_\mathrm{eff} = 0.04$. When the driving frequency ω approaches both ω_r and ω_s, an avoided crossing is observed. In this case of hybridization, the Lorentian gets broadened due to the additional loss channel of coupling to the spin ensemble.

Since it is assumed, that the spin ensemble cannot be excited by the feedline, the boundary equations (2.25) and (2.23) for transmission and reflection geometry are still valid. For transmission:

$$S_{21}(\omega) = 1 + \frac{\kappa_\mathrm{ext}}{i(\omega_\mathrm{r} - \omega) - \kappa + \frac{g_\mathrm{eff}^2}{i(\omega_\mathrm{s} - \omega) - \gamma_\mathrm{s}}}. \tag{2.80}$$

For reflection:

$$S_{11}(\omega) = 1 + \frac{2\kappa_\mathrm{ext}}{i(\omega_\mathrm{r} - \omega) - \kappa + \frac{g_\mathrm{eff}^2}{i(\omega_\mathrm{s} - \omega) - \gamma_\mathrm{s}}}. \tag{2.81}$$

The corresponding signature of hybridization between resonator and spin system described by an avoided crossing is simulated and visualized in Figure 2.3.2 for transmission and reflection geometry. Near ω_s, the Lorentian signature of the resonator gets broadened and splits up into a lower and an upper branch, thus showing an avoided crossing. The broadening is due to the coupling to the spin system that can be interpreted as an additional loss channel from the point of view of the resonator. When comparing the simulated data of the two geometries, one can see that the depth of the Lorentian dip is rather constant for transmission geometry whereas for reflection geometry, it becomes deeper when approaching the region of hybridization.

To characterize the coupling between resonator and spin system, the so called spin cooperativity C is introduced as

$$C = \frac{g_{\text{eff}}^2}{\kappa\gamma_{\text{s}}}. \tag{2.82}$$

Three cases of coupling regimes can be distinguished:

1. $C < 1$: Weak coupling regime. The loss rates dominate the coupling rate between resonator and spin ensemble.
2. $C = 1$: Critical coupling. The coupling rates are very similar.
3. $C > 1$: Strong coupling regime. The effective coupling rate between resonator and spin ensemble outweighs the loss rates. Information is efficiently exchanged between resonator and spin ensemble.

For the goal of realizing a quantum memory, the system should operate in the critical to strong coupling regime $C \geq 1$ to ensure efficient transfer of information between feedline, resonator and solid-state spin ensemble. This regime can also be expressed by $g_{\text{eff}} \gg \kappa, \gamma_{\text{s}}$ [13].

2.4 Kinetic Inductance

The energy of an electric current I in an electrical conductor is described by two terms. First, there is a term summarizing the self-inductance of the current caused by its own magnetic field. This contribution is caused by the geometry of the conductor. The other term takes the kinetic energy into account caused by the non-zero inertial mass of the charge carriers. Consequently, the energy E of a homogeneous superconductor of length l, cross section A and uniform current density is given by [47]:

$$E = \underbrace{\frac{1}{2}L_{\text{g}}I^2}_{\text{geometric term}} + \underbrace{\frac{1}{2}\left[\frac{m_{\text{e}}}{n_{\text{s}}e^2} \cdot \frac{l}{A}\right]I^2}_{\text{kinetic term}}. \tag{2.83}$$

Here, L_{g} denotes the geometric inductance, m_{e} is the electron mass, n_{s} is the density of the cooper pairs and e is the elementary charge. The term in parenthesis is summarized to the kinetic inductance

$$L_{\text{k}} = \frac{m_{\text{e}}}{n_{\text{s}}e^2} \cdot \frac{l}{A} = \frac{\mu_0\lambda_{\text{L}}^2 l}{A}, \tag{2.84}$$

which can also be expressed in terms of the London penetration depth $\lambda_{\text{L}} = \sqrt{\frac{m_{\text{e}}}{\mu_0 n_{\text{s}} e^2}}$ [48]. L_k depends on the external magnetic field B_0 as well as the temperature T due to λ_{L}. As a consequence, the resonance frequency of a superconducting microwave resonator also inherits this dependence via:

$$f_{\text{r}}(B_0, T) = \frac{1}{2\pi\sqrt{L(B_0, T) \cdot C}} = \frac{1}{2\pi\sqrt{(L_{\text{g}} + L_{\text{k}}(B_0, T)) \cdot C}}, \tag{2.85}$$

where L_{g} is assumed to be independent of magnetic field and temperature due to originating purely from the geometry. Based on this relation above, the resonance frequency is expected to shift due to the changes of kinetic inductance under the influence of magnetic field and temperature. However, these shifts tend to be rather small as can be seen in the measurements later on. It is therefore assumed in analogy to Ref. [30]

$$L_\mathrm{k}(B_0,T) - L_\mathrm{k}(0,0) \ll L_\mathrm{g} + L_\mathrm{k}(0,0) \text{ for } B_0 \ll B_\mathrm{c},\ T \ll T_\mathrm{c}. \tag{2.86}$$

The relative shift in resonance frequency can be written as:

$$\begin{aligned}\frac{f_\mathrm{r}(B_0,T) - f_\mathrm{r}(0,0)}{f_\mathrm{r}(0,0)} &= \sqrt{\frac{L_\mathrm{g} + L_\mathrm{k}(0,0)}{L_\mathrm{g} + L_\mathrm{k}(B_0,T)}} - 1 = \sqrt{\frac{1}{1 + \frac{L_\mathrm{k}(B_0,T) - L_\mathrm{k}(0,0)}{L_\mathrm{g} + L_\mathrm{k}(0,0)}}} - 1 \\ &\approx -\frac{1}{2}\frac{L_\mathrm{k}(B_0,T) - L_\mathrm{k}(0,0)}{L_\mathrm{g} + L_\mathrm{k}(0,0)} \\ &= \frac{1}{2}\frac{L_\mathrm{k}(0,0)}{L_\mathrm{g} + L_\mathrm{k}(0,0)}\left(1 - \frac{L_\mathrm{k}(B_0,T)}{L_\mathrm{k}(0,0)}\right).\end{aligned} \tag{2.87}$$

Here, the expansion

$$\sqrt{\frac{1}{1+x}} \approx 1 - \frac{1}{2}x + \mathcal{O}(x^2), \tag{2.88}$$

for $x \ll 1$ given by the assumption of equation (2.86) is applied. The expression of equation (2.87) is rewritten by defining the ratio of kinetic inductance to total inductance as:

$$\alpha = \frac{L_\mathrm{k}(0,0)}{L_\mathrm{g} + L_\mathrm{k}(0,0)}, \tag{2.89}$$

and plugging in equation (2.84) yields the resonance frequency shift of the resonator due to changes in L_k:

$$\frac{f_\mathrm{r}(B_0,T) - f_\mathrm{r}(0,0)}{f_\mathrm{r}(0,0)} = \frac{\alpha}{2}\left(1 - \frac{\lambda_\mathrm{L}^2(B_0,T)}{\lambda_\mathrm{L}^2(0,0)}\right). \tag{2.90}$$

Magnetic Field Dependency Since the used materials NbTiN and Nb both represent s-wave superconductors [49, 50], the effective London penetration depth λ_L as a function of the magnetic field can be described by [51]:

$$\frac{1}{\lambda_\mathrm{L}(B_0)} = \frac{1}{\lambda_\mathrm{L}(0)}\left\{1 - \frac{3}{4}\beta(T)\left(\frac{B_0}{B^*}\right)^2\right\}. \tag{2.91}$$

Here, $\beta(T)$ is a non-linear and temperature dependent function, which can be treated as a constant due to the measurements being done at constant temperatures, and B^* is a characteristic field in the order of the thermodynamic critical field. The relation above describes the increase in magnetic penetration depth due to the pair-breaking effect caused by B_0.

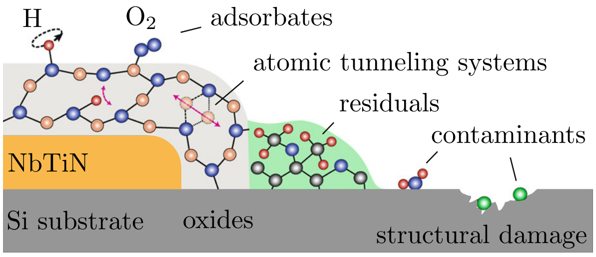

Figure 2.5.1: Schematic of different sources of TLS. In addition to atomic tunneling systems in the naturally occurring oxide layer, contaminants, residuals of e-beam resist and structural damage provide TLS in form of surface defects. Adsorbates such as H and O_2 provide surface spins which also act as TLS. Adapted from [52].

Plugging this expression into the master equation (2.90) results in:

$$\frac{f_\mathrm{r}(B_0) - f_\mathrm{r}(0)}{f_\mathrm{r}(0)} = \frac{\alpha}{2}\left\{1 - \frac{1}{\left(1 - \frac{3}{4}\beta\left(\frac{B_0}{B^*}\right)^2\right)^2}\right\}, \tag{2.92}$$

Temperature Dependency The temperature dependence of λ_L in the frequency shift is well described by the empirical Gorter-Casimir model [48]:

$$\lambda_\mathrm{L}(T) = \frac{\lambda_\mathrm{L}(0)}{\sqrt{1 - \left(\frac{T}{T_c}\right)^4}}, \tag{2.93}$$

where T_c is the critical temperature. An expression for the temperature dependent frequency shift due to changes in kinetic inductance is obtained by plugging the equation above into (2.90):

$$\frac{f_\mathrm{r}(B_0, T) - f_\mathrm{r}(0,0)}{f_\mathrm{r}(0,0)} = \frac{\alpha}{2}\left(1 - \frac{1}{1 - \left(\frac{T}{T_c}\right)^4}\right), \tag{2.94}$$

2.5 Two-Level Systems

At very low powers and temperatures, the performance of superconducting quantum devices such as resonators are limited by quantum two-level systems (TLS), which are unsaturated in this regime [52–55]. TLS occur in amorphous matter, surface defects, adsorbates providing surface spins, the different interfaces and other surface impurities. An overview of sources of TLS is given in Figure 2.5.1. Although the detailed nature of TLS is still not perfectly understood up to now, we want to briefly sketch the most prominent source of TLS and the corresponding model to understand the mechanism affecting the resonators.

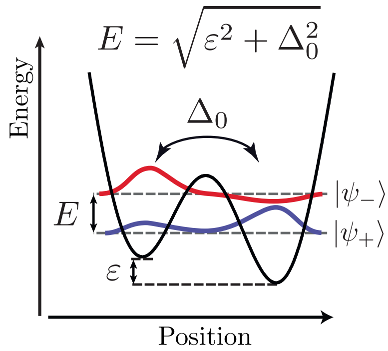

Figure 2.5.2: Double-well potential modelling the different positions of TLS atom in the standard tunneling model (STM). The two eigenstates $|\psi_\pm\rangle$ are separated by the energy E, which depends on the asymmetry energy ε and the tunneling barrier between the two minima Δ_0. Picture taken from [53].

In amorphous matter, such as in oxide layers on top of the superconducting material and the substrate, atoms that can occupy two different locations in the bulk provide the most prominent kind of TLS [53]. They are described with the so-called standard tunneling model (STM), which models the two different locations or levels of the atom as minima in an mostly asymmetric double-well potential, as shown in Figure 2.5.2. In this model, the atom is always in either one of the two configurations. In general, these TLS are saturated and do not influence the resonator. However, at very low temperatures in the millikelvin regime, the TLS cannot be thermally excited anymore and the saturation of the system vanishes. A change of position then is only possible via tunneling. In this regime, the system can couple to the electric field. Due to a large variety of TLS with different heights of tunnel barriers and energy differences, there always exist TLS that match the resonance frequency, therefore acting as an additional loss channel to the resonators by absorbing resonator photons.

Temperature Dependency The temperature dependent influence of TLS on the performance of superconducting microwave resonators is decribed by the model of [54]. This model deals with TLS that have large detunings to the resonance frequency f_r of the resonator. Since one can measure this temperature dependent behavior at high power, resonant TLS are saturated. In this framework, the internal quality factor is described by:

$$\frac{1}{Q_\mathrm{int}} = \frac{1}{Q_\mathrm{TLS}} \tanh\left(\frac{hf_\mathrm{r}(T)}{2k_\mathrm{B}T}\right) + \frac{1}{Q^*}, \tag{2.95}$$

where an offset $\frac{1}{Q^*}$ is added in analogy to [56]. Here Q_TLS denotes the temperature independent quality factor describing the TLS. The $\tanh$ function acts as a weighting factor for the influence of Q_TLS. Finally, Q^* accounts for non-TLS contributions to the internal quality factor.

The shift in resonance frequency of the resonator caused by TLS is given by [54]:

$$\Delta f_{\mathrm{r}}(T) = \frac{1}{\pi Q_{\mathrm{TLS}}}\left[\operatorname{Re}\Psi\left(\frac{1}{2}+\frac{hf_{\mathrm{r}}(T)}{2\pi i k_{\mathrm{B}}T}\right)-\ln\left(\frac{hf_{\mathrm{r}}(T)}{2\pi k_{\mathrm{B}}T}\right)\right]f_{\mathrm{r}}(0), \tag{2.96}$$

where Ψ denotes the digamma function.

Power Dependency The power dependent influence of TLS on the internal quality factor is described by [18, 56]:

$$\frac{1}{Q_{\mathrm{int}}} = \frac{1}{Q_{\mathrm{TLS}}}\left(1+\frac{\langle n_{\mathrm{ph}}\rangle}{\langle n_{\mathrm{c}}\rangle}\right)^{-\nu}+\frac{1}{Q^*}, \tag{2.97}$$

where $\langle n_{\mathrm{ph}}\rangle$ is the mean photon number of the resonator, Q_{TLS} denotes the quality factor of the TLS and Q^* summarizes non-TLS contributions to Q_{int}. The critical photon number above which the TLS are considered fully saturated is given by $\langle n_{\mathrm{c}}\rangle$ in the expression above. The exponent ν indicates deviations from the standard TLS model in which its value is 0.5.

2.6 Thermal Spin Polarization

The quantity describing the fraction of spins that are addressable for ESR is the thermal spin polarization $0 < P(T) < 1$. An expression for this can be derived using statistical physics and the eigenenergies of the four levels that we presented in Chapter 2.2.1 [57]. The probability that a state with energy $E_i(B_0)$ is occupied at a temperature T is given by [58]:

$$p_i(T, B_0) = \frac{\exp\left\{-\frac{E_i(B_0)}{k_{\mathrm{B}}T}\right\}}{Z(T, B_0)}, \tag{2.98}$$

where k_{B} is the Boltzmann constant and $Z(T, B_0)$ is the canonical partition function defined as:

$$Z(T, B_0) = \sum_{i=1}^{4}\exp\left\{-\frac{E_i(B_0)}{k_{\mathrm{B}}T}\right\}. \tag{2.99}$$

The thermal spin polarization of the low field transition ($E_4(B_0) \to E_1(B_0)$) and the high field transition ($E_3(B_0) \to E_2(B_0)$) then are:

$$P_{\mathrm{lf}}(T, B_0) = |p_1(T, B_0) - p_4(T, B_0)| \text{ and} \tag{2.100}$$

$$P_{\mathrm{hf}}(T, B_0) = |p_2(T, B_0) - p_3(T, B_0)|, \tag{2.101}$$

respectively. The thermal spin polarizations are visualized for different temperatures and a given magnetic field $B_0 = 180\,\mathrm{mT}$ in figure 2.6.1. Coming from high temperatures, both polarizations increase with decreasing temperature. However, below $0.1\,\mathrm{K}$ the curves show contrary behaviour. The one of the low field transition increases further until reaching complete polarization whereas the one of the high field transition decreases until vanishing completely. This is due to the fact that the the spin states with energy E_3 become less probable to be populated in

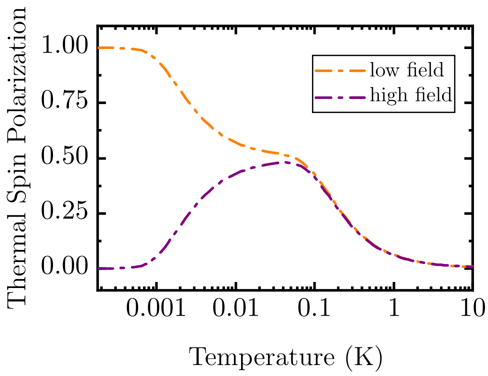

Figure 2.6.1: Thermal spin polarization of the low and high field transitions of phosphorous donors in silicon as a function of temperature for a magnetic field $B_0 = 180\,\mathrm{mT}$. The spin polarization increases with decreasing temperature. Below $0.1\,\mathrm{K}$, the polarization of the low field transition increases further whereas the one of the high field transition decreases due to the state with E_3 being less populated.

contrast to the state with the lowest energy E_4.

2.7 cwESR Power Saturation

A saturating behaviour of the spin ensemble is expected at sufficiently high incident microwave powers at the sample. For a general undriven $S = \frac{1}{2}$ spin system consisting of N spins exposed to a background magnetic field B_0, N_- spins are in the $|\downarrow\rangle$ state and $N_+ = N - N_-$ are in the $|\uparrow\rangle$ state. At a temperature T, the ratio between N_-/N_+ is given by a Boltzmann factor [59]:

$$\frac{N_-}{N_+} = \exp\left(\frac{g\mu_\mathrm{B} B_0}{k_\mathrm{B} T}\right). \tag{2.102}$$

The lower the temperature T and the higher the magnetic field B_0, the more spins are in the $|\downarrow\rangle$ state.

In order for the spin system to be able to absorb resonator photons, $N_- > N_+$ is required. Contrary to the excitation of the spins through absorption of resonator photons, different relaxation processes act to restore the thermal equilibrium ratio of equation (2.102). The most dominant relaxation channel is spin-lattice relaxation. At temperatures below $4\,\mathrm{K}$, so-called direct relaxation processes happen at which a spin relaxes back into the $|\downarrow\rangle$ state while generating a phonon of the same frequency as the ESR transition. For this case, the characterizing relaxation time T_1 is related to temperature and magnetic field via [59]:

$$T_1 \propto \frac{1}{B_0^2 T}. \tag{2.103}$$

For the case of high relaxation time and high incident microwave powers at the sample, the excitations outweigh the relaxation processes and the spin system approaches equal populations of both states. At $N_- = N_+$, the spin ensemble is considered to be saturated. Consequently, the number of addressable spins for ESR transitions becomes minimal as the thermal spin polarization given by equations (2.100) and (2.101) approaches zero. The same accounts for the effective collective coupling rate that is related to the thermal spin polarization by $g_{\text{eff}} \propto \sqrt{P(T)}$.

2.8 Spin Dynamics and Rotating Reference Frame

The spin ensemble of phosphorous donors in silicon represents a paramagnetic system, meaning it exhibits a non-zero total spin $\vec{J}$ and magnetization $\vec{M} \propto -\vec{J}$ in an external magnetic field $\vec{B}_0 = B_0\vec{e}_z$ at sufficiently low temperatures. This finite magnetization is a consequence of the thermal spin polarization and strives to align parallel to $\vec{B}_0$. However, the external magnetic field causes a torque $\vec{T}$ acting on the total magnetization:

$$\vec{T} = \vec{M} \times \vec{B}_0. \tag{2.104}$$

Together with the relations $\vec{M} = -\gamma_{\text{e}}\vec{L}$ and $d\vec{L}/dt = \vec{M}$, we obtain the time evolution of the magnetization [48, 60]:

$$\frac{d\vec{M}}{dt} = -\gamma_{\text{e}}(\vec{M} \times \vec{B}_0) = -\omega_{\text{L}}(\vec{M} \times \vec{e}_z), \tag{2.105}$$

where we introduced the Larmor frequency $\omega_{\text{L}} = -\gamma_{\text{e}}B_0$. The expression above describes the counterclockwise precession of $\vec{M}$ around the z-axis at an angular frequency ω_{L}.

Due to this precession movement, it is favorable to transit from the static laboratory reference frame to a rotating reference frame. This frame rotates at an angular frequency ω_0 around the z-axis. The sense of rotation follows the right hand logic with the thumb pointing parallel to the rotational angular velocity vector $\vec{\Omega} = \omega_0\vec{e}_z$. For the time evolution of $\vec{M}$ in this rotating reference frame, we find [61]:

$$\left(\frac{d\vec{M}}{dt}\right)_{\text{rot}} = \left(\frac{d\vec{M}}{dt}\right)_{\text{lab}} - \vec{\Omega} \times \vec{M} = (\omega_0 - \omega_{\text{L}})\vec{M} \times \vec{e}_z. \tag{2.106}$$

Hence, by choosing $\omega_0 = \omega_{\text{L}}$, the total magnetization $\vec{M}$ becomes a stationary vector.

In our experiments, we send pulses through the resonator which causes a linearly polarized magnetic field for the duration of the pulse:

$$\vec{B}_1 = B_1\cos(\omega_{\text{L}}t)\vec{e}_x, \tag{2.107}$$

that is perpendicular to B_0. Here, we already assumed the resonant case $\omega = \omega_{\text{L}}$ for the resonator-spin-ensemble system. Applying equation (2.106) to the resonator field also leads approximately to a static vector $\vec{B}_{1,\text{rot}} = B_1\vec{e}_x$. This is achieved by formally expressing the linearly polarized B_1 field as a superposition of a right and left circular polarized magnetic field in the xy-plane. It is obvious, that one of these parts becomes stationary in the rotating reference frame whereas the other rotates at double its original frequency 2ω. However, the latter can be neglected for $B_1 \ll B_0$, which is always fulfilled in our experiments.

Assuming $\vec{M} = M\vec{e}_z$, the presence of the resonator field $\vec{B}_{1,\mathrm{rot}}$ then changes the total magnetization analogously to equation (2.105):

$$\left(\frac{d\vec{M}}{dt}\right)_{\mathrm{rot}} = -\gamma_{\mathrm{e}}(\vec{M} \times \vec{B}_{1,\mathrm{rot}}) = -\omega_1 M\vec{e}_y. \tag{2.108}$$

Here, $\omega_1 = \gamma_{\mathrm{e}} B_1$ denotes the Larmor frequency for the precession around $\vec{B}_{1,\mathrm{rot}}$. The angle of rotation α is given by the pulse duration t_α during which $\vec{B}_{1,\mathrm{rot}}$ is acting on the $\vec{M}$:

$$\alpha = \omega_1 t_\alpha. \tag{2.109}$$

An applied pulse that causes a rotation by an angle of $\alpha = \pi/2$ is then called a $\pi/2$-pulse. The same logic applies for a π-pulse.

As already discussed in Chapter 2.7, spin lattice relaxation strives to restore the equilibrium state. Assuming the equilibrium total magnetization to be $\vec{M}_0 = M_0\vec{e}_z$, this relaxation process acts on the z-component of $\vec{M}$ via [10, 62]:

$$\left(\frac{dM_z}{dt}\right)_{\mathrm{rot}} = -\frac{M_z - M_0}{T_1}, \tag{2.110}$$

where T_1 is the characteristic spin-lattice relaxation time. This quantity is of importance for pESR measurements averaging over numerous repetitions of the same pulse sequence since it represents the minimal waiting time between two subsequent sequences. We refer to the time between two pulse sequences as the shot repetition time SRT.

Chapter 3

Resonators: Simulation and Fabrication

In this chapter, we focus on the practical implementation of superconducting microwave resonators for electron spin resonance applications. This requires the fundamental understanding of the resonator design to predict the magnetic field distribution and resonance conditions. We present modelling of the electromagnetic properties of the resonators using the finite element modeling software CST. In addition, we detail the fabrication procedure for the planar superconducting microwave resonators.

3.1 Finite Element Modeling of Planar Microwave Resonators

For our experiments, we typically use chips with lateral dimensions of $6\,\mathrm{mm} \times 10\,\mathrm{mm}$ and a thickness of $0.525\,\mathrm{mm}$. We then deposit the superconducting material NbTiN or Nb with a thickness of $150\,\mathrm{nm}$ on the silicon substrate. The resonator structure is then written and etched into this layer as described in the next section. The electron spin resonance experiments presented in Chapter 5 require the specific design of planar microwave resonators which operate at a target frequency of around $5\,\mathrm{GHz}$. To this end, we model the electromagnetic circuit on the chip using finite elements modeling (FEM). The software used for this purpose is "CST Studio Suite 2018", also known as "CST Microwave Studio" [22]. Our model includes the whole chip, consisting of silicon substrate, superconducting layer, resonator structures and signal ports. A screenshot of a modelled chip is shown in Figure 3.1.1. We choose the silicon to be a lossy material, which matches the applied high resistivity silicon chips best. On top of the substrate, a superconducting layer with a thickness of $150\,\mathrm{nm}$ is placed, modelled with perfectly electric conducting material (PEC).

In the scope of this work, we developed a fully parameterized model for planar lumped element microwave resonators implemented in CST. Figure 3.1.2 shows the model of the capacitively shunted meander resonator and summarizes all variables that can be adjusted to vary its characteristic properties such as resonance frequency or coupling constants. The capacitance C is given by an interdigital capacitor whereas the inductance L is provided by the meandering inductor as already shown in 2.1.1. The neighboring branches of the meandering inductor exhibit alternating current directions, which leads to destructive interference of the magnetic field and its localization near the surface of the resonator. This resonator design therefore provides a small mode volume that leads to higher filling factors for ESR experiments on small samples at the expense of magnetic field homogeneity. The resonator structure is framed by PEC which is then grounded in the simulation as well as in reality. The signal line is designed as a coplanar waveguide (CPW) consisting of a center conductor between two ground planes. As shown in

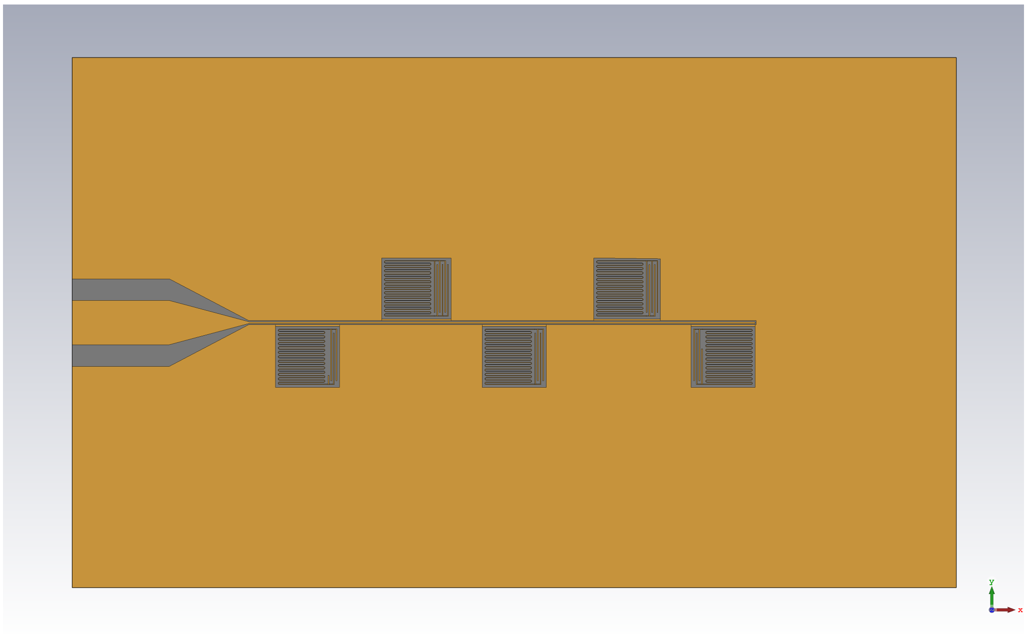

Figure 3.1.1: Chip with five resonators in reflection geometry modelled with CST. The silicon substrate is depicted in grey and the superconducting layer is shown in orange.

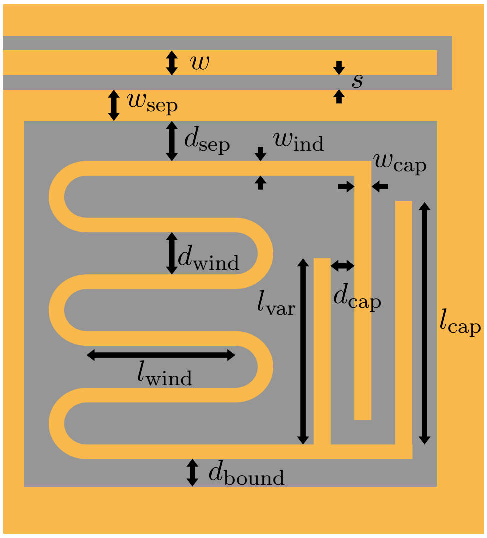

parameter	typical value (µm)
w	20
s	12
w_{sep}	5
d_{sep}	20
w_{ind}	5
d_{branch}	20
l_{wind}	500
l_{var}	300
l_{cap}	500
w_{cap}	10
d_{cap}	15
d_{bound}	30

Figure 3.1.2: Schematic of the fully parameterized resonator model for a planar microwave resonator (yellow) on silicon substrate (grey). The signal line is depicted in open circuit geometry for reflection type resonators. The table on the right hand side shows typical dimensions of the model used in this work.

Figure 3.1.2, we choose the width of the center conductor w to be $20\,\mu\mathrm{m}$ and the width of the gap between ground plane and center conductor s to be $12\,\mu\mathrm{m}$. Assuming the relative permittivity ε_r of the silicon substrate to be $\varepsilon_\mathrm{r} = 11.9$, these dimensions correspond to a line impedance of $Z_0 \approx 50\,\Omega$ according to the built-in line impedance calculator of CST and the analytical formula [63]

$$Z_0 = \frac{30\pi}{\sqrt{\varepsilon_\mathrm{eff}}} \frac{K(k_0')}{K(k_0)}. \tag{3.1}$$

Here, ε_eff is the effective dielectric constant, K denotes the complete elliptic integral and its arguments are $k_0 = \frac{w}{w+2s}$ and $k_0' = \sqrt{1-k_0^2}$.

In reflection geometry, the center conductor is discontinued in open circuit geometry with the gap at the end also having the dimension of s. Towards the edge of the chip, the CPW is broadened for the microwave connectors, which in reality can be planar pins contacted with conducting silver fluid or bonding wires. We keep the ratio w/s the same as for the narrow region, which also results in an impedance of $50\,\Omega$.

In CST, we contact the chip with waveguide ports, which are rectangular objects. Such a port should cover most of the relevant area of the coplanar line field, while also not causing higher modes to propagate in the CPW [64]. We therefore apply the recommended dimensions, which are illustrated in Figure 3.1.3. The planes of the bounding box enclosing the simulation volume are set to be electrically open boundaries.

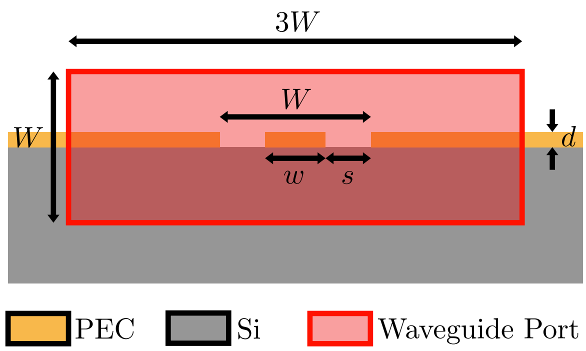

Figure 3.1.3: Schematic of the applied dimensions for the waveguide ports in CST. Ideally, the length of the waveguide port should be three times the spacing W between the two ground planes [64].

With these settings, we apply the frequency domain solver. It yields all possible S-parameters from which we obtain the resonance frequencies of the resonators. The simulated data of a resonator coupled to feedline in reflection geometry is shown in Figure 3.1.4. We observe a dip in the simulated and normalized $|S_{11}|$. The resonator can be viewed as a driven damped harmonic oscillator. For such an oscillator, one expects a lorentian curve for the amplitude with

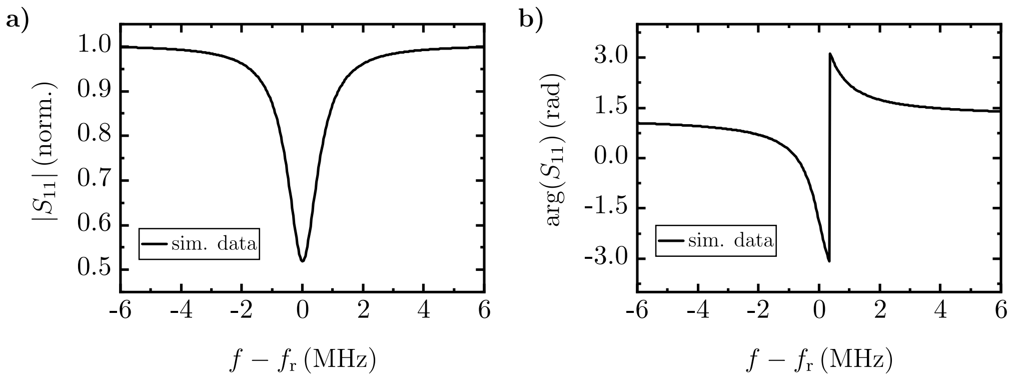

Figure 3.1.4: Simulated data of a resonator coupled to a feedline in reflection geometry. The measured data is plotted for a smaller range of frequency to exclude standing wave signatures and other background. **a)** Simulated $|S_{11}|$ parameter. The data has been normalized. The resonator exhibits a lorentian dip with its minimum at the resonance frequency f_r indicating the resonance absorption. **b)** Simulated phase. The relative phase changes by 2π when sweeping the frequency across the resonant one [65].

its maximum at the resonance frequency f_r [66]. We observe a dip due to the fact that we do not measure the amplitude of the resonator itself but the reflected signal. The dip therefore corresponds to signal being absorbed by the resonator and agrees with the model of a driven damped harmonic oscillator. The dip is described by the absolute value of equation (2.36), which is also a lorentian curve. Considering the phase signature, one would expect a change of the relative phase by pi when sweeping the frequency across the resonant one [66]. This is fulfilled for resonators coupled to a feedline in transmission geometry [67]. However, it is evident in the data of Figure 3.1.4 b) that the relative change of the phase is actually 2π across the resonance. This is characteristic for resonators that are coupled to reflection type feedlines and is a consequence of the additional factor of 2 in the nominator of equation (2.39) compared to (2.36) and classical driven damped harmonic oscillators [65]. From this data, resonance frequency and quality factors can be extracted by using the circlefit routine by [34, 68], which will be demonstrated in Chapter 4.3.1.

To show the magnetic field distribution, we extracted the simulated data of the field on a plane that is perpendicular to both feedline and substrate surface. The resulting data of the absolute value of the magnetic field B_1 is shown in Figure 3.1.5. We note that the incident microwave power at the sample of $P_{\text{MW}} = 27\,\text{dBm}$ is large compared to the applied incident powers in ESR experiments. This power is unfortunately fixed in the used frequency domain solver of CST Microwave Studio. Therefore, the value of the magnetic field is expected to be lower in reality and the simulated data only allows for a quantitative analysis of the field distribution. It is evident that the magnitude stays large up to a height of about $20\,\mu\text{m}$, which is approximately the thickness of our samples. This characteristic is important to reach good filling factors.

We can also observe the inhomogeneity of the field which is shown by the spike structures. This is due to the meandering structure of the inductor, which by design has neighboring branches of counter-flowing currents. Looking at the overall structure of the magnetic field distribution, it is obvious that the resulting pattern is not as repetitive as we would intuitively expect,

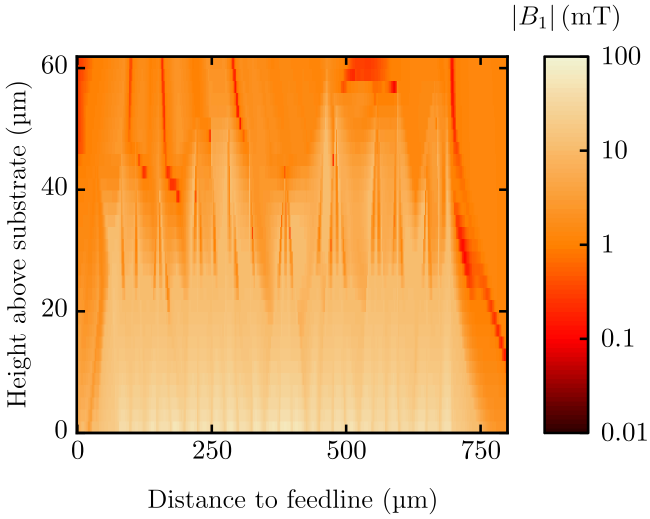

Figure 3.1.5: Simulated magnetic field $|B_1|$ of a LER for an applied power of $27\,\mathrm{dBm}$. The plot shows the absolute value of the magnetic field on a plane perpendicular to feedline and resonator plane. It cuts through the middle of the inductance of the resonator.

especially when looking at the spikes between a height above the substrate of $20\,\mu\mathrm{m}$ and $40\,\mu\mathrm{m}$.

3.2 Fabrication

In this section, we describe the fabrication procedure of planar superconducting microwave resonators. It consists of multiple cleaning steps, the sputtering of superconducting material onto the substrate, and the structuring of the resonators with electron beam lithography and subsequent reactive ion etching. The fabrication of resonators presented here and illustrated in Figure 3.2.1 is similar to the ones of [9, 18]. A more detailed version in a step by step procedure of the fabrication recipe can be found in appendix A.

Chip Preparation We start the fabrication with a high resistivity silicon (001) substrate that is cut into $6\mathrm{mm} \times 10\mathrm{mm} \times 525\mu\mathrm{m}$ chips. Firstly, we need to remove the protective coating from the polished surface. Therefore, we perform a multi-step cleaning procedure. We start with technical grade acetone and an ultrasonic bath treatment at medium power for 2 minutes. Next, we repeat this step twice with pro analysis (p.a.) grade acetone. Acetone removes the protective coating, organic residues and dust particles, but leaves residues on the substrate when evaporating. Therefore, we repeat the previous step one additional time with p.a. grade isopropanol to remove those residues [69]. The chips are then rinsed with p.a. grade isopropanol and dried with nitrogen gas to remove any remaining coating flakes or dust particles. Next, we place them on a preheated hotplate at $120\,^{\circ}\mathrm{C}$. The heat evaporates any remaining isopropanol to ensure that the chip is dry.

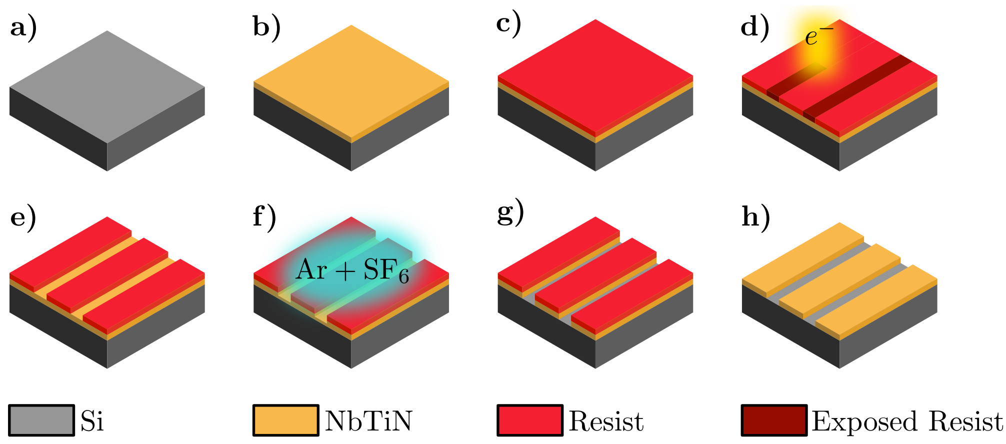

Figure 3.2.1: Illustrations of the various steps in fabrication of a chip with planar resonator structures. **a)** Pre-cut silicon substrates are chosen from a wafer and the surface is cleaned thoroughly. Silicon oxides are removed by HF etching. **b)** Superconducting material (here: NbTiN) is deposited onto the blank silicon chip by magnetron sputtering. **c)** Coating the surface oft the chip with resist, then bakeout. **d)** The structures are written into the resist via e-beam lithography. **e)** The exposed resist is removed by developing the resist. **f)** The remaining resist serves as an etching mask for reactive ion etching which etches the structures into the superconducting material. **g)** Structures are etched into the chip **h)** After removing the etching mask with the corresponding chemical, the sample is finished.

Removal of Silicon Oxides The silicon wafer naturally has a layer of silicon oxide on top of the surface. We deposit the superconducting material directly on top of the pure silicon surface in order to achieve high quality thin films. For this purpose, we remove the oxide layer by etching the silicon chips with liquid hydrofluoric acid for 30 seconds and bathing them in water afterwards to stop the etching process. With this treatment, the silicon surface also becomes passivated by hydrogen atoms which suppresses reoxidation long enough until the samples are placed in a vacuum airlock for sputtering of superconducting material [70].

Sputtering of NbTiN At WMI, a lot of thin film deposition devices are available for growth of superconducting materials, i.e. Al, Nb, and multi-component materials like NbTiN onto silicon substrates [71]. For our resonators, we deposit niobium titanium nitride (NbTiN) by magnetron sputter deposition with the **U**nlimited **L**egendary **T**ool for **R**eliable **A**chievements in the **D**eposition of **I**ntegrated **S**uperconducting **K**omponents (ULTRADISK) system by *Mantis*. Hereby, atoms of the target magnetron are ejected from the surface by bombardment of the latter with ions from a plasma in a vacuum chamber. The released target atoms can accumulate on the surface of the substrate that is placed above the magnetron. The latter has a negative bias to attract and induce kinetic energy to positive ions of the plasma, therefore increasing the rate of deposition compared to sputter deposition without using magnetrons [72]. A more detailed description of the working principle of sputter deposition and the ULTRADISK device itself can be found in [73].

We install the sample holder with the surface of the chips facing downwards into the main chamber. Next, the sample holder is heated up to a temperature of 500 °C and the argon plasma is ignited above the niobium titanium target magnetron in nitrogen atmosphere at low pressure. A shutter covers the plasma and the target to protect the substrate manipulator from deposition until we start the process. The target source placed on top of the magnetron is composed of 70% niobium and 30% titanium. The nitrogen component is controlled by the inlet of the corresponding gas into the chamber. Concerning gas flows, we set the one of argon to $36.2\,\mathrm{sccm}$[1] and the one of nitrogen to $3.8\,\mathrm{sccm}$. The sputtering rate is mainly around $0.8\,\mathrm{\AA/s}$. We then deposit a NbTiN layer with a thickness of $\approx 150\,\mathrm{nm}$ by placing the sample holder above the target and opening the shutter for the corresponding sputtering time. The NbTiN thin film is then grown on the polished surface of the silicon substrates as it is depicted in Figure 3.2.1b).

Niobium Chips In this work, we also fabricated resonators made of niobium. The niobium films are deposited onto silicon substrates by the PLASSYS device in house [71]. However, except for the program used for reactive ion etching, the fabrication process of niobium resonators is the same as the one described starting from here.

Preparing Chips for Lithography We clean the surface of the silicon chips with the superconducting material on top by applying a two-chemical-routine using p.a. grade acetone and p.a. grade isopropanol. The surfaces are now ready to be coated with e-beam resist.
We place the chip onto the spincoater. The resist of choice is the "AR-P 6200.18" of the CSAR 62 series by *Allresist* [74]. We place $\approx 40\,\mathrm{\mu L}$ of resist onto the chip. It is crucial to make sure that there are no air bubbles in the resist to ensure a homogeneous distribution of resist after spinning. The chip is then spun at a constant velocity of $8000\,\mathrm{rpm}$ for one minute. This results in a $\approx 550\,\mathrm{nm}$ thick layer of resist. Then we perform a bakeout on a preheated hotplate at a temperature of $150\,^\circ\mathrm{C}$ for one minute. The coated chip is illustrated in Figure 3.2.1c). In order to be able to properly focus onto the surface of the resist layer, we place four droplets of gold nanoparticles in the corners of the chip with a toothpick.

Electron Beam Lithography The resonator structures are written into the resist layer with an electron beam as shown in Figure 3.2.1d) [75]. We load the sample holder containing the chips into the main chamber of the e-beam machine. The applied dose for the lithography process is in the range of $2.1\,\mathrm{C/cm^2}$ to $2.3\,\mathrm{C/cm^2}$. To set the right focus, we use the build-in scanning electron microscope and search for the gold nanoparticles in the four corners. After having parsed the focus values to the executing software, the process is started.

Developing Exposed Resist Following the lithography step, we need to remove the exposed resist to reveal the etching mask for the next step as displayed in Figure 3.2.1e). For this purpose, we expose the resist to the corresponding developer chemical "AR 600-546" [76]. Afterwards, we stop the developing process by putting the chip in p.a. isopropanol followed by ultrasonic bath treatment at lowest power for about two minutes. With that, the remaining developer chemical gets deactivated and resist flakes are removed from the chip. Following this step, we rinse the chip with p.a. isopropanol and blow dry it with nitrogen. The chip then undergoes

[1] sccm: standard cubic centimeter. $1\,\mathrm{sccm}$ corresponds to a gas flow of $1\,\mathrm{cm^3/min}$ at standard conditions

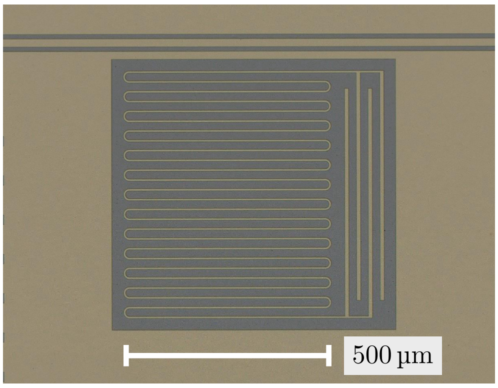

Figure 3.2.2: Fabricated planar superconducting lumped element microwave resonator. The resonator is made of NbTiN (ocher) on a silicon substrate (grey).

another bakeout on a hotplate at a temperature of $130\,^{\circ}\mathrm{C}$ for one minute. This post-exposure bakeout increases the resistance of the resist layer towards reactive ion etching.

Reactive ion etching Next, we need to structure the superconducting layer. We apply reactive ion etching as schematically shown in 3.2.1f). The remaining resist layer serves as an etching mask for the underlying superconducting layer and shields it from the etching plasma. The gas mixture being used for etching NbTiN consists of sulfur hexafluoride and argon, where the former makes up the major part with a gas flow of $20\,\mathrm{sccm}$ compared to $7.2\,\mathrm{sccm}$ of argon. With this gas mixture, we employ both chemical and physical etching [77]. The ions and radicals generated by the plasma get adsorbed onto the exposed surface of the chip and chemically react with the surface atoms. The products of these reactions are volatile and removed by the vacuum pump [78]. To counteract the apparent nonlinear behaviour of the etching depth as a function of time, we etch in two steps for 80 seconds each. In between those steps, the chamber is flooded and cooled down with nitrogen gas before it is subsequently evacuated again. In the scope of this thesis, we focused on ensuring that the etching depth is sufficient to avoid fabricating a shorted chip. Concerning Nb chips, we execute the etching process with only sulfur hexafluoride in a single step process for about 165 seconds.

Removal of Resist We remove the layer of resist by exposing it to the chemical "AR 600-71" [79]. After five minutes, we stop the process by placing the chip in p.a. isopropanol and place the beaker in the ultrasonic bath at low power for about two minutes to remove flakes of resist. After rinsing the chip with p.a. isopropanol and blowing it dry with nitrogen, we check under the microscope, whether all of the resist has been removed. We can also opt to heat up the remover chemical to $40\,^{\circ}\mathrm{C}$ for improved performance. Finally, the chip is free of any resist as shown in Figure 3.2.1h) and the fabrication is finished.

A fabricated resonator made of NbTiN is shown in Figure 3.2.2. The dimensions of the fabricated resonator match the simulation model thanks to the high precision of the e-beam lithography machine. The only deviation from the simulation model is the height difference between

NbTiN and silicon due to overetching the NbTiN layer and subsequently also etching the silicon as stated above. Hence, the etching edges do not exhibit a height of $150\,\mathrm{nm}$ but typically around $230\,\mathrm{nm}$ instead.

Chapter 4

Superconducting Microwave Resonators

In this section, we introduce different measurement setups, procedures and results leading to a performance characterization of the superconducting resonators for ESR applications. The first measurements characterize the quality and superconducting properties of our NbTiN and Nb thin films. In addition, we discuss the differences between identical resonators in transmission and reflection geometry. We assess their performance under various conditions, such as different external magnetic fields, incident microwave powers and temperatures. Finally, we demonstrate the influence of geometric variations in the resonator design on coupling constants and overall performance. The characteristics and fitting results of all resonators that are presented in this chapter are listed in section 4.3.5.

4.1 Measurement Setups

We start with introducing the setup used for the characterization of the NbTiN and Nb thin films using DC transport techniques as well as microwave spectroscopy of the fabricated resonators. For the majority of the measurements presented, we use variable temperature helium gas flow cryostats which have the option to supply a static magnetic field to the sample. The samples to investigate are mounted on a so-called dip-stick, which is designed to enable DC transport or microwave spectroscopy. All used dip-sticks come with their own local temperature sensors and active PID temperature control to guarantee temperature stability during the experiment.

Transport Measurement Setup While the cryostat provides the thermal environment and the static magnetic fields, we measure the resistivity of the thin films by transport measurements in the following manner. The initial chips with dimensions of $6\,\mathrm{mm} \times 10\,\mathrm{mm}$ are cleaved into smaller pieces and mounted on a transport chip carrier as shown in Figure 4.1.1 a). A total of 20 copper pads surround the samples and are connected to the DC lines of the dipstick. We contact the samples to the pads by aluminum wire bonds. Each piece is equipped with 6 contacts of which four are used for the transport measurements while the other two are used as backup.

Figure 4.1.2 shows the electrical wiring scheme for measuring the two samples simultaneously, including a sourcemeter, two nanovoltmeters and a breakout box. The breakout box is used to connect the other devices to the DC lines of the dipstick and subsequently the samples. The sourcemeter provides a DC current to both samples and will be also applied in the other direction of the current. The nanovoltmeters are each connected to one of the two samples and measure the drop in voltage across the sample.

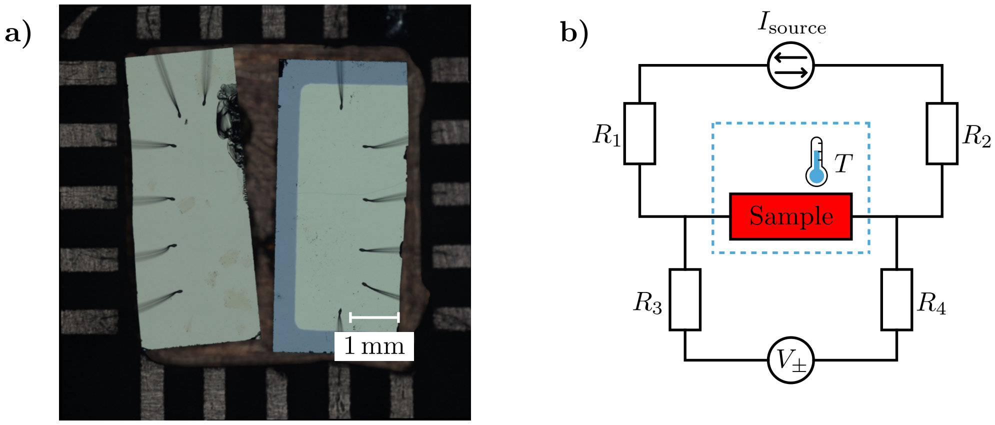

Figure 4.1.1: Prepared chip carrier and circuit schemactic for transport measurements with the Van der Pauw method [23]. **a)** Picture of two prepared NbTiN samples for transport measurements. The samples are contacted to the surrounding copper pads by thin aluminum bonding wires. The current flows from top side to bottom side contact and vice versa for both samples. Two of the remaining four contacts are each used for measuring the voltage drop of the sample. **b)** Circuit diagram of the transport measurements. R_1 to R_4 denote the resistances of the cables and wires. As a function of temperature T, the voltage $V_\pm$ is measured for $|I_{\text{source}}| = 100\,\mu\text{A}$.

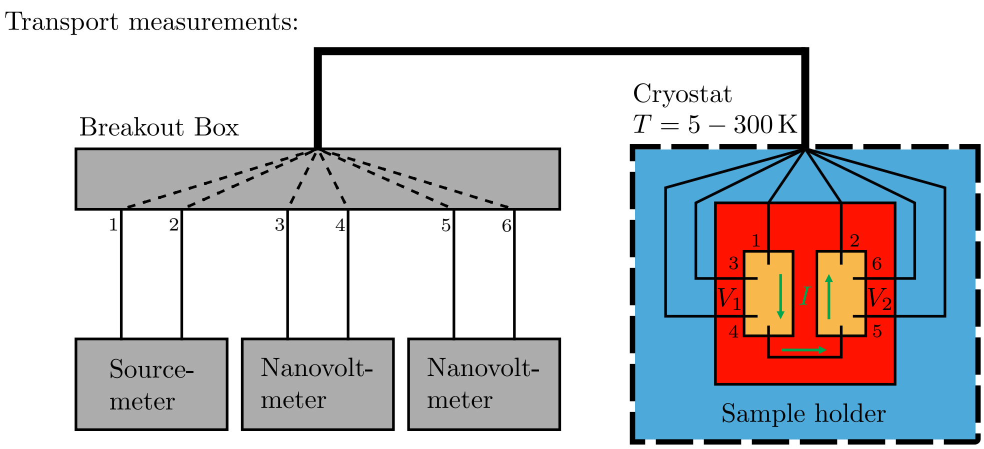

Figure 4.1.2: Schematic of the measurement setup for transport measurements. The breakout box connects the devices with the sampleholder to apply a current I to the samples and measuring their voltages.

The method of measurement we apply was developed by Van der Pauw [23]. It is a four point measurement, which is illustrated in the electric circuit diagram of figure 4.1.1 b) for one of the two samples. The quantities R_1 to R_4 denote the different resistances of the cables and contacts. We apply a constant current $I_{\text{source}} = 100\,\mu\text{A}$ to the chip carrier and measure the drop in voltage caused by the sample as a function of temperature. We measure the voltage both with positive and negative current to eliminate non-ohmic resistances from our measurements. The averaged voltage V is therefore calculated via

$$V = \frac{V_+ - V_-}{2}, \tag{4.1}$$

where the plus and minus subscripts indicate the sign of the applied current I_{source}.

We then calculate the measured resistance R of the sample with Ohm's law. The Van der Pauw method is used to measure the specific resistance ρ of the thin films [23]. For samples with a given axis of symmetry, ρ can be calculated via

$$\rho = \frac{\pi d}{\ln 2} \cdot R \approx 4.532 \cdot R \cdot d, \tag{4.2}$$

where R is the measured resistance and $d = 150\,\text{nm}$ is the thickness of the superconducting thin films.

To determine T_c, we start at 5 K and ramp up the temperature at a rate of up to $1\,\text{K}/\text{min}$ while measuring V. Afterwards we can determine the specific resistance as a function of temperature. For low temperatures, the resistance stays at a constant value and increases at T_c, as we would expect, since the superconducting phase collapses. The increase happens not in an instant, but in an interval ΔT.

Based on our measurement data, we can use two approaches to determine the transition temperature and the width of the transition. First, we can access both characteristics directly from the $\rho(T)$ curve by the so-called mean value method [80]. Referring to the maximum value of the specific resistance after the transition, we can define:

$$T_\text{c} = \frac{T_{10\%} + T_{90\%}}{2} \tag{4.3}$$

$$\Delta T = T_{90\%} - T_{10\%} \tag{4.4}$$

In addition, we can make use of the fact that the $\rho(T)$ curve can be described based on an error function. To do so, we determine the numerical derivative. For N measurement points, it is given by:

$$\frac{\mathrm{d}\rho}{\mathrm{d}T} = \frac{\rho_{i+1} - \rho_i}{T_{i+1} - T_i};\ i = 1, \ldots, N-1. \tag{4.5}$$

By analyzing to the first derivative of the curve, we are able to fit a gaussian curve to the data:

$$\frac{\mathrm{d}\rho}{\mathrm{d}T}(T) = y_0 + A \cdot \exp\left\{\frac{-(T - T_\text{c})^2}{2\sigma^2}\right\}. \tag{4.6}$$

From this fit, we extract the critical temperature T_c via the center of the gaussian function and

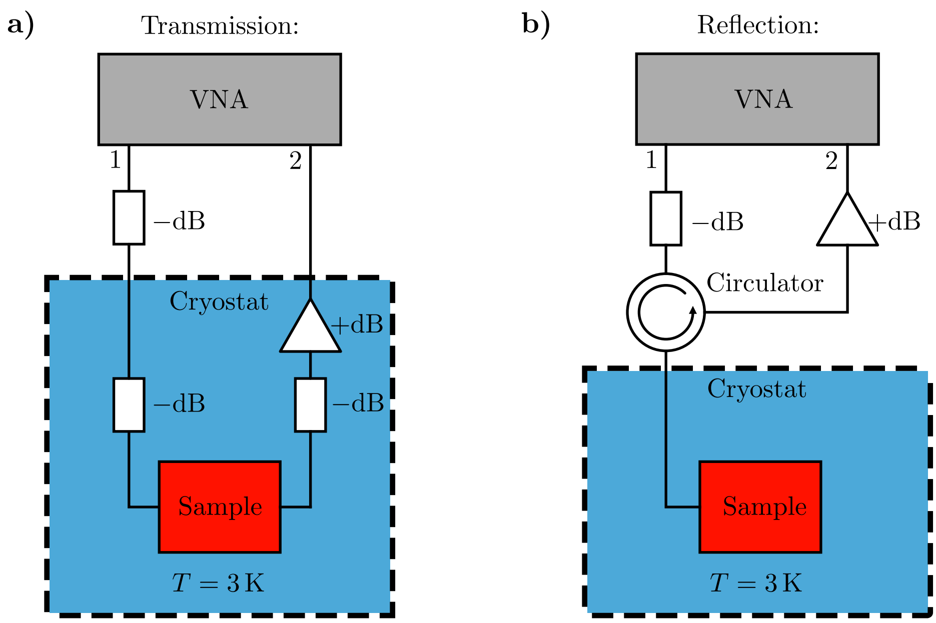

Figure 4.1.3: Schematic of the measurement setup for resonator characterization measurements for transmission and reflection geometry. The numbers denote the ports of the VNA, whereas white rectangles (triangles) denote the possible positions of attenuators (amplifiers). **a)** Arrangement for measurement of S_{21} of transmission type resonators. The signal is sent from port 1 and detected at port 2. A dipstick with a cryogenic HEMT amplifier can be used to enhance the output signal. **b)** Arrangement for S_{11} measurement of reflection type resonators. To reduce standing wave signatures, a circulator is additionally employed, which transforms this measurement of S_{11} into an effective S_{21} measurement for the VNA.

ΔT via the full width at half maximum (FWHM), given by:

$$\mathrm{FWHM} = \Delta T = 2\sqrt{2\ln 2} \cdot \sigma. \tag{4.7}$$

We also measure $\rho(T)$ up to room temperature values to extract another measure for the quality of the thin films, which is the residual resistance ratio RRR [80]. We define it as the ratio of the resistances at 300 K and 20 K:

$$RRR = \frac{R_{300\,\mathrm{K}}}{R_{20\,\mathrm{K}}} = \frac{\rho_{300\,\mathrm{K}}}{\rho_{20\,\mathrm{K}}} \tag{4.8}$$

The higher this value, the higher the quality of the thin film [80].

Resonator Characterization Measurement Setup Analogously to the transport measurements, we use a second liquid helium cryostat[1] setup for the characterization of the planar

[1] This cryostat is internally called 17 T due to the maximum magnetic field that can be applied to samples via its built-in magnet.

microwave resonators. Here, the cryostat is operated at temperatures between $3\,\mathrm{K}$ and $4\,\mathrm{K}$. The sample is installed using a dipstick with microwave cables. We use a VNA to measure the transmission and reflection parameter. Figure 4.1.3 summarizes the measurement setup for the transmission and reflection type configurations used for characterization of the resonators.

For resonators in transmission geometry, we measure the S_{21}-parameter in the configuration displayed in Figure 4.1.3 a). The port 1 of the VNA serves as the microwave source and port 2 detects the transmitted signal. In addition, we have access to a special microwave dipstick which hosts a cryogenic HEMT amplifier to enhance the outgoing signal. When measuring with this dipstick, we connect an attenuator between port 2 of the sample and the HEMT to protect the latter from large input powers and to ensure operating it in its optimal range of power.

In principle, reflection type experiments require only one microwave line as emitting and receiving port of the VNA are the same. For cryogenic experiments, however, the long microwave lines typically add a standing wave pattern to the investigated signal. To overcome this, circulators as close to the sample as possible are employed. They separate input and output line and restict potential standing waves to the line connecting sample and circulator. By using a circulator, the measurement becomes a two port measurement like in the case of transmission resonators. Consequently, S_{21} is measured with the VNA but the actually recorded data is the S_{11}-parameter. In addition, this configuration allows to also use low-noise preamplifiers.

In the case of reflection type resonators, we could measure S_{11} with just one cable connecting port 1 of the VNA to the sample. However, when doing so we cannot employ any amplifiers. More importantly, we receive a remarkable background signature of standing waves that form in the cable in our measurements. To mitigate these standing wave patterns, a circulator is used to redirect the reflected signal coming from the sample towards port 2 of the VNA. By using the circulator, the measurement becomes a two port measurement like in the case of transmission resonators. Consequently, we measure S_{21} with the VNA but actually record S_{11} data.

When measuring in a dilution cryostat at millikelvin temperatures, the applied measurement setups follow the same principles as the ones described for the $17\,\mathrm{T}$ cryostat. We employ the setups used by A. Jung and S. Weichselbaumer [81, 82].

Sample Boxes We apply two different sample boxes and methods of contacting the chips in this thesis. They are shown with mounted resonator chips in figure 4.1.4. Each box is made of copper. For the smaller one depicted in Figure 4.1.4 a), electrical contacts to connect the NbTiN ground planes to the grounded box and the SMA pin connectors to the signal line of the chip are established with conductive silver. In the case of the other sample box shown in Figure 4.1.4 b), the contacting is done by bonding wires of aluminum.

4.2 DC Characterization of NbTiN and Nb Thin Films

In order to obtain high quality planar superconducting microwave resonators, we quantitatively examine the quality of our superconducting NbTiN and Nb thin films by transport measurements. In particular, we measure the critical temperature T_c, also called transition temperature, above which the superconducting phase collapses and the electrical resistance becomes measurable [48]. Additionally, we also measure the specific resistance ρ over the whole temperature range

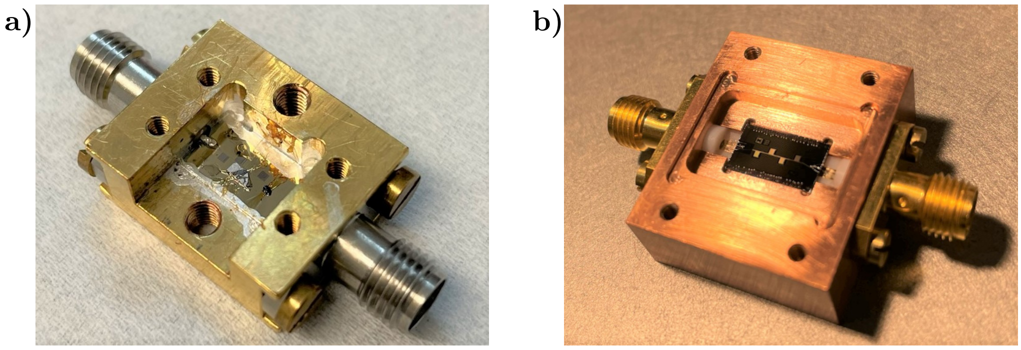

Figure 4.1.4: Sample boxes made of copper used for our measurements. The boxes are closed with a corresponding lid. **a)** In this sample box, the ground planes of the thin film are contacted to the grounded box via conductive silver. The SMA connector is contacted to the feedline of the chip in the same way. **b)** In this sample box, the chips are contacted through bonding wires of aluminum.

from $5\,\mathrm{K}$ to $300\,\mathrm{K}$. By measuring this dependency, we can extract the residual resistance ratio RRR which is an estimate of the thin film's quality [80]. These measurements are carried out in the transport measurement setup using the Van-der-Pauw method described in Chapter 4.1.

Figure 4.2.1 a) and c) show the measured $\rho(T)$ for NbTiN and Nb thin films with a thickness of $150\,\mathrm{nm}$. Panels b) and d) show the numerically computed $\frac{\mathrm{d}\rho}{\mathrm{d}T}(T)$ curves for both films. Fitting to the data the equation (4.6) yields T_c and ΔT. These results, as well as the ones obtained by applying equations (4.3) and (4.4) of the mean value method are summarized in table 4.2.1. We find for our NbTiN film a T_c of about $16\,\mathrm{K}$, which is in good agreement with literature values for its stoichiometric composition of Nb and Ti of $70:30$ from the target regardless of the fraction of nitrogen [83]. In comparison, we find a T_c for the presented Nb thin film of $7.9\,\mathrm{K}$, which is about $1\,\mathrm{K}$ lower compared to films of similar thickness presented in Ref. [84].

We next discuss the width of T_c characterized by ΔT. The transition width ΔT of Nb is almost seven times smaller compared to NbTiN. This can be intuitively understood since the ternary system of NbTiN is more difficult to grow homogeneously than monoatomic Nb. This gives a first indication, that the homogeneity of the Nb films is better than the one of the NbTiN films. However, we notice relatively large discrepancies between the results of the two methods for determining ΔT of Nb. This might be a consequence of the relatively low number of data points in the region of the superconducting transition, which limits the precision of the mean value method and therefore leads to the relatively larger value of ΔT compared to the one obtained from the gaussian fit.

We also measured $\rho(T)$ up to room temperature values to calculate the residual resistance ratio RRR by equation (4.8). The measured curves are shown in figure 4.2.2 and the RRR values are also listed in table 4.2.1. The RRR of Nb is about one and a half times larger than the one of NbTiN. This indicates a higher quality of these thin films.

We finally want to discuss the advantages of each material. NbTiN is a promising material for ESR experiments with superconducting resonator circuits, as it allows in principle to measure into the 10K regime, and to higher magnetic fields. Both properties are related to the larger superconducting gap compared to Nb [18]. In contrast, Nb does not perform well at these elevated

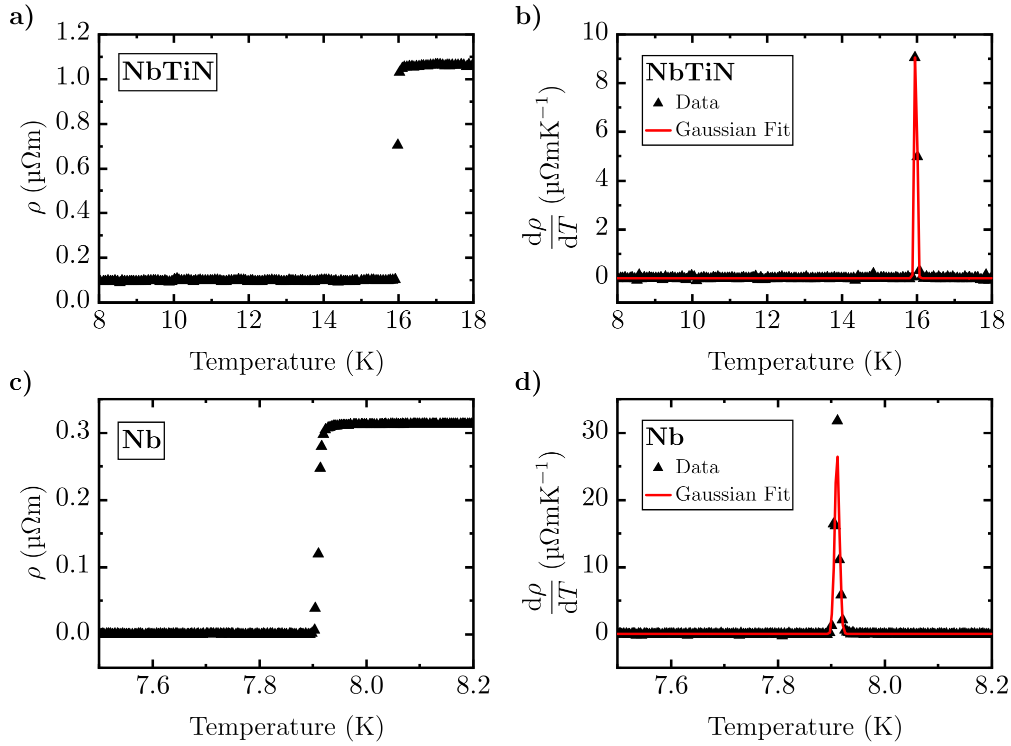

Figure 4.2.1: Results of the Van der Pauw measurements on the 150 nm thin films [23]. Dependent on the temperature T, **a)**,**c)** show the specific resistance ρ and **b)**,**d)** the numerical derivative of the NbTiN and Nb thin film, respectively. The critical temperatures are determined to be $T_{c,\text{NbTiN}} = 16\,\text{K}$ and $T_{c,\text{Nb}} 7.9\,\text{K}$ whereas the transition widths are $\Delta T_{\text{NbTiN}} = 0.0718$ and $\Delta T_{\text{Nb}} = 0.0107$ based on a gaussian fit

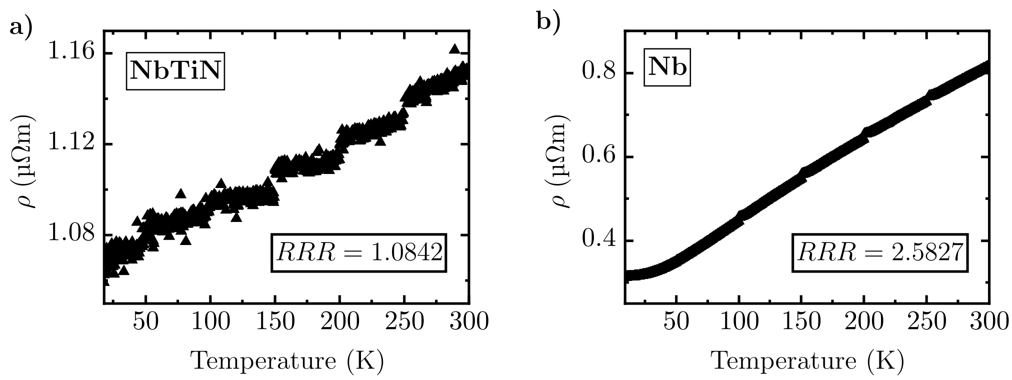

Figure 4.2.2: Measured $\rho(T)$ curves for **a)** NbTiN and **b)** Nb thin films up to room temperature to determine the RRR values that are summarized in table 4.2.1.

Material	RRR	Method	T_c (K)	ΔT (K)
NbTiN	1.0842	fit	15.968	0.072
		mean value	16.010	0.065
Nb	2.5827	fit	7.911	0.011
		mean value	7.912	0.015

Table 4.2.1: Results of the transport measurement with the Van der Pauw method [23], summarizing the critical temperature, transition width and RRR for NbTiN and Nb based on the measurements shown in figure 4.2.1 and 4.2.2. Fitting errors are negligibly small and therefore omitted.

temperatures of 3 K and above. The main reason is given by the lower critical temperature, which consequently leads to more losses due to excitation of quasiparticles at these temperatures [48]. However at millikelvin temperatures, the situation is more complex. Nb thin film resonators achieve very large quality factors i.e. for qubit readout. However, they suffer from significant losses when exposed to an external magnetic field. NbTiN does not quite reach as high quality factors as Nb but since it exhibits a better robustness towards such fields, it could potentially also outperform Nb lumped element resonators in ESR applications at millikelvin temperatures [18]. In conclusion, NbTiN is suited for experiments at liquid helium temperatures whereas Nb currently appears to be suited for measurements at millikelvin temperatures and low magnetic fields due to its larger internal quality factor.

Note on NbTiN Thin Films During this work, we unfortunately observed a decrease in quality of the NbTiN thin films. This decrease was evident in further transport measurements as well as in the internal quality factors Q_{int} of the fabricated resonators which undercut the results of [18] by one to two orders of magnitude. While exchanging the target in the ULTRADISK device did increase the quality again, we unfortunately did not manage to achieve the quality we had at the beginning of this work. Even a bakeout of the sputtering chamber did not yield remarkable improvements. Therefore, it seems like the ULTRADISK chamber is contaminated with impurities that limit the quality of the deposited NbTiN. We carried out additional transport measurements with thin films that have been sputter deposited with the new target and varied some process parameters. The results are included in appendix B.

4.3 Resonator Measurements

We now present our measurements of the resonators. We begin by displaying results on our first fabricated resonators and discussing the experimental findings in view of the coupling of the resonator to the feedline. We then show characterization measurements of our resonators for variations of magnetic field, temperature and microwave power at liquid helium and millikelvin temperatures. In addition, we display our results on the influence of geometric variations on both external and internal coupling rates of the resonators. Finally, we list all fit results of the resonators presented in this work.

4.3.1 Transmission and Reflection Geometry

In this section, we compare resonators coupled to a transmission and a reflection type feedline. We introduce the design of the resonator chips and point out the zero-field performance of the resonators.

Fabricated Chips Keeping in mind the application of ESR experiments, we use planar lumped element superconducting microwave resonators as describen in Ref. [9]. To compare different feedline geometries, we fabricate two chips, namely "JF001" and "JF002" with a transmission and reflection type signal line, respectively. In total, five resonators are coupled to the feedline, denoted by R1 to R5 according to an increasing resonance frequency. Unfortunately, R5 coupled to the reflection type of feedline is not working, as its inductor was visibly broken during fabrication. Figure 4.3.1 shows an overview of the resonator chips.

The structures on the chips are surrounded by a grid of $25\,\mathrm{\mu m} \times 25\,\mathrm{\mu m}$ squares with a center to center distance of $100\,\mathrm{\mu m}$ in the NbTiN thin film. This grid is used to trap flux lines of magnetic fields that are not parallel to the thin film surface. Since every superconducting thin film behaves like a type-II superconductor, flux pinning can occur [85]. Due to the fact that the cryostat of our measuring setup has a magnet that achieves fields of up to $17\,\mathrm{T}$, we cannot neglect trapped flux in the cryostat affecting the resonators.

Zero Magnetic Field Measurements We measured each resonator chip in its corresponding measurement configuration described in Chapter 4.1. We measure S_{21} for "JF001" and S_{11} for "JF002", respectively, at a temperature $T = 4\,\mathrm{K}$ and an incident microwave power at the sample of $P_{\mathrm{MW}} = -60\,\mathrm{dBm}$.

The data is fitted with the corresponding formulas (2.36) and (2.39) using the circle fit routine developed by Probst et al. [34] and implemented in Ref. [68]. The measured and fitted data of the absolute value of the scattering parameter and the phase are exemplary shown in Figure 4.3.2 for resonator R2 of each chip. As mentioned at the beginning of this Chapter, all fitting results of zero field measurements are listed in table 4.3.2.

To compare the two geometries, we plot the total and the external quality factor over the corresponding resonance frequency in Figure 4.3.3. Although the resonators are identical and the chips were fabricated as parallel as possible, the resonance frequencies do not match perfectly. We can see that the Q values of the reflection sample vary considerably compared to the transmission sample although they have been measured in the same type of sample box. We can also see the same course in Q_{ext}. Especially the large external quality factor for R1 of the reflection sample stands out and indicates weak coupling to the feedline. This can only be caused due to the difference in feedline geometry.

Position Dependent External Coupling for Reflection Type In electronics, impedance matching is a crucial practice to optimize transfer of power and minimize reflection of signal. When applying power to a load impedance Z_{L} from an impedance Z_0, the reflection coefficient is defined as [86]:

$$\Gamma = \frac{Z_{\mathrm{L}} - Z_0}{Z_{\mathrm{L}} + Z_0} \tag{4.9}$$

a)

b)

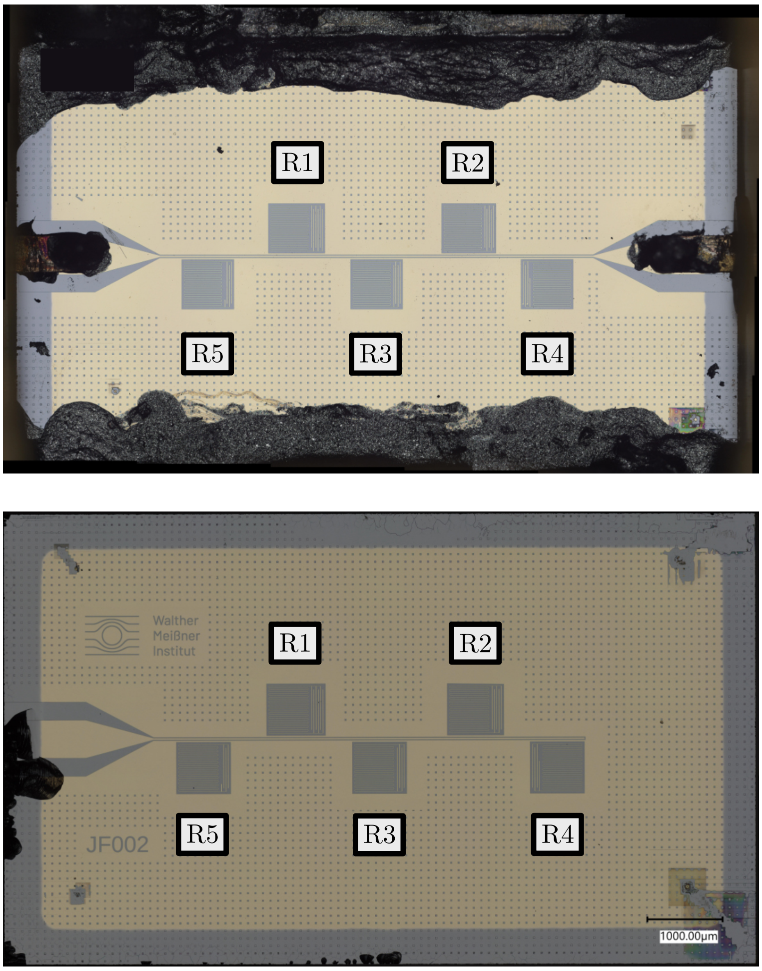

Figure 4.3.1: Samples "JF001" and "JF002" with resonators coupled to a transmission and reflection type feedline. The grid of squared holes in the yellow NbTiN film is for trapping potential magnetic flux lines. The resonators are numbered by ascending resonance frequency. **a)** Transmission sample "JF001" contacted inside a sample box. The dark grey structures is contact silver, which is used to ground the upper and lower NbTiN ground planes to the box and also contact the signal line to the SMA pin connectors. **b)** Reflection sample "JF002". Its design is the same as "JF001" but with a reflection type feedline. Resonator R5 unfortunately did not work due to being discontinued during fabrication.

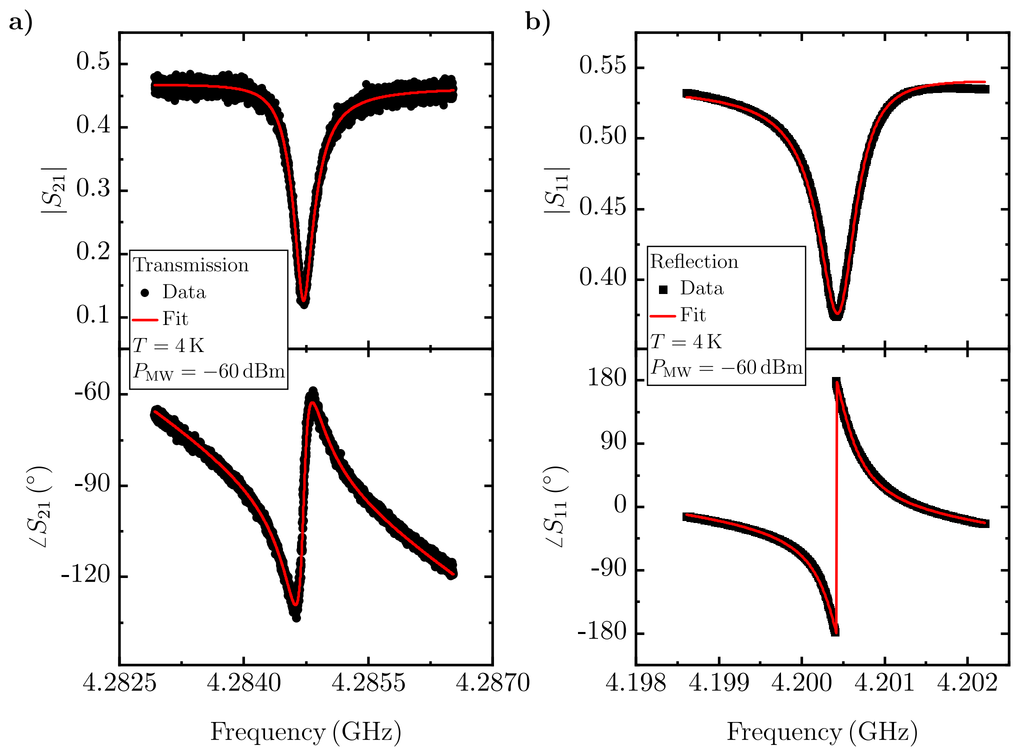

Figure 4.3.2: Measured and fitted data of resonator R2 from **a)** transmission chip "JF001" and **b)** reflection chip "JF002". The fitting was done based on the circle fit routine by [34, 68].

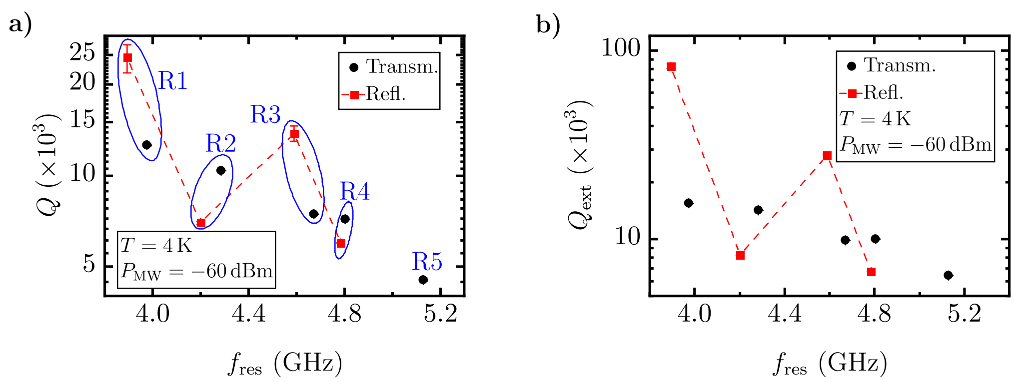

Figure 4.3.3: Fitting results of zero field measurements of transmission (JF001) and reflection (JF002) sample at $T = 4\,\mathrm{K}$ and $P_{\mathrm{MW}} = -60\,\mathrm{dBm}$. R5 of the reflection sample did not work and is therefore missing. **a)** The total quality factor Q dependent on the resonance frequency. While Q decreases almost linearly for the transmission type feedline, the change in Q shows an alternating wave-like pattern. **b)** Assuming no influence of the feedline design to the internal quality factor, the external quality factor Q_{ext} as a function of the resonance frequency reflects the behaviour of Q.

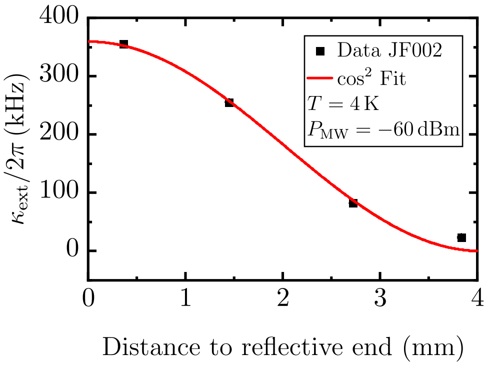

Figure 4.3.4: External coupling rate $\kappa_{\text{ext}}/2\pi$ depending on the relative position of the resonators to the reflective end of "JF002". The data points are fitted with a $\cos^2$ function indicating the standing wave of the voltage in the feedline.

It is obvious, that $\Gamma = 0$ for matching impedances.

For our transmission geometry, the two contacts between SMA pin connector and feedline port are possible sources of impedance mismatches. As discussed and mentioned in Chapter 3.1, the transmission line is designed to match an impedance of $50\,\Omega$ as best as possible, which is the impedance of the SMA connectors. Consequently, reflection coefficients are possibly non-zero and cause the formation of standing waves in the transmission line. However, due to the mismatch being very small by design, the influence of the standing wave to the coupling is also low.

As the name suggests, reflection geometry has one port of the chip replaced by an reflective end in form of an open circuit discontinuity. This end represents a hard boundary with $\Gamma = 1$ and certainly causes standing waves with much higher intensity than for feedlines in transmission geometry. We can clearly see the standing wave in the data of the reflection sample, when plotting the coupling rate $\kappa_{\text{ext}}/2\pi$ instead of $Q_{\text{ext}}/2\pi$ over the distance of the center of the resonators to the reflective end. This is visualized in figure 4.3.4.

The underlying standing wave is fitted with a $\cos^2$ function. Based on the fit, we identify the first node at $\lambda/4 \approx 4\,\mathrm{mm}$. This explains the large Q_{ext} of R1 as mentioned earlier, since it is located at the electric field node. Apart from the standing wave, the plot also proves that the coupling of our resonators to the feedline is mostly of capacitive nature. For a feedline that is terminated in open circuit geometry, an anti-node of the voltage is located right at the end [87]. This is exactly what we measure and shown in figure 4.3.4.

In conclusion, we need to respect the position dependent coupling to the feedline when designing resonators in reflection geometry with a certain coupling rate κ_{ext}.

4.3.2 Characterization Measurements

We demonstrate the performance and behavior of the resonators under various conditions in the following. The main contributors that influence the resonators are the kinetic inductance and two level systems as described in Chapters 2.4 and 2.5. We present measurements at variations

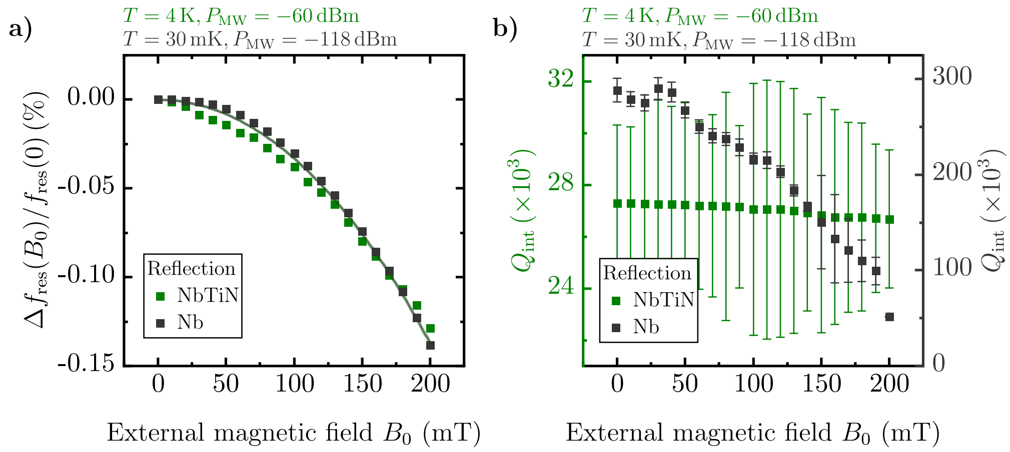

Figure 4.3.5: Measurement of a NbTiN ("JF002") and Nb resonator chip ("JF016") with reflection type feedlines in different external in-plane magnetic fields B_0. The measurement of the NbTiN chip was performed at liquid helium temperatures whereas the one of the Nb chip was measured at millikelvin temperatures. **a)** Relative frequency shift $(f_r(B_0) - f_r(0))/f_r(0)$ as a function of the external magnetic field. The resonance frequency decreases due to a change in kinetic inductance L_k and London penetration depth λ_L. The data was fitted with equation 2.92. **b)** Internal quality factor Q_{int} over external magnetic field B_0. Q_{int} for NbTiN is rather robust towards the external field whereas the one of Nb decreases remarkably with increasing field amplitude.

of external magnetic field, temperature and incident microwave power. At the same time, we discuss the observed differences between the superconducting materials NbTiN and Nb.

4.3.2.1 Microwave Resonator Performance in in-plane Magnetic Fields

ESR experiments typically require the application of a static magnetic field B_0 to tune the Zeeman energy. When using superconducting resonators, this field is typically applied in the plane of the superconducting thin film to avoid the formation of vortices and the deterioration of the quality factor.

For the investigation of the performance in static magnetic fields, we choose one resonator each, coupled to a feedline in reflection geometry from the NbTiN chip "JF002" and from the Nb chip "JF016". We measure these resonators exposed to in-plane magnetic fields from $0\,\mathrm{mT}$ to $200\,\mathrm{mT}$. This magnetic field range covers the region in which ESR-experiments on phosphorous donor spins in silicon are possible with our resonators. The measurement of NbTiN was performed at elevated temperatures and the one of the Nb chip at millikelvin temperatures, which is the optimal temperature region for the latter, as discussed in Chapter 4.2. The fit results for the relative shift of the resonance frequency $(f_r(B_0) - f_r(0))/f_r(0)$ and the internal quality factor Q_{int} depending on the field are shown in figure 4.3.5.

We can see that the resonance frequency remains mostly unchanged for fields of up to $50\,\mathrm{mT}$ before a drop off sets in. The decrease seems to become linear for fields larger that $150\,\mathrm{mT}$. However, the overall course and values of the shift are very similar for both materials. A possible reason for this might be the different temperatures at which the different materials are measured.

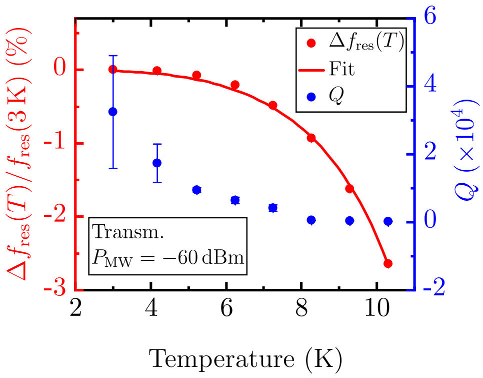

Figure 4.3.6: Temperature dependent measurement of transmission resonator R1 from the NbTiN chip "JF001". The resonance frequency shifts to lower values with increasing temperature. This data is fitted based on equation (2.94). The total quality factor Q also decreases very fast and fully collapses above 7 K, which is still way below the critical temperature of NbTiN $T_c \approx 16\,\text{K}$ which we also measured in Chapter 4.2 [83].

It is evident, that the shift is rather small as it is in the sub-percent region which translates to a few hundred kilohertz for resonance frequencies of a few gigahertz.

The situation is notably different when looking at the internal quality factors of both materials. The difference of the values in zero magnetic field is partially explained by the different temperatures. However, the main reason is given by the Nb thin films being of higher quality than the ones of NbTiN as discussed in Chapter 4.2.

Concerning the course of Q_{int}, NbTiN only shows a slight decrease over the full range of B_0. In contrast to that, Nb suffers visibly from the influence of the magnetic field and Q_{int} seems to collapse completely for even larger fields. This comparison shows that NbTiN resonators are far more robust towards the influence of external magnetic in-plane fields than Nb ones.

Based on the considerations of Chapter 2.4, we make an attempt to fit the data of the resonance shift. The fits to the data based on equation 2.92 are shown as green and grey lines in figure 4.3.5 a). Unfortunately, we do not know all three unknown parameters, which correlate with each other and therefore lead to large uncertainties. We therefore cannot extract any reasonable results by fitting the data without knowing two of the three unknown quantities. In addition, literature has contradictory definitions of the critical field as well as the magnetic field dependency of the London penetration depth [88, 89].

4.3.2.2 Temperature Dependence of Microwave Resonators

The temperature at which the resonator characterization measurements are carried out has significant influence on their performance and the dominant loss channels. At elevated temperatures, the latter is given by the change in kinetic inductance whereas TLS are the main loss contributors at millikelvin temperatures. We performe measurements for both temperature regimes and investigate the behavior of both resonance frequencies and quality factors.

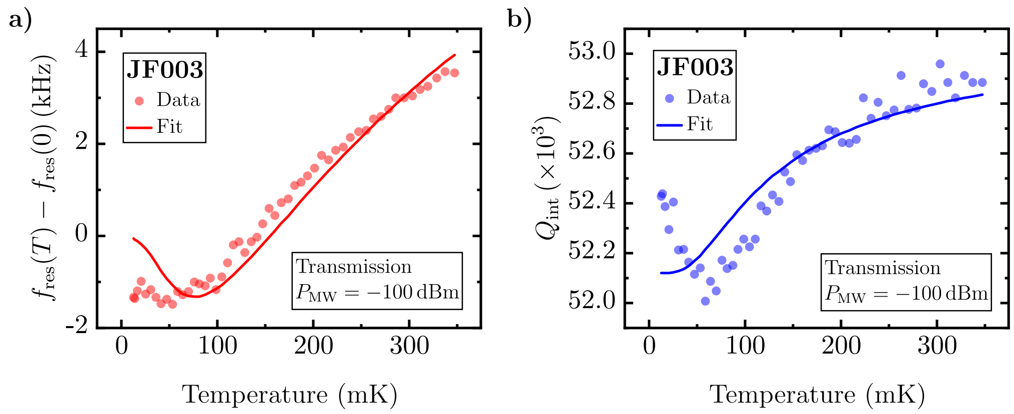

Figure 4.3.7: Temperature dependent measurement of transmission type resonator R1 from the NbTiN chip "JF003". **a)** The frequency ascends together with the temperature T. The fit by equation (2.96) only deviates for very low temperatures from the measurement data. **b)** The internal quality factor Q_{int} also increases with the temperature and starts to saturate at around $300\,\mathrm{mK}$, which is due to more TLS being thermally excited and the shift of the resonance frequency causing the TLS to be off-resonant. The fit by equation 2.95 is in good agreement with the measured data.

Measurement at Liquid Helium Temperatures For temperatures above $1\,\mathrm{K}$, we measure the resonator R1 of the transmission chip "JF001" at an incident microwave power $P_{\text{MW}} = -60\,\mathrm{dBm}$ in intervals of $\Delta T \approx 1\,\mathrm{K}$ from $3\,\mathrm{K}$ to $10\,\mathrm{K}$ and extract the relative shift of the resonance frequency $\Delta f_{\text{r}}(T)/f_{\text{r}}(3\,\mathrm{K})$ as well as the total quality factor Q. The data is shown in figure 4.3.6.

Similar to the measurement under different external magnetic fields B_0 from the previous chapter, the resonance frequency shifts to lower values with increasing temperature. The shifts are rather small up to $5\,\mathrm{K}$ before reaching the order of a few percent. The total quality factor also decreases rapidly and fully collapses above $8\,\mathrm{K}$, which is still remarkably lower than the critical temperature $T_c \approx 16\,\mathrm{K}$ of NbTiN [83]. To still operate the resonators at reasonably high quality factors, we set the upper limit for the temperature to $4\,\mathrm{K}$. Nevertheless, for the setup in liquid helium cryostats, one should always aim for $3\,\mathrm{K}$ to measure with even better quality factors.

We fit the relative resonance frequency shift of the resonator based on equation (2.94) to the data, which is shown as the red line in figure 4.3.6. The fit yields a ratio of kinetic inductance to total inductance of $\alpha = 0.157 \pm 0.031$ and a critical temperature $T_c = (14.47 \pm 0.58)\,\mathrm{K}$. The slight deviation of T_c from the expected value of $16\,\mathrm{K}$ can be explained by the fact, that the reference frequency for the shift is set at $3\,\mathrm{K}$ instead of $0\,\mathrm{K}$. However, the fit model is in good agreement with the measured data.

Measurement at Millikelvin Temperatures After having investigated the robustness of NbTiN resonators at elevated temperatures, we also examine their response to changes of temperature in the millikelvin regime. The measured transmission resonator is R1 of the chip "JF003", which we measure in a temperature range from $13\,\mathrm{mK}$ to $347\,\mathrm{mK}$ at an incident microwave power $P_{\text{MW}} = -100\,\mathrm{dBm}$. The measured data of the difference in resonance frequency

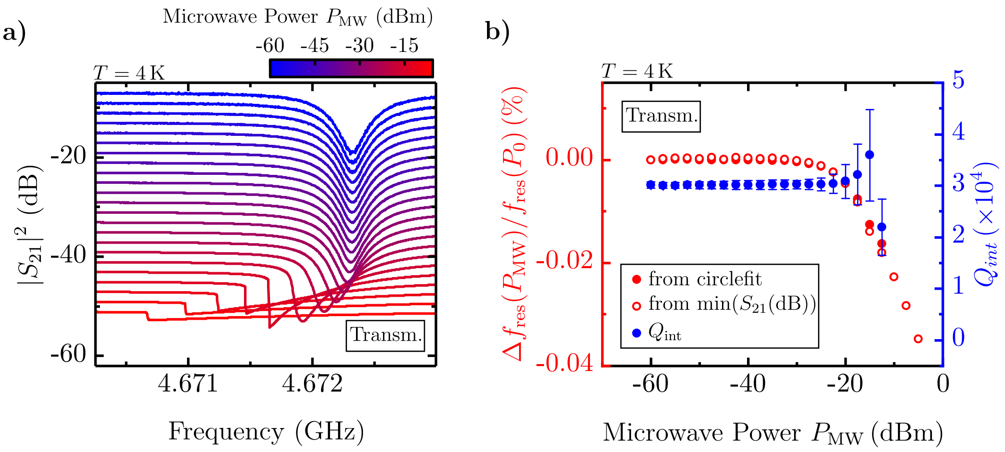

Figure 4.3.8: Power dependent measurement of transmission resonator R3 of NbTiN chip "JF001". **a)** Resonator lineshape for different applied incident microwave powers. For better visibility, the lines are offset by $2\,\mathrm{dB}$. The line shape becomes asymmetric with increasing incident microwave power. **b)** Results of fitting the data of the power dependent measurement with the circlefit routine [34, 68]. The fit routine fails to yield reasonable results for powers of $-20\,\mathrm{dBm}$ and higher. Therefore, the relative shift in resonance frequency was also determined by taking the values at the minima of the resonance dips in the S_{21} spectra.

and the temperature dependent internal quality factor Q_{int} are presented in figure 4.3.7.

Both measured quantities show the same course. With increasing temperature, they first decrease in a small region up to about $75\,\mathrm{mK}$ before the trend is inverted and the values increase. For Q_{int}, the data hints a saturation at temperatures higher than $300\,\mathrm{mK}$. The main reason for these behaviors are TLS that become more and more thermally excited until they are saturated and do not provide loss channels to the resonator.

The data shown in figure 4.3.7 a) can be fit based on equations (2.96) and (2.95). From fitting the internal quality factor, we obtain $Q_{\text{TLS}} = (2.9 \pm 0.2) \cdot 10^6$ and $Q^* = (53.07 \pm 0.04) \cdot 10^3$. From the fit results and the data, we can clearly see that under these measurement conditions, Q_{int} is mainly given by Q^* and only slightly modified by Q_{TLS}.

From the fit of the relative frequency shift, we extract a TLS quality factor of $Q_{\text{TLS}} = (181 \pm 7) \cdot 10^3$, which is one order of magnitude lower than the result received by fitting the internal quality factor. This shows, that off-resonance TLS have a larger influence on the frequency shift than on internal resonator losses.

4.3.2.3 Power Dependence of Microwave Resonators

The last parameter that can be varied when measuring the resonators is the applied incident microwave power P_{MW}. We measured the behavior of the NbTiN resonators towards high powers at liquid helium temperatures whereas at millikelvin temperatures, we investigated the power dependence down to the single-photon regime for both NbTiN and Nb.

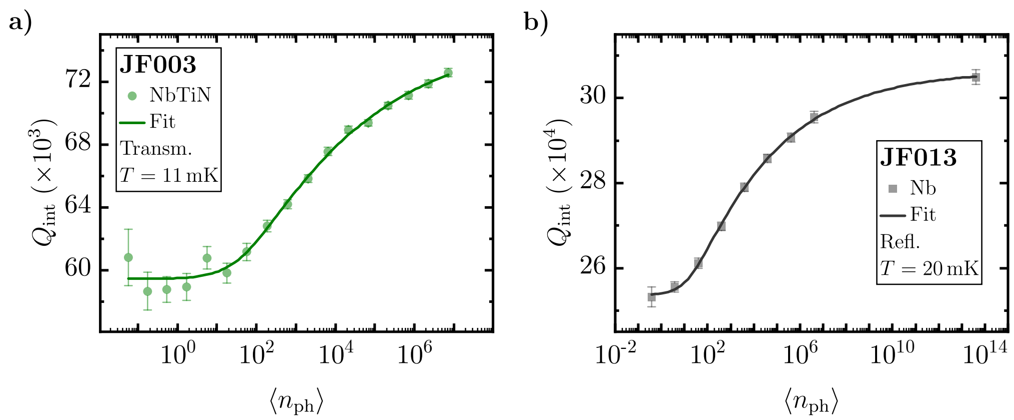

Figure 4.3.9: Power dependence of Q_{int} at millikelvin temperatures for resonators made of **a)** NbTiN and **b)** Nb as a function of average photon number $\langle n_{\mathrm{ph}} \rangle$. TLS losses prove to be a dominant loss channel of the resonators until they are saturated at high photon numbers. The data is fitted based on equation (2.97)

High Power Dependence at Liquid Helium Temperatures We measured the power dependent behavior of NbTiN resonator R3 from chip "JF001" at $4\,\mathrm{K}$. The incident microwave powers ranged from $-60\,\mathrm{dBm}$ to $-5\,\mathrm{dBm}$ in steps of $2.5\,\mathrm{dBm}$. The measured data and extracted fit values are shown in figure 4.3.8. The measured $|S_{21}|^2$ data as a function of the frequency is plotted in 4.3.8 a) for each applied power. In order to distinguish the color coded lines, they are plotted with an offset of $2\,\mathrm{dBm}$ to each other.

It is evident that the line shape of the resonance becomes asymmetric for high enough powers. Different nonlinear behaviors of planar microwave resonators have been observed in Ref [90]. Some of these nonlinearities can be jumps in the resonance spectrum, hysteretic behaviour and the lineshape becoming asymmetric. The effect that is present in our data is the transition from an harmonic oscillator at low powers to a duffing oscillator at applied incident microwave powers larger than $-20\,\mathrm{dBm}$.

This behavior also affects the fitting of the data with the circle fit routine, as shown in figure 4.3.8 b). The fit routine fails to yield the correct results for high enough powers since the resonator is not operating in the linear response regime. Therefore, we also approximated the resonance frequency by extracting the minimum of the data shown in Figure 4.3.8 a), which reliably exhibits the decrease of the resonance frequency as a function of applied power.

The internal quality factor Q_{int} shows stability over a wide range of power. However, as already discussed for the fit results of the resonance frequency, the values for Q_{int} cannot be fully trusted at high powers. This is supported by the increasing fitting errors for powers beyond $-20\,\mathrm{dBm}$.

Microwave Resonators at Millikelvin Temperatures At millikelvin temperatures, TLS play a dominant role in the performance of the resonators [53]. In order to investigate the dependence of the internal quality factor on unsaturated TLS, we performed power dependent measurements for both NbTiN and Nb resonators from $-160\,\mathrm{dBm}$ to $-14\,\mathrm{dBm}$. We can also

Material	Q_{TLS}	$\langle n_{\text{c}} \rangle$	ν	Q^*
NbTiN	285646 ± 30200	39.5 ± 24.8	0.163 ± 0.046	75087 ± 1960
Nb	1471681 ± 24400	14.73 ± 3.04	0.133 ± 0.006	306454 ± 729

Table 4.3.1: Results obtained by fitting the data of figure 4.3.9 with equation 2.97. TLS prove to have higher influence on losses in NbTiN than in Nb.

convert the incident microwave power at the sample P_{MW} to the average number of photons $\langle n_{\text{ph}} \rangle$ in the resonator by [56]:

$$\langle n_{\text{ph}} \rangle = \frac{4\kappa_{\text{ext}} P_{\text{MW}}}{h f_{\text{r}} \kappa^2}. \tag{4.10}$$

In the expression above, we plug in the coupling rates that we calculate from the fitted quality factors by use of equation (2.33). The measured internal quality factors are shown in figure 4.3.9.

Both materials show a constant course of Q_{int} in the single-photon regime. For larger photon numbers the internal quality factor increases until it saturates at very high photon numbers. This effect of saturation directly translates to the TLS, which eventually saturate at high incident microwave powers.

The data in figure 4.3.9 can be fitted by equation (2.97). The results of the fits are listed in table 4.3.1. In general, we can see that the values of Q^* differ by an order of magnitude, which is due to the higher quality of the Nb thin films. For both materials, Q_{TLS} exceeds Q^* by one order of magnitude, which can be interpreted as the relative influence of TLS being the same for both materials.

However, we observe notable differences in the values for the critical mean photon number $\langle n_{\text{c}} \rangle$. Here, the value for NbTiN is more than twice as large as the one of Nb, indicating that TLS start to saturate at higher photon numbers for NbTiN resonators. However, it must be noted that the error of the value for NbTiN is also significantly large, which might be a consequence of not having measured high enough incident microwave powers for the NbTiN resonator. Finally, we notice the same deviation of ν from the standard value 0.5 for both material systems.

4.3.3 Tuning External Coupling

An important characteristic of the resonators is the coupling strength to the feedline. As shown in Chapter 2.1.2, it is described by the external coupling rate κ_{ext} and the corresponding quality factor Q_{ext}. In order to reach certain coupling rates, a profound understanding of the geometric parameters influencing the coupling mechanism is needed.

In general, κ_{ext} depends on the position of the resonator relative to the feedline. On the one side, it depends on the relative position to standing waves forming in the feedline, which we addressed in Chapter 4.3.1. On the other side, κ_{ext} can be tuned by varying the spacing between resonator and feedline.

To investigate this relation, we fabricate the NbTiN chip named "JF003" with eight resonators. We choose transmission geometry, since the influence of standing waves on κ_{ext} is of significantly lower importance in this geometry compared to reflection geometry. The resonance frequency and the width of their separating grounded NbTiN-stripe of the resonators increase

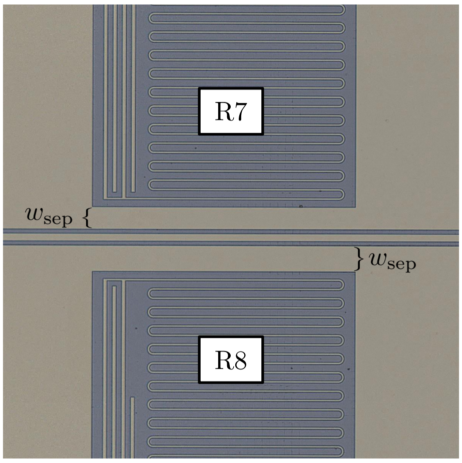

JF003 (transmission)	
Resonator	w_{sep} (µm)
R1	5
R2	10
R3	20
R4	30
R5	40
R6	50
R7	60
R8	70

Figure 4.3.10: Visualization of the resonator arrangement of chip "JF003" using the example of resonators R7 and R8. The table shows the different spacings of the separating stripe w_{sep} for each of the eight resonators. The resonators are placed in pairs along across the chip with each of them being separated by the feedline.

from one side to the other side of the chip. We choose widths of the separating stripe w_{sep} from $5\,\mu\text{m}$ to $70\,\mu\text{m}$. The situation is exemplary shown in figure 4.3.10 for the pair of resonators R7 and R8. We measure the chip at $T = 3\,\text{K}$ and at an incident microwave power of $P_{\text{MW}} = -60\,\text{dBm}$. Additionally, we also run a CST simulation for widths of w_{sep} from $1\,\mu\text{m}$ to $75\,\mu\text{m}$. The measured and simulated data is evaluated with the circle fit routine and κ_{ext} is obtained from Q_{ext} via equation (2.33) [34, 68]. The results are shown in figure 4.3.11.

The simulated data shows a clear descending course. However, the experimental data shows an alternating but overall also descending course. We can clearly identify the four pairs and that the resonators of each pair are placed on both sides of the feedline. This effect can be explained by the large numbers of resonators. When designing a chip, we make sure that the resonators are placed fairly away from each other around the feedline to be isolated from effects caused by their neighbors. For 8 resonators, this is not possible anymore and the resonators of each pair influence each other, which might cause the observed alternating course of the data points from left to right.

Despite this pairing effect, both sets of data show that κ_{ext} is inversely proportional to w_{sep}, which is exactly what we would expect for capacitively coupled resonators. This becomes clear when viewing feedline and top part of the resonator as the plates of a capacitor C_{coupling} and w_{sep} as the distance between them. When doing so, it is consequently evident that κ_{ext} increases with decreasing w_{sep}.

4.3.4 Varying Inductor Geometry

In general, we require high quality resonators for ESR experiments, so that dissipation of the signal caused by the resonator itself is minimized. The characterizing quantity is Q_{int}, which is a measure for the internal losses of a resonator as described in Chapter 2.1.2. The larger Q_{int}, the lower the losses. In general, the internal quality factor is given by the different interfaces

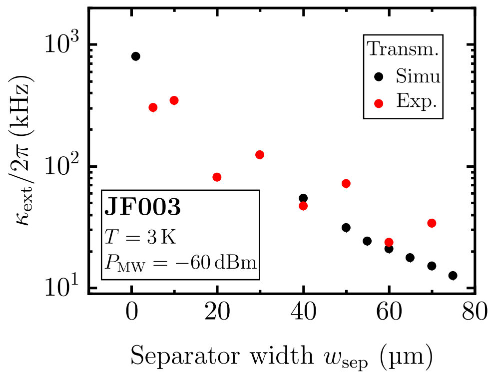

Figure 4.3.11: External coupling rate $\kappa_{\mathrm{ext}}/2\pi$ as a function of the width of the separating stripe w_{sep} for transmission chip "JF003" together with simulated data. The experimental data shows a pairing pattern which might originate due to the resonators of the same pair influencing each other, as shown in figure 4.3.10. The coupling rate decreases with increasing distance between resonator and feedline.

between substrate, thin film and air [91].

However, losses due to the resonator geometry also contribute to Q_{int}. We identified the inductance as the part of the resonator that shows potential for optimization, since the maximum current is reached in this element. We investigated the influence of the width of the inductor stripe w_{ind} on the internal quality factor by varying the former. When doing so, one also has to adjust the distance between the windings d_{wind} or the effective curvature radius r_{eff}, which we define with the inner radius of the u-bend r_{in} as:

$$r_{\mathrm{eff}} = r_{\mathrm{in}} + 0.3 w_{\mathrm{ind}}. \tag{4.11}$$

This is needed to avoid transmission losses in the u-bends of the inductor. In general, a radial bend fulfilling $r_{\mathrm{eff}} \geq 3w_{\mathrm{ind}}$ basically shows the same behaviour as a straight segment [92]. However, fulfilling this condition would lead to geometrically too large inductors. Instead of this condition, we require $r_{\mathrm{eff}} = 2w_{\mathrm{ind}}$ or $d_{\mathrm{wind}} = 3.4w_{\mathrm{ind}}$, which promises to be a good compromise [93]. A winding with the important quantities is illustrated in figure 4.3.12.

We fabricated the chip "JF014" with five resonators made of high quality niobium coupled to a transmission type feedline. The number of windings for each inductor remains constant and the widths of w_{ind} were chosen to be in the range of $3\,\mathrm{µm}$ to $15\,\mathrm{µm}$, while fulfilling the relation for the effective curvature radius mentioned before. We measure the resonators at a Temperature $T = 20\,\mathrm{mK}$ and at an incident microwave power of $P_{\mathrm{MW}} = -84\,\mathrm{dBm}$ and extract the internal quality factor Q_{int}. The results are shown in figure 4.3.13.

Although fulfilling the stated condition for the curvature radius, the data unfortunately gives no clear hint on which value to chose for w_{ind}. It makes no apparent sense that the quality factor takes a dip at $w_{\mathrm{ind}} = 12\,\mathrm{µm}$, but is larger for lower and higher widths. Even the presumed best Q_{int} at $w_{\mathrm{ind}} = 3\,\mathrm{µm}$ has eventually to be ruled out due to the immensely large error.

Due to the insufficient statement of the data and the fact that the variation of w_{ind} resulted in resonators of different size and magnetic field distribution, we chose to stay with our standard values of $w_{\mathrm{ind}} = 5\,\mathrm{µm}$ and $d_{\mathrm{wind}} = 20\,\mathrm{µm}$.

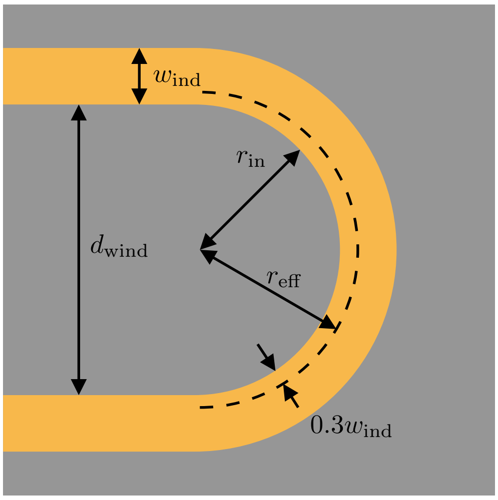

Figure 4.3.12: Schematic of a inductor winding with the most important variables for the understanding of the critical radius. When varying the width of the superconducting stripe w_{ind}, we require the effective radius to be $r_{\mathrm{eff}} = 2w_{\mathrm{ind}}$ [93].

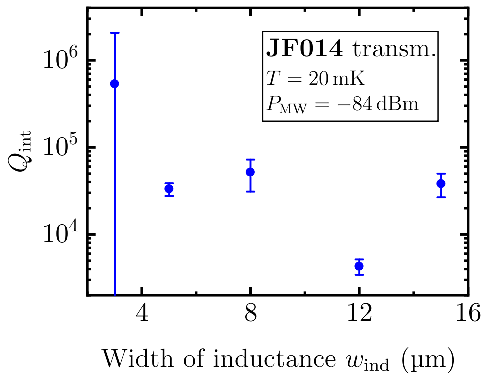

Figure 4.3.13: Resulting internal quality factors Q_{int} as a function of the width of the inductor stripe w_{ind}. The data shows no apparent trend and the error for the presumed best value $w_{\mathrm{ind}} = 3\,\mu\mathrm{m}$ is way to large to rely on.

4.3.5 Resonator Characteristics

In the following table, all fitting results of zero magnetic field measurements of the resonators presented in this work are listed. The numbering of the samples is not continuous because there were naturally samples with insufficient performance due to complications in fabrication etc., which are excluded from this work.

Sample	Material	Geom.	T (K)	P_{MW} (dBm)	Res.	f_{res} (GHz)	Q	Q_{int}	Q_{ext}
JF001	NbTiN	Transm.	4	-60	R1	3.975	12605 ± 132	66183 ± 2839	15571 ± 109
					R2	4.284	10408 ± 39	38333 ± 384	14287 ± 38
					R3	4.672	7458 ± 35	30349 ± 421	9889 ± 33
					R4	4.804	7177 ± 51	25556 ± 500	9980 ± 49
					R5	5.129	4524 ± 55	15281 ± 568	6427 ± 46
JF002	NbTiN	Refl.	4	-60	R1	3.896	24523 ± 2630	34841 ± 5211	82806 ± 2512
					R2	4.200	6992 ± 85	46808 ± 3573	8220 ± 24
					R3	4.589	13795 ± 781	27306 ± 3004	27880 ± 262
					R4	4.786	5994 ± 30	53945 ± 2507	6743 ± 13
JF003	NbTiN	Transm.	3	-60	R1	3.627	5317 ± 15	46529 ± 818	6003 ± 12
					R2	3.743	5010 ± 29	71925 ± 4650	5385 ± 20
					R3	3.838	18509 ± 398	86964 ± 7149	23514 ± 320
					R4	3.925	13444 ± 171	90124 ± 5855	15801 ± 132
					R5	4.058	26652 ± 676	69795 ± 3771	43117 ± 717
					R6	4.227	21654 ± 529	81590 ± 5622	29477 ± 505
					R7	4.292	52171 ± 1821	123899 ± 8192	90119 ± 2091
					R8	4.584	40323 ± 1142	101083 ± 5573	67084 ± 1361
JF013	Nb	Transm.	0.02	-14	R3	5.919	43526 ± 42	304913 ± 1746	50774 ± 28
JF014	Nb	Transm.	0.02	-84	R1	4.355	2295 ± 34	38274 ± 11437	2442 ± 21
					R2	4.635	1112 ± 55	4307 ± 865	1499 ± 47
					R3	4.849	2034 ± 23	51520 ± 20261	2117 ± 13
					R4	4.897	3465 ± 57	33148 ± 5553	3869 ± 35
					R5	5.024	2596 ± 24	529247 ± 1545756	2609 ± 12
JF016	Nb	Refl.	0.03	-118	R2	5.584	7177 ± 11	288473 ± 12327	7361 ± 8

Table 4.3.2: Zero magnetic field fit results of the resonators presented in Chapter 4.

4.4 Summary

Finally, we want to summarize the main statements and results of this chapter. We started by presenting the different measurement setups, which we use to characterize the thin films and measure the planar microwave resonators. We pointed out, that it is crucial to employ a circulator for measuring reflection type resonators to mitigate standing wave patterns in the recorded spectra.

We then presented transport measurements using the Van der Pauw method [23] to determine the superconducting properties of NbTiN and Nb thin films such as critical temperature T_c, width of transition ΔT and residual resistance ratio RRR. For NbTiN, we measured a T_c of about $16\,\mathrm{K}$ and $7.9\,\mathrm{K}$. From these characterization measurements, we obtained the tendency, that the Nb thin films exhibit a larger quality than the NbTiN thin films due to the smaller width of transition $\Delta T_{\mathrm{Nb}} \approx 0.01\,\mathrm{K}$ compared to the one of NbTiN $\Delta T_{\mathrm{NbTiN}} \approx 0.07\,\mathrm{K}$.

Following that, we discussed the chip preparation and discussed the between transmission and reflection type chips. Here, we encountered a position dependent behavior of the coupling between resonator and feedline. This is due to the formation of high intensity standing waves in the feedline caused by the reflective end of this geometry. For the transmission chip, we received Q_{ext} in the range of 6000 to 17 000 and for the reflection chip values ranging from 6000 to 80000.

We then discussed the influence of kinetic inductance and two level systems on the behaviors of the resonators under variations of external magnetic field, temperature and applied incident microwave power. When varying the external magnetic field, we observed magnetic field robustness of NbTiN with the internal quality factor staying rather constant around 27000, which cannot be stated for Nb, whose Q_{int} effectively collapses from 270000 at zero magnetic field down to 50000 at $200\,\mathrm{mT}$. For variations of the temperature, we observed high stability of NbTiN at elevated temperatures. At millikelvin temperatures, we investigated the influence of highly detuned TLS, which turned out to affect the resonance frequency more than the internal quality factor. We determined the components of the latter to be $Q_{\mathrm{TLS}} = 2.9 \times 10^6$ from the TLS and $Q^* = 53 \times 10^3$. Additionally, we varied the incident microwave power at the sample. For very high powers above $-20\,\mathrm{dBm}$, the resonator shows the anharmonic line shape of a duffing oscillator. At very low powers and at millikelvin temperatures, unsaturated TLS have a significant influence on the internal quality factor up to reaching high enough powers at which they saturate. The quality factors of these TLS are $Q_{\mathrm{TLS,NbTiN}} = 285 \times 10^3$ and $Q_{\mathrm{TLS,Nb}} = 1471 \times 10^3$ for each material. The non-TLS contributions to Q_{int} obtained from this measurement are $Q^*_{\mathrm{NbTiN}} = 75 \times 10^3$ and $Q^*_{\mathrm{Nb}} = 306 \times 10^3$.

In addition to these characterization measurements, we also varied geometric parameters of the resonator design to investigate their influence on external and internal coupling rate. We observed an inverse behavior of the spacing between resonator and feedline on the external coupling rate κ_{ext}. This proved that the coupling is of capacitive nature and gives us the possibility to adjust the coupling rate through w_{sep} when aiming for a certain coupling regime of the resonators. Finally, we also varied the width of the inductance stripe to observe the influence on the internal quality. Unfortunately, the data did not yield clear results, which lead us to stay at our standard resonator design with the spacing between two counter-flowing inductor branches being $d_{\mathrm{wind}} = 20\,\mathrm{\mu m}$ and an inductor width of $w_{\mathrm{ind}} = 5\,\mathrm{\mu m}$.

By performing all these measurements, we gained a profound understanding of the resonator behavior and are able to design resonators with certain characteristics. Therefore, we are able to carry out ESR experiments by using these resonators, especially in reflection geometry.

Chapter 5

Electron Spin Resonance

In this chapter, we present electron spin resonance experiments (ESR) on phosphorous donors in silicon (Si:P) by using resonators coupled to feedlines in transmission and reflection geometry. ESR experiments are performed in two fashions, continuous wave ESR (cwESR) and pulsed ESR (pESR) referring to the application of the microwave signal. In the first section, we discuss cwESR and present the measurement setup, sample preparation and the measurements. From these experiments, we obtain the working point for pESR, which is discussed in the second part of this chapter. The measurement setup for this technique is presented alongside the setup calibration. Furthermore, we show measurements that characterize the spin ensemble in terms of spin coherence time.

5.1 Continuous Wave ESR

For cwESR experiments, we place a silicon crystal containing phosphorus donors with a doping density of $[\mathrm{P}] = 2 \times 10^{17}\,\mathrm{cm}^{-3}$ on top of the planar superconducting microwave resonator. We then perform microwave spectroscopy of this hybrid system as discussed in Chapter 4. We use these experiments to identify the field range for pulsed ESR measurements. In the following, we discuss the measurement setup and sample preparation that are used for cwESR. After that, the different measurements and results are presented and discussed.

5.1.1 Measurement Setup and Sample Preparation

Measurement Setup The measurement setup for cwESR with resonators coupled to a feedline in transmission and reflection geometry is identical to the one employed for characterizing the resonators, which is shown in figure 4.1.3. The VNA is used to drive the resonator and consequently the spin ensemble with a continuous frequency band, thereby serving as the microwave source. It also records the signal coming back from the coupled system. As discussed in Chapter 4, a circulator is employed when measuring cwESR with reflection type resonators to allow the usage of attenuators and amplifiers while simultaneously reducing the standing wave signature. The built-in magnet of the cryostat plays a significant role in ESR measurements since it tunes the energy difference between the spin states of Si:P by providing the in-plane magnetic field B_0.

Sample Preparation We perform cwESR on two different samples, namely phosphorous donors in silicon (Si:P) and 2,2-diphenyl-1-picrylhydrazyl (DPPH). The samples are each placed

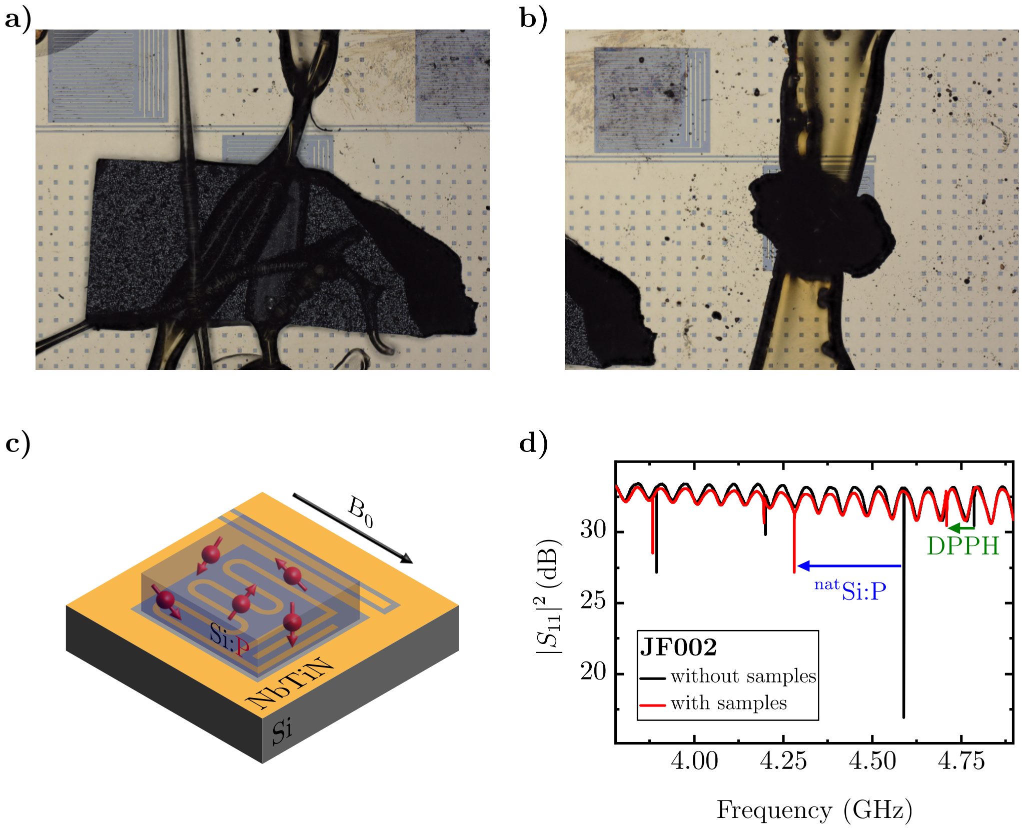

Figure 5.1.1: Sample preparation and test measurement for cwESR measurements. **a)** A sample of ^{nat}Si:P is placed on the NbTiN resonator R3 of the reflection chip "JF002". The sample is fixed by using an elastic adhesive. **b)** Granular 2,2-diphenyl-1-picrylhydrazyl (DPPH) mounted onto R4 of chip "JF002". **c)** Schematic of sample on top of the resonator for ESR measurements. An in-plane magnetic field B_0 is applied to tune the energy difference between the spin states of Si:P levels. **d)** Measurements of chip "JF002" with and without ^{nat}Si:P and DPPH on top of two resonators. The resonance frequency of the latters shift to lower values due to the presence of the samples, which changes the effective permittivity for each resonator.

on top of a resonator, as shown schematically in figure 5.1.1 c). We then fix the samples in place with rubber cement as depicted in Figure 5.1.1 a), b).

Before executing cwESR measurements, we assess whether the sample are in close contact to the resonators, which is essential as the microwave magnetic fields are spatially located close to the surface of the chip.

We employ microwave spectroscopy to this end. As our samples have a finite dielectric constant, we expect that the change the electromagnetic environment of the resonator by modifying the effective dielectric constant. By monitoring the resonance frequency of the microwave circuit and comparing it to the unloaded resonator, we can check, whether and how close the sample is to the resonator. Figure 5.1.1 d) shows exemplary data for the reflection chip JF002. The solid black line shows the data prior to mounting of the samples. After mounting of the samples, we observe a shift of one of the resonators from $4.590\,\mathrm{GHz}$ to $4.281\,\mathrm{GHz}$, which we associate with the bulk Si sample. The resonance at $4.786\,\mathrm{GHz}$ is shifted to $4.709\,\mathrm{GHz}$ which we identify as the resonator loaded with DPPH. The two remaining resonators at $3.894\,\mathrm{GHz}$ and $4.201\,\mathrm{GHz}$ only shift by few MHz, which we attribute to the slightly changed electromagnetic environment present after loading the chip. The frequency shift of the resonator loaded with the bulk silicon specimen is the most straightforward way to assess quantitatively. Since the resonance frequency is inversely proportional to the square root of the effective dielectric constant $\varepsilon_{\mathrm{eff}}$

$$f_{\mathrm{r}} \propto \frac{1}{\sqrt{\varepsilon_{\mathrm{eff}}}}. \tag{5.1}$$

and assuming that the silicon sample fully replaces the vacuum above the resonator, we can quantitatively estimate the frequency shift by

$$\frac{f^{(\mathrm{Si:P})} - f^{(\mathrm{bare})}}{f^{(\mathrm{bare})}} = \sqrt{\frac{\varepsilon_{\mathrm{eff}}^{(\mathrm{bare})}}{\varepsilon_{\mathrm{eff}}^{(\mathrm{Si:P})}}} - 1, \tag{5.2}$$

where we plug in $\varepsilon_{\mathrm{eff}}^{(\mathrm{bare})} = \frac{\varepsilon_{\mathrm{Si}}+\varepsilon_{\mathrm{vac}}}{2} = 6.45$ and $\varepsilon_{\mathrm{eff}}^{(\mathrm{Si:P})} = \varepsilon_{\mathrm{Si}} = 11.9$. Thus in the ideal scenario, we would expect a reduction of the resonance frequency by -26.4%. However, we find -6.7% which is less than expected for the ideal case. The discrepancy can be explained by a remaining gap between the surface of the chip an the Si:P crystal, potential resulting from residual particles on the chips surface. For a more detailed assessment, one can use FEM simulations of the resonator with the sample mounted on top as discussed in detail in Refs. [30, 82].

5.1.2 Measurements

In the following, we present different cwESR measurements. In addition to the experiments with phosphorous spin ensembles in silicon, we also perform ESR measurements on DPPH, which is an established g-marker. DPPH has a g-factor of $g = 2.0036$ [94, 95] and thus allows to provide a field calibration. After that, we present measurements on $^{\mathrm{nat}}$Si:P using transmission and reflection type resonators. Finally, we investigate the power dependence of the collective coupling g_{eff} and estimate the spin-lattice relaxation time T_1 by saturation recovery.

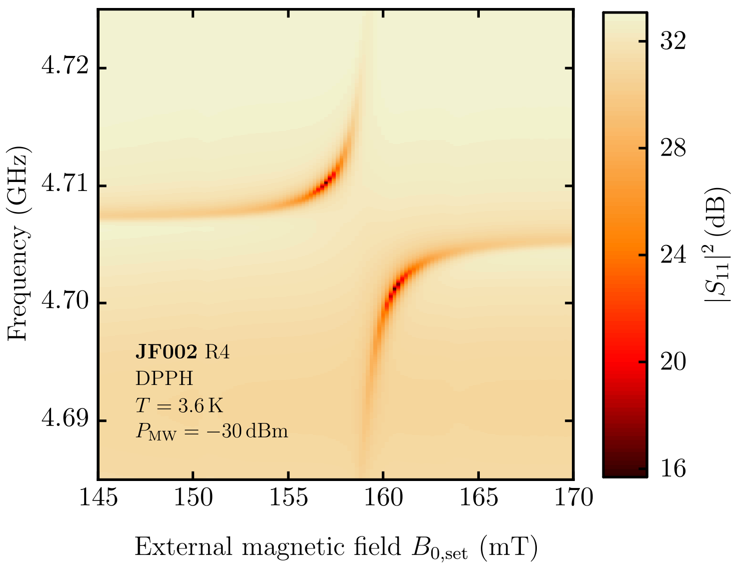

Figure 5.1.2: Heatmap of the measured $|S_{11}|^2$ data as a function of the background magnetic field B_0 from the cwESR measurement on DPPH. The outgoing signal was amplified by $35\,\mathrm{dB}$. The x-axis shows the uncalibrated set magnetic field $B_{0,\mathrm{set}}$. The ESR transition happens at $B_{0,\mathrm{meas}} = 159\,\mathrm{mT}$.

5.1.2.1 Field Calibration

Although the built-in magnet of the cryostat is per se calibrated, an additional calibration of its magnetic field at the sample B_0 is needed. This allows for measuring the Landé factor $g_{\mathrm{e,P}}$ of $^{\mathrm{nat}}$Si:P with high precision by cwESR.

The field calibration is done by measuring ESR with DPPH that is placed on one of the resonators as it is shown in figure 5.1.1 b). It is a stable free radical molecule whose unbound electron provides a $S = \frac{1}{2}$ spin system with a well known isotropic Landé factor $g_{\mathrm{e,DPPH}} = 2.0036$ [94, 95]. The resonance condition is given by:

$$hf_{\mathrm{r}} = g_{\mathrm{e,DPPH}}\mu_{\mathrm{B}}B_0. \tag{5.3}$$

Thus, the determination of the ESR resonance signature allows to perform a magnetic field calibration of the system. This is of particular importance when using superconducting magnet systems, as they are prone to capture flux during magnetic field sweeps. These add to the theoretically computed field based on the applied current to the system.

Figure 5.1.2 shows the measured cwESR data of DPPH. We observe the microwave resonator as light red signature which is nearly constant in frequency between $145\,\mathrm{mT}$ and $152\,\mathrm{mT}$. At around $155\,\mathrm{mT}$ to $162\,\mathrm{mT}$, we observe a distinctive modification of the resonator in form of an avoided crossing. While for conventional ESR, we would only expect a slight modification of the resonator parameters, in particular the linewidth of the resonator, we here observe a strong collective coupling. We extract the measured magnetic field $B_{0,\mathrm{meas}}$ from the center of the transition by hand and yield $B_{0,\mathrm{meas}} = 159\,\mathrm{mT}$, which is lower than the expected field of transition of

$167.866\,\mathrm{mT}$. We interpret this as a magnetic field offset $\Delta B_0 = B_{0,\text{theo}} - B_{0,\text{meas}} = 8.866\,\mathrm{mT}$, which we will use later to present our data on a calibrated field scale.

5.1.2.2 Transmission and Reflection Measurement

We now present cwESR measurements on ${}^{\text{nat}}$Si:P samples that have a phosphorous concentration of $[\mathrm{P}] = 2 \times 10^{17}\,\mathrm{cm}^{-3}$. The measurements were done once with a NbTiN transmission type resonator at liquid helium temperatures and once with Nb reflection type resonator at millikelvin temperatures. We therefore cover all possible materials, resonator geometries and temperature regimes for ESR measurements.

Transmission First, we discuss the measurement in transmission geometry. The employed NbTiN resonator chip with resonators coupled to a transmission type feedline was fabricated during the work of Müller [18] and will be referred to as just "transmission chip" in the following. We can estimate the values for the magnetic fields of of the ESR transitions based on the energy differences of the spin states as shown in Chapter 2.2.1. Then, the S_{21}-parameter of the resonator-spin-ensemble-system at resonance is measured as a function of the magnetic field in a region containing the expected fields of transitions. The resulting two-dimensional data measured at temperature $T = 3.6\,\mathrm{K}$ and incident microwave power $P_{\text{MW}} = -100\,\mathrm{dBm}$ is shown in figure 5.1.3 a).

We observe a decrease of the resonance frequency with increasing external magnetic field, which we expect based on the measurements presented in Chapter 4.3.2.1. However, we observe two signatures in the data around $172.6\,\mathrm{mT}$ and $176.6\,\mathrm{mT}$, which we identify as the low and high field ESR transitions. Here, the resonance dip of the resonator has a lower amplitude and broadens. This broadening is caused by the coupling of the resonator to the spin ensemble, which acts as an additional loss channel to the resonator. It is described by the additional term in the denominator of equation (2.80), which was derived using the input-output formalism. Consequently, the total loss rate increases when the resonator is in resonance with the spin ensemble.

We can extract the total coupling rate κ by fitting the $|S_{21}|^2$ spectrum for each measured magnetic field. Based on equations (2.36) and (2.80), we employ the fit function:

$$|S_{21}(\omega)|^2 = a \cdot \left| 1 + \frac{\kappa_{\text{ext}} e^{i\phi}}{i(\omega_{\text{r}} - \omega) - \kappa_{\text{ext}} - \tilde{\kappa}} \right|^2, \tag{5.4}$$

where we plugged in the redefined total coupling rate given by:

$$\kappa = \kappa_{\text{ext}} + \tilde{\kappa} = \kappa_{\text{ext}} + \kappa_{\text{int}} + \kappa_{\text{spin}}. \tag{5.5}$$

This definition includes the loss contribution and the change in resonance frequency caused by the spin ensemble $\kappa_{\text{spin}} = \frac{g_{\text{eff}}^2}{i(\omega_{\text{s}} - \omega) - \gamma_{\text{s}}}$, that is non-negligible near spin resonance. We stress that we use κ_{ext}, $\tilde{\kappa}$ as fit parameters instead of κ_{ext} and κ. By doing so, we make sure that $\kappa = \kappa_{\text{ext}} + \tilde{\kappa} > \kappa_{\text{ext}}$ is fulfilled. However, we stress that κ_{spin} is actually complex. The total

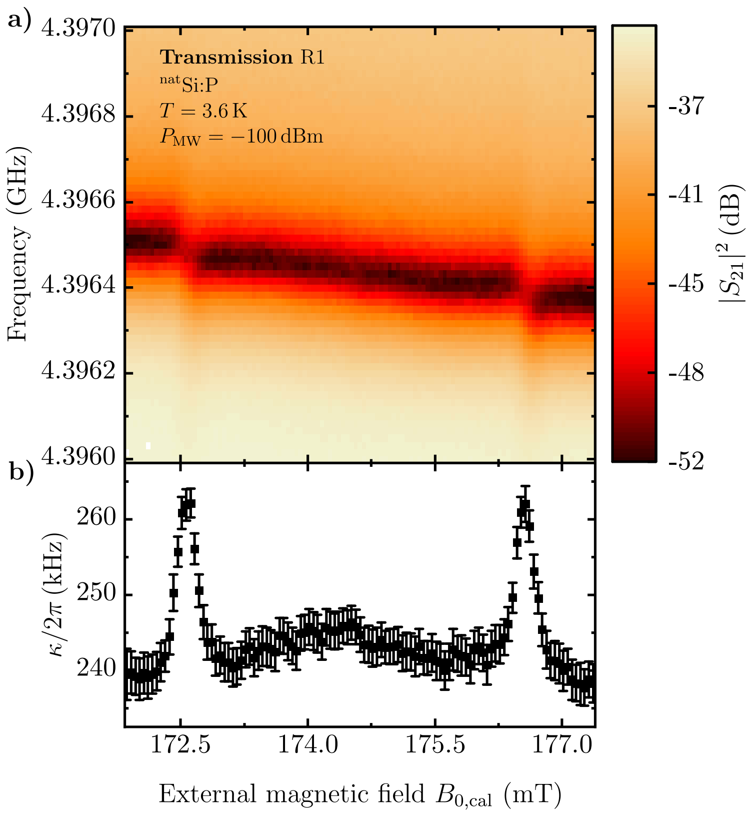

Figure 5.1.3: Continuous wave ESR measurement on a ${}^{\mathrm{nat}}$Si:P sample measured with resonator R1 of the NbTiN transmission chip. **a)** Measured $|S_{21}|^2$ data around the resonance frequency for different applied magnetic fields B_0. ESR transitions happen near $172.6\,\mathrm{mT}$ and $176.6\,\mathrm{mT}$. **b)** Total coupling rate $\kappa/2\pi$ as function of the magnetic field B_0. The data was obtained by fitting equation (5.4) to the $|S_{21}|^2$ spectra above. Two peaks occur at the magnetic fields of the ESR transitions, since the spin system contributes to the resonator losses when in resonance to the latter.

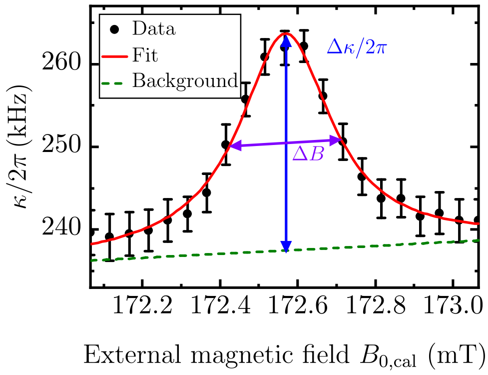

Figure 5.1.4: Fitted low field transition peak from figure 5.1.3 b). The peak is fit using a Lorentzian curve with an additional linear background described in equation (5.6) to extract the FWHM ΔB, the center of the peak B_c and the amplitude of the Lorentzian curve alone $\Delta\kappa/2\pi$.

coupling rate is then given by the sum of these two[1].

The resulting spectrum of κ is shown in figure 5.1.3 b). We can clearly see two peaks in the spectrum, that are located at the same magnetic fields of the ESR signatures in the $|S_{21}|^2$ data shown above. From these peaks, we can extract various information about the spin system. We fit a Lorentzian curve with an additional linear background to the peaks. The fitting function reads:

$$\frac{\kappa}{2\pi}(B_0) = A \cdot \frac{2}{\pi}\frac{\Delta B}{4(B_0 - B_c)^2 + \Delta B^2} + m \cdot B_0 + \kappa_0, \tag{5.6}$$

where A is an amplitude, ΔB is the linewidth, B_c is the center of the peak, m is the slope and κ_0 the offset of the linear background. The amplitude of the Lorentzian curve $\Delta\kappa/2\pi$ with the linear background subtracted is then given by:

$$\frac{\Delta\kappa}{2\pi} = \frac{2A}{\pi\Delta B}. \tag{5.7}$$

An exemplary fit of the low field transition peak measured with the transmission chip is shown in figure 5.1.4.

From fitting the peaks, we extract the calibrated fields $B_{0,\mathrm{lf}}^{\mathrm{cal}} = 172.57\,\mathrm{mT}$ and $B_{0,\mathrm{hf}}^{\mathrm{cal}} = 176.56\,\mathrm{mT}$ for the low field and high field transition, respectively. Therefore, the transitions are separated by $3.99\,\mathrm{mT}$. To compare this value to the expected one from theory, we can write the resonance condition in good approximation as:

$$\omega_{\mathrm{s}} = \gamma_{\mathrm{e,P}} B_0 \pm \frac{A}{2\hbar}, \tag{5.8}$$

where $\gamma_{\mathrm{e,P}} = g_{\mathrm{e,P}} \frac{\mu_{\mathrm{B}}}{\hbar}$ is the gyro magnetic ratio of phosphorous in silicon and $A/\hbar = (2\pi \cdot 117.53)\,\mathrm{MHz}$ is the hyperfine constant of phosphorous [36]. Based on this expression, we expect the ESR transitions to be separated by $A/\hbar\gamma_{\mathrm{e,P}} = 4.20\,\mathrm{mT}$. We see that the measured field

[1]The fitting error is calculated via $\Delta\kappa = \sqrt{(\Delta\kappa_{\mathrm{ext}})^2 + (\Delta\tilde{\kappa})^2}$

Transition	ΔB (mT)	$\Delta\kappa/2\pi$ (kHz)	$\gamma_s/2\pi$ (kHz)	$g_{\text{eff}}/2\pi$ (kHz)
low field	0.287 ± 0.016	26.2 ± 1.6	7301.0 ± 425.6	309.1 ± 39.9
high field	0.263 ± 0.016	23.8 ± 1.5	3272.2 ± 197.6	279.3 ± 36.3

Table 5.1.1: Characteristics of the spin ensemble obtained from fitting the transition peaks from the cwESR measurement with the transmission chip. Especially the spin loss rates γ_s of the transitions deviate from each other.

spacing between the peaks deviates by $0.21\,\text{mT}$.

We then calculate the measured Landé factor from our measurements. We do not calculate this value for each transition but use the approach that uses the center field $B_{\text{center}} = (B_{0,\text{lf}}^{\text{cal}} + B_{0,\text{lf}}^{\text{cal}})/2$ from the measured magnetic fields of transition and the center resonance frequency $f_{\text{r,center}} = (f_{\text{r,lf}} + f_{\text{r,lf}})/2$. This results in

$$g_{\text{e,P}}^{\text{meas}} = \frac{h f_{\text{r,center}}}{B_{\text{center}}\mu_{\text{B}}} = 1.7994, \tag{5.9}$$

which deviates from the literature value $g_{\text{e,P}} = 1.9985$ [36]. The main reason might lay in the sweeping of the magnetic field and potential trapped flux in the cryostat caused by the built-in magnet that can generate magnetic field magnitudes up to $17\,\text{T}$. This might also affect the field calibration measurement with DPPH, so the calibration might be inaccurate as well.

Next, we extract the effective collective coupling g_{eff} between resonator and spin system and the cooperativity C. According to [96], we can calculate g_{eff} via:

$$g_{\text{eff}} = \sqrt{\gamma_s \Delta\kappa}, \tag{5.10}$$

where γ_s is the spin loss rate that is connected to the linewidth ΔB via:

$$\gamma_s = \gamma_e \frac{\Delta B}{2}. \tag{5.11}$$

The resulting coupling rates are listed in table 5.1.1. We notice a remarkable difference between the spin loss rates of both transitions. However, the collective coupling rates g_{eff} are identical within the scope of their uncertainty and comparable to literature values [9].

The cooperativity is calculated by plugging these values into equation (2.82) alongside with the off-resonant total coupling rate $\kappa_{\text{offres}}/2\pi = (239.4 \pm 3.4)\,\text{kHz}$ measured at $B_0 = 171.866\,\text{mT}$. We find $C_{\text{lf}} = 0.109 \pm 0.029$ and $C_{\text{hf}} = 0.100 \pm 0.027$ for the transitions. These values also agree with each other within their uncertainties. With these results, we can state that this measurement configuration operates in the weak coupling regime due to the cooperativity being notably below 1.

Reflection Next, we discuss the cwESR measurement on $^{\text{nat}}$Si:P measured with a Nb reflection type resonator at millikelvin temperature. The measurement procedure is identical to the measurement with the transmission chip. The measurement was conducted with the resonator R3 of the chip "JF016" at a temperature of $T = 80\,\text{mK}$ and applied microwave power at the chip

Transition	ΔB (mT)	$\Delta\kappa/2\pi$ (kHz)	$\gamma_s/2\pi$ (kHz)	$g_{\text{eff}}/2\pi$ (kHz)
low field	0.152 ± 0.005	1652.9 ± 49.2	2137.2 ± 67.1	1879.5 ± 164.9
high field	0.166 ± 0.001	1347.8 ± 31.6	2286.4 ± 55.9	1755.5 ± 136.1

Table 5.1.2: Characteristics of the spin ensemble obtained from fitting the transition peaks from the cwESR measurement with the reflection chip "JF016".

of $P_{\text{MW}} = -148\,\text{dBm}$. In this millikelvin setup, no field calibration using DPPH was made, so the shown values of the magnetic field are always the ones we set the magnet to.

Figure 5.1.5 a) shows the measured $|S_{11}|^2$ data. We see two avoided crossings in the data, at which the resonance dip seems to split up into two branches at each signature. These features in the data represent the ESR transitions. In contrast to the transmission cwESR measurement, we can clearly see these avoided crossings that the simulation shown in figure 2.3.2 suggests. This fact provides a first hint that the coupling between resonator and spin ensemble is larger in this measurement configuration.

To extract the spectrum of the total coupling rate κ, we also fit the $|S_{11}|^2$ data for each measured magnetic field B_0. Since this is a reflection type resonator, an additional factor of 2 has to be added to the nominator of equation (5.4) used to fit transmission data. The resulting fit function for reflection measurements that is based on equations (2.39) and (2.81) then reads:

$$|S_{11}(\omega)|^2 = a \cdot \left|1 + \frac{2\kappa_{\text{ext}} e^{i\phi}}{i(\omega_r - \omega) - \kappa_{\text{ext}} - \tilde{\kappa}}\right|^2. \tag{5.12}$$

The data obtained from the fit is shown in figure 5.1.5 b). We also see two peaks indicating the spin transitions. When comparing this data with the transmission one of figure 5.1.3 b), it is evident that the magnitude of these peaks here are significantly larger than those of the transmission measurement.

The peaks are fit by equation (5.6). We extract the fields $B_{0,\text{lf}}^{\text{uncal.}} = 180.39\,\text{mT}$ and $B_{0,\text{hf}}^{\text{uncal.}} = 184.58\,\text{mT}$ for the low field and high field transition, respectively. Consequently, the two transitions are separated by $4.19\,\text{mT}$, which is in excellent agreement with the theoretical value of $4.20\,\text{mT}$. By using equation (5.9), we obtain the Landé factor to be $g_{\text{e,P}}^{\text{meas}} = 1.9908$. This value does also not agree with the reported value of $g_{\text{e,P}} = 1.9985$ [36]. The reason for this might be the missing calibration of the magnetic field of this setup.

The calculated coupling rates obtained from the Lorentzian fit and the use of equations (5.11) and (5.10) are listed in table 5.1.2. We notice that these values are very similar for each transition. The larger amplitudes of the Lorentzian peak $\Delta\kappa/2\pi$ consequently lead to effective coupling rates $g_{\text{eff}}/2\pi$ that are an order of magnitude higher than the ones measured with the transmission chip. The cooperativities yielded through equation (2.82) and the off-resonant total coupling rate $\kappa_{\text{offres}}/2\pi = 663.6\,\text{kHz}$ for this measurement configuration are $C_{\text{lf}} = 2.491 \pm 0.460$ and $C_{\text{hf}} = 2.031 \pm 0.334$. They agree within their uncertainty and are higher than 1, meaning that this resonator-spin-ensemble system operates in the strong coupling regime. However, in the strong coupling regime, one typically should not be able to fit the data in the region of the field transitions since the branches split up and consequently, there are two lorentian dips in these spectra. One then would extract g_{eff} via the spacing of these two dips at resonance [7]. However,

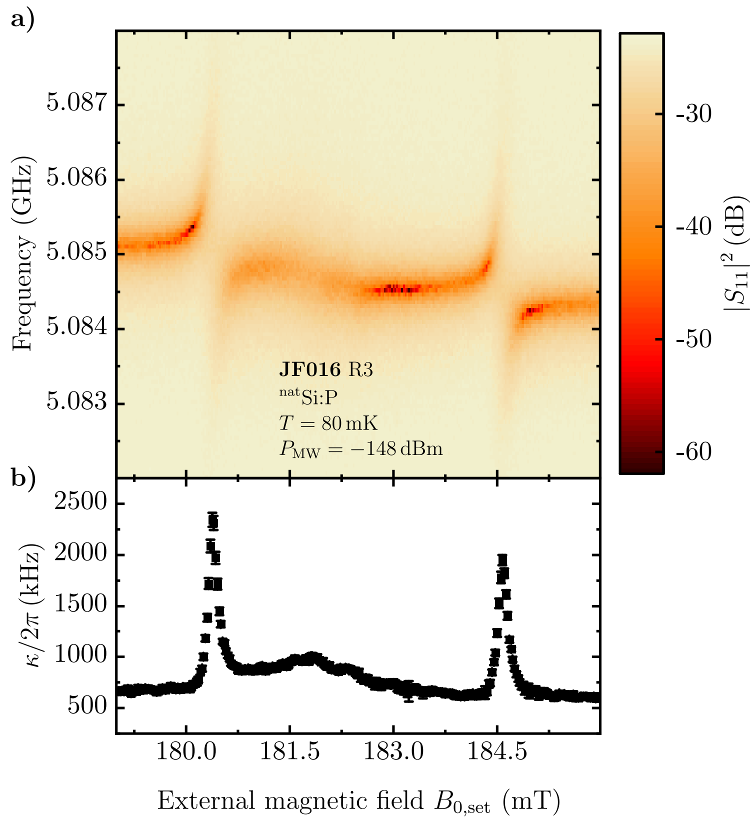

Figure 5.1.5: Continuous wave ESR measurement on a $^{\mathrm{nat}}$Si:P sample with reflection type resonator R3 of the Nb chip "JF016". **a)** Measured $|S_{11}|^2$ data around the resonance for different applied magnetic fields B_0. Two avoided crossings indicate the ESR transitions. **b)** Total coupling rate $\kappa/2\pi$ as a function of the magnetic field B_0. The data was obtained from fitting equation (5.12) to the $|S_{11}|^2$ spectra shown above for each measured magnetic field. The two peaks arise from the coupling to the spin ensemble when the system is near resonance.

we did not observe said splitting when fitting the spectra and the fit routine did not fail.

Consequently, we simulate the cwESR spectrum of the low field transition based on equation (2.81) together with the eigenenergies from Chapter 2.2.1 and the measured results from Tab. 5.1.2. The data is shown in Figure 5.1.6. Although both the simulated and the measured cwESR spectra yield the same cooperativity $C = 2.491$, they look different. We observe that the slope of the spin excitation mode is significantly lower in the simulated data than in the measured data. The reason for these differences needs further investigation, which is why one should treat these results with caution.

The main reason for the higher effective coupling g_{eff} and consequently also higher cooperativity C is the lower temperature at which the reflection measurement was performed. This is due to the fact, that g_{eff} is proportional to the thermal spin polarization discussed in Chapter 2.6.

By means of Figure 2.6.1, we can see that for the measurement conducted with the transmission resonator at $T = 3.6\,\mathrm{K}$, the thermal spin polarization for both transitions is just a few

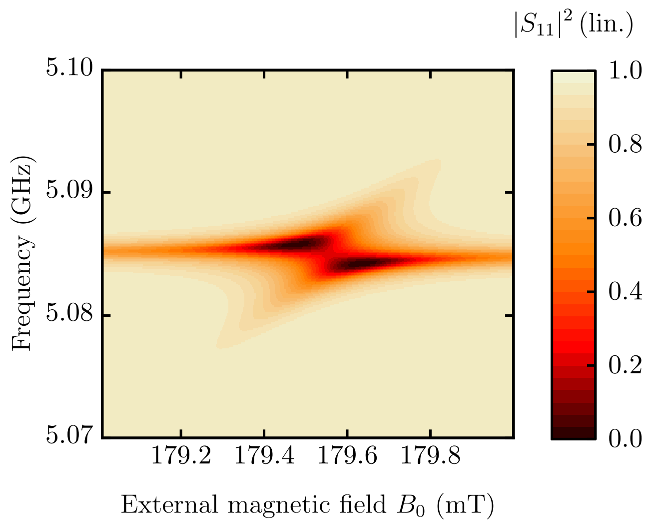

Figure 5.1.6: Simulated $|S_{11}|^2$ data in linear scale of the low field transition of Si:P based on equation (2.81) and the parameters from the measurement with JF016 (see Tab. 5.1.2 and text). The spin excitation mode shows a different slope in the simulation than the measurement.

percents. This is way lower than the spin polarizations of the reflection measurement executed at $80\,\mathrm{mK}$, which are around 50%. Therefore, the difference in the collective coupling rate g_{eff} between the two measurements is explained by the different thermal spin polarization.

5.1.2.3 Power Dependent cwESR

After having successfully measured cwESR on $^{\text{nat}}$Si:P in two different measurement configurations, we also investigate the effect of the incident microwave power at the sample on the effective collective coupling rate g_{eff} between resonator and spin ensemble.

Based on the considerations of Chapter 2.7, we performed cwESR measurements on $^{\text{nat}}$Si:P in both measurement configurations from the previous chapter. The measurements were conducted at different incident microwave powers at the sample ranging from $-120\,\mathrm{dBm}$ to $-50\,\mathrm{dBm}$ for the transmission chip and ranging from $-148\,\mathrm{dBm}$ to $-88\,\mathrm{dBm}$ for the reflection chip, respectively in steps of $5\,\mathrm{dBm}$. The resulting data for g_{eff} is shown in figure 5.1.7 and was calculated as in the previous section.

The general course of g_{eff} is identical for both measurement configurations. For very low incident microwave powers, the effective collective coupling rate exhibits only a weak dependence. However, it decreases quite rapidly for increasing powers, which is due to the saturation of the spin ensemble discussed above. We observe that it takes lower absolute powers until a notable drop off in g_{eff} sets in for the measurement performed with the reflection measurement at millikelvin temperatures. The reason for this behaviour is given by a higher spin-lattice relaxation time T_1. Due to its inverse proportionality to the temperature stated in equation (2.103), T_1 is larger at millikelvin temperatures and it consequently takes lower incident microwave powers to saturate the spin ensemble. To realize high effective collective coupling rates, low incident

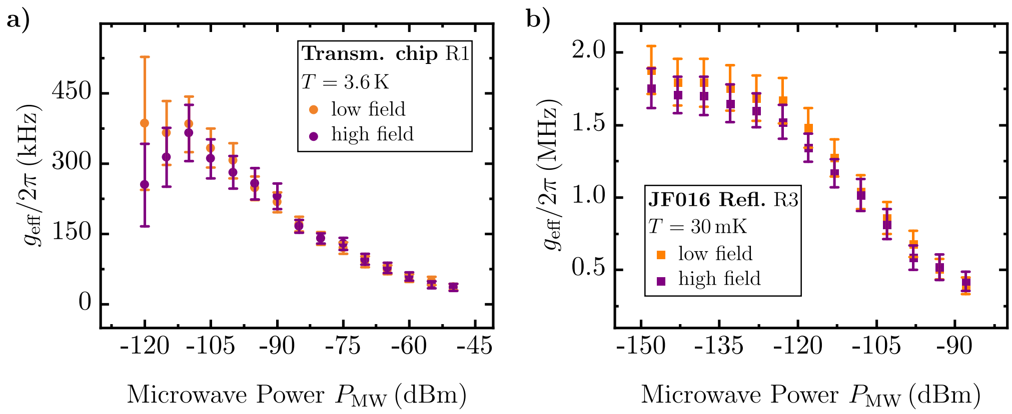

Figure 5.1.7: Measured power dependence of the collective coupling rate g_{eff} in cwESR measurements for each spin transition. **a)** Measured g_{eff} of the $^{\mathrm{nat}}$Si:P sample on top of the transmission type resonator at liquid helium temperatures. The coupling decreases with increasing incident microwave power. **b)** Results from the millikelvin measurement of $^{\mathrm{nat}}$Si:P sample on top of a reflection type resonator. At very low powers, the power dependency is very weak. For higher powers, g_{eff} decreases drastically as well.

microwave powers are sufficient.

5.1.3 Estimation of Spin-Lattice Relaxation Time

We also performed a measurement to estimate the spin-lattice relaxation time T_1 of the $^{\mathrm{nat}}$Si:P sample by means of cwESR with the reflexion chip "JF016". For this purpose, we apply the principle of cw saturation recovery [97]. Hereby, the spin ensemble is driven into saturation by a higher power pulse. Following the pulse, the relaxation of the spin system is measured over time at very low power.

Before doing that, we measure cwESR for incident microwave powers at the sample P_{MW} from $-138\,\mathrm{dBm}$ to $-68\,\mathrm{dBm}$ is steps of $2\,\mathrm{dBm}$ at the low field transition. The measured $|S_{11}|^2$ data over the incident microwave power at the sample is shown in figure 5.1.8 a) and $|S_{11}|^2$ spectra for three different powers are shown in 5.1.8 b). The data has been normalized for better comparison. We notice that the resonance frequency shifts to lower values and the resonance dip becomes more narrow with increasing incident microwave power. The latter effect can be explained with the saturation of the spin ensemble. When saturated, the coupling to the spin ensemble is suppressed and its loss contribution to the resonator is reduced, resulting in a more shallow and more narrow resonance dip of the microwave resonator. Additionally, we observe extraordinary high amplitude resonance signatures for incident microwave powers from $-100\,\mathrm{dBm}$ to $-80\,\mathrm{dBm}$. We attribute this to the observation, that the absorption depth of microwave resonator depends on the ratio of κ_{ext} and κ_{int}. When considering the contribution of the spin ensemble in form of a κ_{spin}, we can create the situation that $\kappa_{\mathrm{int}} + \kappa_{\mathrm{spin}} = \kappa_{\mathrm{ext}}$ and hence we observe critical coupling.

From figures 5.1.8 a) and 5.1.7 b), we can see that we do not necessarily need to apply a higher power pulse to saturate the spin ensemble since the cw probe signal at $-68\,\mathrm{dBm}$ is

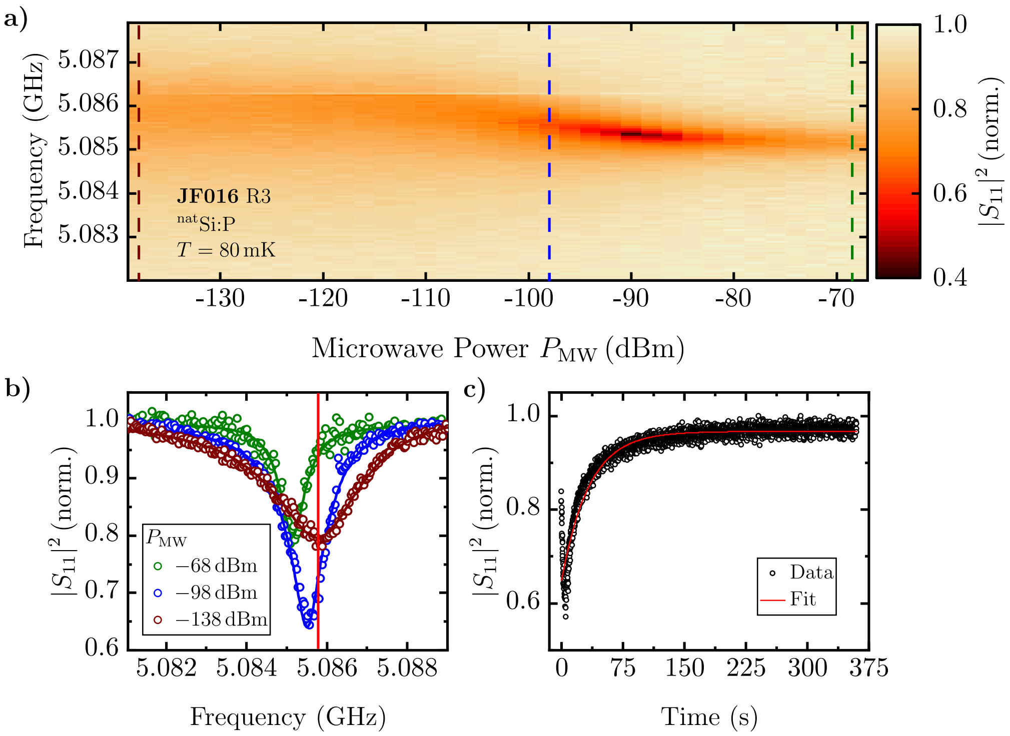

Figure 5.1.8: cwESR measurement data for the estimation of the spin-lattice relaxation time T_1 by cw saturation recovery [97]. **a)** Measured $|S_{11}|^2$ data for various applied microwave powers P_{MW}. The resonance frequency shifts due to the increasing power. **b)** $|S_{11}|^2$ data for three different applied powers. For estimating T_1, the values of the curves at the resonance frequency of the lowest incident microwave power is used (intersections with the red line). **c)** $|S_{11}|^2$ data as a function of time after saturating the spin ensemble. The data is normalized and measured with an incident microwave power at the sample $P_{\mathrm{MW}} = -138\,\mathrm{dBm}$. An exponential saturation is observed and fit by equation (5.13) to yield $T_1 \approx 33\,\mathrm{s}$.

already sufficient for reaching saturation. We therefore measure cwESR saturation recovery at $T = 80\,\mathrm{mK}$ as follows: First, we measure the S_{11}-parameter at the highest possible power with the VNA to saturate the spin ensemble. Following that, we measure the relaxation of the spin ensemble by measuring S_{11} over time at the lowest possible power, which is $-138\,\mathrm{dBm}$. We then take the values of the S_{11}-parameter spectra at the low power resonance frequency, which are the intersections of the spectra with the red vertical line in 5.1.8 b), and normalize the data to the value measured for full relaxation.

The resulting data is shown in figure 5.1.8 d) with the normalized $|S_{11}|^2$ data as a function of time. Overall, we observe an exponential dependence with saturation value of about 1. However, the time dependence of $|S_{11}|^2$ is quite complex. Stating from an initial value of 0.8 at $t = 0\,\mathrm{s}$, the $|S_{11}|^2$ initially decreases until it reaches its minimum at $t = 5\,\mathrm{s}$. Then we observe an monotonic increase until the $|S_{11}|^2$ reaches its normalization value of 1. We note that $|S_{11}|^2$ is not directly proportional to the spin polarization, but the situation is more complex. This can be anticipated by revisiting equation (2.81). Here, we note that the $|S_{11}|^2$ depends on g_{eff}, which itself it proportional to $\sqrt{P}$. Hence, for a quantitative analysis of T_1, we would need to translate the measured data to a $P(t)$ dependence and then analyse the data with an exponential relaxation back to the thermal state. However, for a first estimate for the relaxation time at play, we go a more experimental route and fit $|S_{11}|^2$ to an exponential saturation function

$$|S_{11}|^2(t) = A - B \cdot \exp\left\{-\frac{t}{T_1}\right\}, \tag{5.13}$$

where the amplitude A accounts for the saturation value not being exactly 1 due to normalization and B accounts for the minimum value not being 0 for $t = 0\,\text{s}$.

From the fit, we yield a spin-lattice relaxation time of $T_1 \approx 33\,\text{s}$. Comparing these values to literature turns out to be challenging since T_1 highly depends on the concentration of phosphorous donor atoms [98]. However, for concentrations in the order of $10^{17}\,\text{cm}^{-3}$ like in our case, T_1 is in the order of of $1\,\text{s}$ for temperatures of $1.25\,\text{K}$ [98] and $1.4\,\text{K}$ [99], respectively. Judging from these values measured at higher temperatures than in the case of this measurement, it is intuitive that our estimated value for T_1 is larger due to the lower temperature. A more in depth discussion about measuring and estimating T_1 for a similar sample can be found in the supplemental material of Ref. [7].

5.2 Pulsed ESR

In this section, we deal with the second measurement technique, which is pulsed electron spin resonance (pESR). First, we present the measurement setup and the characterization procedure. We then show measurements using the Hahn-Echo pulse sequence for measuring spin echos and the coherence time of the spin system.

5.2.1 Measurement Setup and Characterization

Measurement Setup The measurement setup used for pulsed ESR experiments at liquid helium temperatures in transmission geometry is schematically depicted in figure 5.2.1. A $10\,\text{MHz}$ signal provided by a reference clock is used to synchronize and stabilize the phase between all devices. The pulse generating arbitrary waveform generator (AWG, Keysight M8190A 12GSa/s) is initially triggered by a pulse blaster card (PBC). The AWG then triggers the analog-to-digital converter (ADC) before sending out the pulses, so it is ready to detect signals in the correct time frame. The outgoing pulses from the AWG are split up in in-phase (I) and $90°$ phase shifted quadrature (Q) signals at an intermediate frequency of $f_{\text{IF}} = 50\,\text{MHz}$. These signals are then upconverted to radio frequency (RF) by a vector source (Rohde & Schwarz SGS100A). This device consists of an IQ modulator and a built-in local oscillator source (LO). The frequency f_{LO} of the internal LO is set accordingly to the obtain the target resonance frequency of the hybrid system f_{s} given by:

$$f_{\text{s}} = f_{\text{LO}} + f_{\text{IF}}. \tag{5.14}$$

The signal is then attenuated by $-30\,\text{dB}$ and guided to the sample in the cryostat, which is at a temperature $T = 3.6\,\text{K}$. The background magnetic field B_0 at the sample as well as the

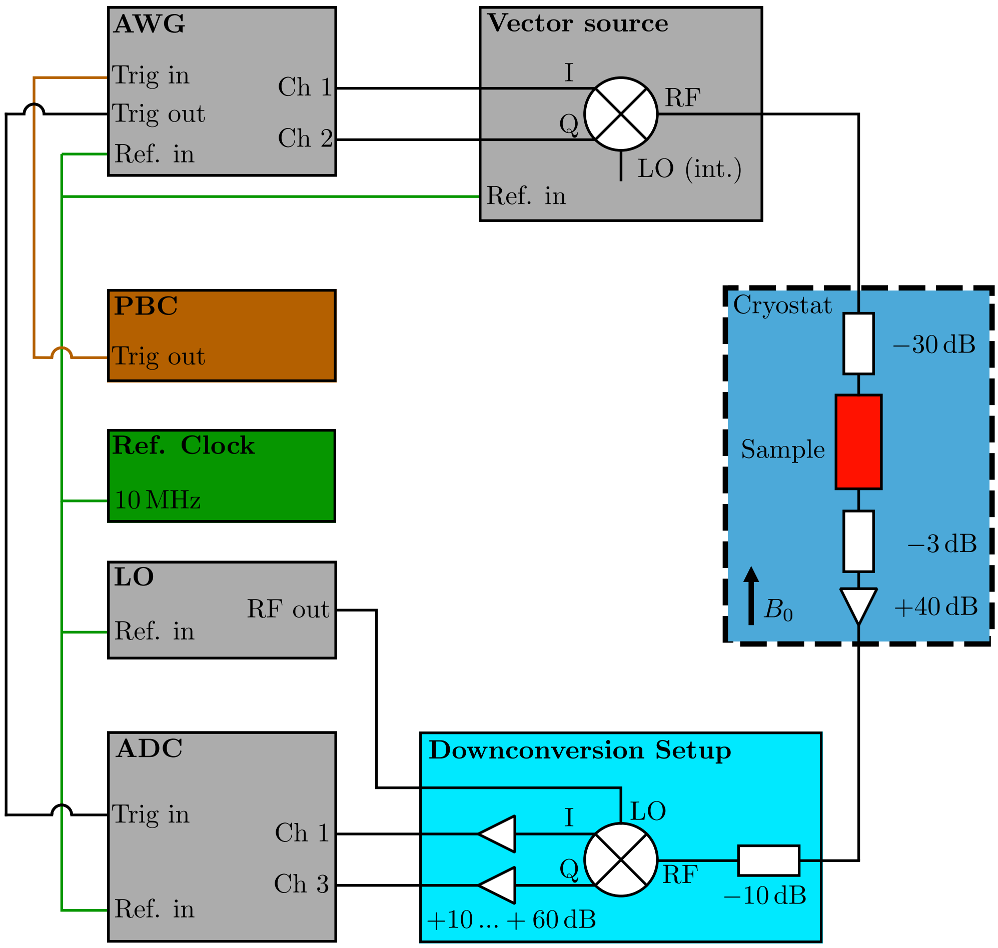

Figure 5.2.1: Schematic of the measurement setup used for pESR measurements. The pulses are generated by an arbitrary waveform generator (AWG) at an intermediate frequency. They then are upconverted to the corresponding ESR frequency before reaching the sample in the cryostat. Signal coming back from the sample is downconverted to the intermediate frequency and subsequently recorded by an analog-to-digital converter (ADC).

resonance frequency of the resonator-spin-ensemble system is set to the values obtained from previous cwESR measurements, e.g. the ones dicussed in Chapter 5.1.2.2.

Signals coming from the sample pass a -3 dB attenuator before being amplified by $+40$ dB and then reach the downconversion setup. This setup consists of a -10 dB attenuator, an IQ mixer (Marki microwave MLIQ-0416L), an external LO source (Keysight E8257D) and two variable voltage amplifiers (FEMTO DHPVA) which are placed at the I and Q outputs of the IQ mixer. The downconversion of the signal follows the inverted logic described above for the upconversion. Eventually, the amplified I and Q signals are recorded by the ADC.

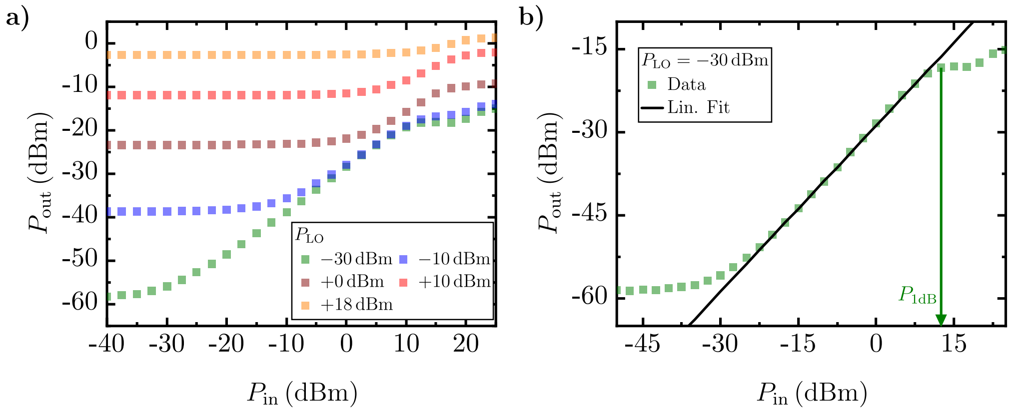

Figure 5.2.2: Measurements of the 1 dB-compression points at the I-port of the downconversion setup. **a)** Recorded data for different powers of the external LO source. The linear regime becomes more narrow with increasing LO power. **b)** Exemplary procedure to yield the 1 dB-compression point for an LO power of -30 dBm. The linear function with a fixed slope of 1 is used to extrapolate the linear regime to determine the compression point by means of equation (5.15). All results as well as the ones from the characterization of the Q-port are listed in table 5.2.1.

Setup Characterization We want to operate our setup in the linear regime, so an increase in microwave power at the input of any device in the setup should lead to an identical increase in its output power. Unfortunately, some devices exhibit nonlinear behaviors for too high input powers. In our setup, nonlinearities are mainly caused by the IQ mixer and the amplifiers of the downconversion setup.

In order to determine an upper limit for the input power to avoid nonlinear behavior, we need to measure the so called 1 dB-compression point of these devices [100]. It is defined as the input P_{1dB} at which the actual output of the device deviates by 1 dB from the value expected from extrapolation of the linear regime P_{lin}:

$$P_{out}(P_{1dB}) = P_{lin}(P_{1dB}) - 1\,\mathrm{dB}. \tag{5.15}$$

We define the upper limit for operating the mentioned devices in the linear regime as 6 dB below their compression point.

The measurement procedure for the characterization is as follows: The AWG sends a continuous sine signal at a frequency of 50 MHz. The amplitude of the two signals is set to 1.1 V so that the output power of the vector source is identical to the set one. The LO frequencies of both vector and external source of the downconversion setup is set to (de)modulate a RF signal of 5 GHz. Since we only characterize the microwave devices, we bypass the cryostat by directly connecting the RF output of the vector source with the RF input of the downconversion setup (the -10 dB attenuator) for these measurements. To detect the output power, we employ the Rohde & Schwarz power sensor ZRP-N31.

For characterizing the IQ mixer, the power sensor is directly connected to its I- and Q-port. The measurement at the I-port for different powers of the LO source P_{LO} is shown in figure 5.2.2 a). We observe a narrowing of the linear regime of the IQ-mixer when increasing P_{LO}. We

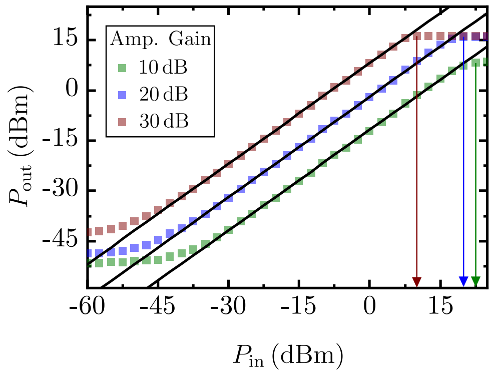

Figure 5.2.3: Characterization measurement of the variable voltage amplifier placed at the I-port of the IQ-mixer. The 1 dB-compression point for a set gain of 30 dB is significantly lower than the ones measured for other gains due to the amplifier being driven into saturation. All results as well as the ones from the measurement of the amplifier placed at the Q-port are listed in table 5.2.1.

P_{LO}(dBm)	$P_{\text{1dB,I}}$ (dBm)	$P_{\text{1dB,Q}}$ (dBm)
-30	12.5	15
-10	10	15
0	17.5	17.5
10	17.5	17.5
18	20	20
Amplifier Gain (dB)	$P_{\text{1dB,I}}$ (dBm)	$P_{\text{1dB,Q}}$ (dBm)
10	22.5	22.5
20	20	20
30	10	10

Table 5.2.1: Resulting 1 dB-compression points measured directly at the I- and Q-ports of the down-conversion setup at different powers P_{LO} of the LO and for different gains of the amplifiers placed at the same ports.

discuss the procedure of determining the 1 dB-compression point for the data set measured at $P_{\text{LO}} = -30\,\text{dBm}$, which is shown in figure 5.2.2 b). A linear function with a fixed slope of 1 is fitted to the linear regime of the data. This function effectively extrapolates the linear regime and serves as a reference to determine the compression point with equation (5.15). For this data set, we find $P_{\text{1dB}} = 12.5\,\text{dBm}$. The so obtained compression points for the other LO powers as well as the results from the measurement at the Q-port are listed in table 5.2.1.

For the characterization of the variable voltage amplifiers, they are placed at the I(Q)-port of the IQ-mixer and the power sensor is placed at their output. We perform the same measurement as described before for set gains of 10 dB, 20 dB and 30 dB. The recorded data as well as the linear fits for the measurement of the amplifier placed at the I-port is shown in figure 5.2.3. We find $P_{\text{1dB,10dB}} = 22.5\,\text{dBm}$, $P_{\text{1dB,20dB}} = 20\,\text{dBm}$ and $P_{\text{1dB,30dB}} = 10\,\text{dBm}$. We note that the compression point obtained for a set gain of 30 dB is significantly lower than the other ones. This is due to the amplifier being driven into saturation, which becomes more evident by the

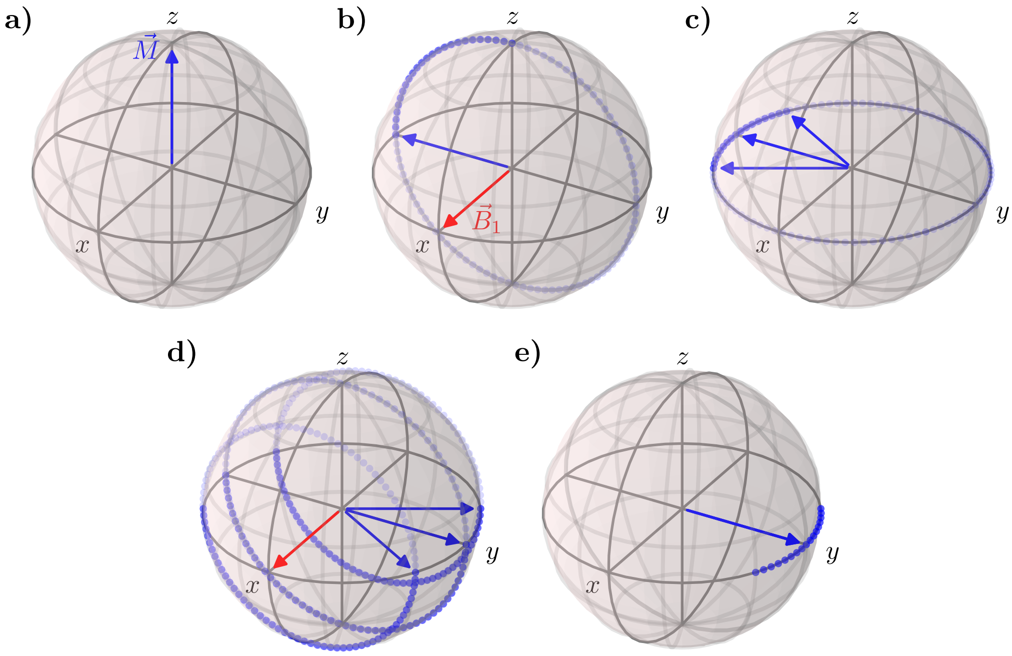

Figure 5.2.4: Bloch spheres in the rotating reference frame illustrating the effect of the Hahn-echo pulse sequence on the total magnetization $\vec{M}$. The different spheres always show the final state. Opaque blue points show the trace of $\vec{M}$ and transparent points indicate the extrapolated trace. **a)** Initially, $\vec{M}$ is assumed to be aligned with the magnetic background field $\vec{B}_0 = B_0\vec{e}_z$. **b)** A $\pi/2$-pulse applied via the resonator magnetic field $\vec{B}_1 = B_1\vec{e}_x$ rotates $\vec{M}$ onto the xy-plane. **c)** Due to inhomogeneities of $\vec{B}_0$ and spin-spin interactions, $\vec{M}$ fans out with time and the different parts precess around the z-axis. **d)** After a free evolution time τ following the $\pi/2$-pulse, a π-pulse effectively inverts the y-components of the fanned out $\vec{M}$. **e)** Finally, the different magnetic moments refocus after a total time of 2τ since the $\pi/2$-pulse and the change of the total magnetization induces a signal into the inductor of the resonator, which is eventually recorded.

saturation value being the same as the one for a set gain of 20 dB. These results and the one obtained from characterizing the amplifier placed at the Q-port are also listed in table 5.2.1.

Note on pESR with Reflection Type Resonators Unfortunately, we experienced several soft- and hardware problems with the ADC unit after the successful pESR measurements using the transmission chip. These technical difficulties could not be resolved in the course of this work, which is the reason why we can only discuss measurements in transmission geometry. However, the measurement procedure is identical for the usage of reflection type resonators.

5.2.2 Hahn-Echo Measurement

Hahn-Echo Pulse Sequence The Hahn-echo pulse sequence is widely used for characterizing spin ensembles, i.e. NV centers in diamond, and for quantum memory applications [10, 11, 101]. In this work, it is a two pulse sequence consisting of a $\pi/2$-pulse followed by a

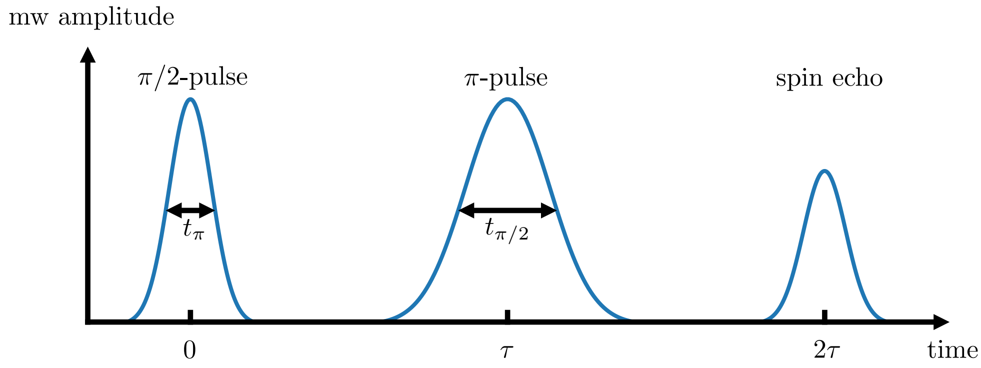

Figure 5.2.5: Hahn-echo pulse sequence illustrated in terms of microwave signal amplitude. The pulses are of gaussian shape. After a time of 2τ since the initial pulse, one records a spin echo of lower amplitude due to spin-spin dephasing effects.

π-pulse later. To illustrate the effects of this pulse sequence on the total magnetization $\vec{M}$, we represent the occurring vectors in Bloch spheres. Such a sphere was originally introduced to display the states of a two level system, e.g. qubits [102]. The different steps of the Hahn-echo pulse sequence are shown in the Bloch spheres in Figure 5.2.4. Note that the representation is already in the rotating reference frame.

We assume $\vec{M}$ to point in z-direction initially. Then, the $\pi/2$-pulse is applied through the magnetic field of the resonator $\vec{B}_1$. It rotates the total magnetization $\vec{M}$ onto the equatorial plane. Subsequently, $\vec{M}$ starts to fan out as indicated by the additional blue vectors in Figure 5.2.4 c). This is caused by magnetic inhomogeneities of $\vec{B}_0$ and spin-spin interactions. Consequently, there is not a single sharp Larmor frequency but instead a band of frequencies due to the different local magnetic environments of each spin. Each of these spins then starts to precess around the z-axis with its own detuning frequency $\Delta\omega(\vec{r}) = \omega_0 - \omega_{\mathrm{L}}(\vec{r})$.

After some free evolution time τ, a π-pulse is applied. This pulse effectively inverts the y-component of each spin. As a consequence, the spins refocus and after an additional free evolution time τ, $\vec{M}$ is refocused. This represents a change in magnetic flux, which induces the signal of this spin echo into the resonator and is eventually recorded.

In Figure 5.2.5, the Hahn-echo sequence is depicted in terms of sent and measured microwave amplitudes. The amplitude and pulse area of the spin echo becomes naturally lower with increasing free evolution time τ. This is due to spin-spin relaxation, which causes the spins to dephase in a way that cannot be compensated by the π-pulse [59, 62]. This relaxation mechanism is characterized by the spin-spin relaxation time T_2, also called the dephasing time.

Single Echo Measurement For the measurements presented from hereon, we set the amplitude of the AWG to $0.7\,\mathrm{V}$, the RF power of the vector source to $5\,\mathrm{dBm}$, the RF power of the external LO source to $18\,\mathrm{dBm}$ and the temperature of the cryostat to $T = 3\,\mathrm{K}$. All measurements were executed at the low field ESR transition of $^{\mathrm{nat}}$Si:P placed on the transmission NbTiN chip. With these settings, we employ a standard Hahn-echo pulse sequence. We choose the duration of the $\pi/2$-pulse and π-pulse to be $t_{\pi/2} = 150\,\mathrm{ns}$ and $t_\pi = 300\,\mathrm{ns}$, respectively. For

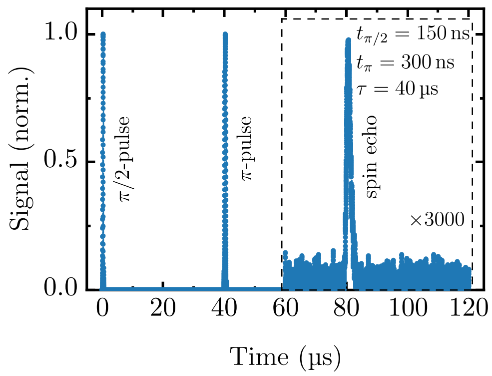

Figure 5.2.6: Hahn-echo measurement using a single excitation $\pi/2$-pulse and a refocusing π-pulse conducted at $T = 3\,\mathrm{K}$. The signals are normalized to the maximum amplitude of the pulses. The duration of the pulses were $150\,\mathrm{ns}$ and $300\,\mathrm{ns}$. After twice the free evolution time $\tau = 80\,\mu\mathrm{s}$, the expected spin echo is recorded. The normalized amplitude of the measured signal is scaled up by a factor of 3000 for better visibility.

the free evolution time between the two pulses, we chose a duration of $\tau = 40\,\mu\mathrm{s}$, so we expect to measure a spin echo at time $2\tau = 80\,\mu\mathrm{s}$. To better distinguish the spin echo from noise, we record not just one but 10240 spin echos and averaged the acquired data. The shot repetition time between subsequent pulse sequences was chosen to be SRT $= 0.2\,\mathrm{s}$. We also record the pulses themselves in an extra measurement where we detuned the pulse frequency from the resonance frequency to allow for the transmission of the pulses and eventually the detection.

Both sent signals and measured data are shown together in Figure 5.2.6. The data has been normalized to the maximum amplitude of the pulses. We indeed measure a spin echo after $80\,\mu\mathrm{s}$ since the initial exciting $\pi/2$-pulse. However, the normalized amplitude is very low compared to the one of the pulses. We hereby have demonstrated, that we can use our hybrid system consisting of resonator and solid-state spin ensemble to store and retrieve microwave pulses in the fashion of a quantum memory.

Multimode Storage We just showed that we can store and retrieve a single $\pi/2$-pulse signal in our $^{\mathrm{nat}}$Si:P sample. However, for quantum memory applications, the storage of multiple information is crucial [11]. This can be realized by modifying the standard Hahn-echo pulse sequence. To store and retrieve for example two pulses in the same spin ensemble, we apply the pulse sequence shown in 5.2.7. Here, we send two subsequent $\pi/2$-pulses as signals to the spin ensemble. To be able to distinguish these signals apart from the point in time at which they were sent, we choose different amplitudes for them. After some time, a π-pulse is applied like in the standard Hahn-echo pulse sequence to refocus the precessing spins. Finally, two spin echoes are measured. The emitted signals from the spin ensemble appear in inverted order. The reason for this is the fact, that the signals are always located symmetrical in time around the π-pulse, since it acts similar to a time inversion on the precessing spins.

We conduct a measurement using this pulse sequence, where we send the second $\pi/2$-pulse $5\,\mu\mathrm{s}$ after the first one. The added duration both pulses results in the one of the $\pi/2$-pulse

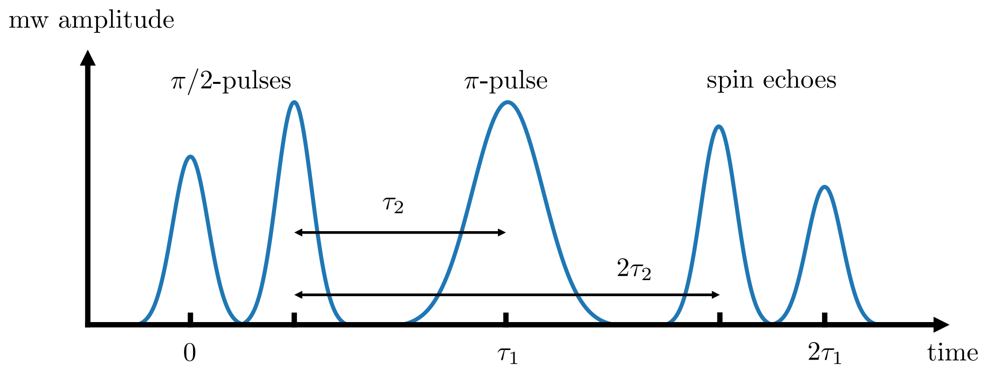

Figure 5.2.7: Modified Hahn-echo pulse sequence for storing and retrieving two signals. The signals consist of two subsequent $\pi/2$-pulses of different amplitudes to distinguish the spin echoes later. A π-pulse is used to refocus the precessing spins. Finally after a time of $2\tau_1$ and $2\tau_2$ since the exciting $\pi/2$-pulses, the corresponding spin echoes are measured in inverted order.

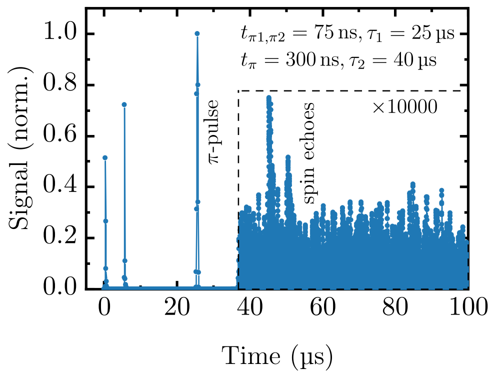

Figure 5.2.8: Measurement of multimode storage at $T = 3\,\mathrm{K}$. Two $\pi/2$-pulses of different amplitudes are stored to and retrieved from the ^{nat}Si:P sample. The spin echoes are measured in inverted order of the initial two pulses as indicated by the different amplitudes.

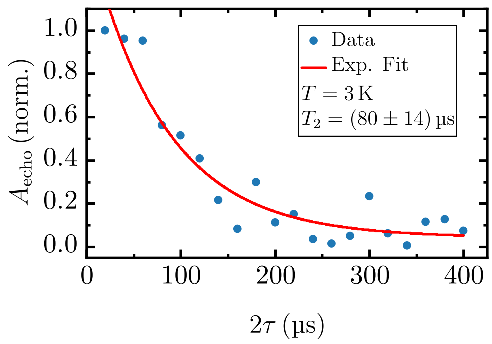

Figure 5.2.9: Measurement of the spin-spin relaxation time T_2 for $^{\mathrm{nat}}$Si:P measured at $T = 3\,\mathrm{K}$. The normalized area of the spin echoes are shown as a function of the time of measurement 2τ. The data is fit with an exponential decay given by equation (5.16).

used in the previous measurement. After $\tau_1 = \tau_2 + 5\,\mu\mathrm{s} = 25\,\mu\mathrm{s}$, the refocusing π-pulse is applied. Consequently, we expect the echoes to be measured at around $2\tau_1 = 50\,\mu\mathrm{s}$ and $2\tau_2 + 5\,\mu\mathrm{s} = 45\,\mu\mathrm{s}$. Figure 5.2.8 shows both the sent pulses as well as the recorded data. The measurement data is also averaged over 10240 records with a larger SRT of $1\,\mathrm{s}$ to ensure that all spins have relaxed back into the initial state. We indeed notice two spin echoes at $45\,\mu\mathrm{s}$ and $50\,\mu\mathrm{s}$ with different amplitudes. We can assign the first echo to the second $\pi/2$-pulse and the second echo to the first pulse, as expected.

To retrieve the stored pulses in the correct order, one could in principle apply the method proposed in [11]. Here, one would add an additional π-pulse after the echoes occur. The second pulse would effectively cancel the inversion of the spin ensemble, meaning that the order of the stored signals is restored. However, when doing this one would need to avoid recording the first echoes, also called "silencing". This can be done by decoupling the resonator from the spin ensemble for the period of time at which the first series of echoes would be measured.

5.2.3 Measurement of Spin Coherence Time

We also employed the Hahn-Echo pulse sequence to measure the spin-spin relaxation time T_2, which is also referred to as spin coherence or dephasing time. Due to this relaxation mechanism, the intensity of the spin echo decreases exponentially in time [103]. This is here measured by applying the standard Hahn-Echo pulse sequence and vary the free induction time τ between the two pulses from $10\,\mu\mathrm{s}$ to $200\,\mu\mathrm{s}$. The obtained data for each element of this series is averaged over 10240 records with a SRT of $0.2\,\mathrm{s}$. Instead of taking the amplitude of the spin echo as a measure for its intensity, we use the area of the gaussian like signal.

The measured intensity of each echo is normalized to the echo signature recorded at $2\tau = 20\,\mu\mathrm{s}$. The data is shown in Figure 5.2.9. We can see the expected exponential decay in the echo intensity. To extract the T_2 relaxation time, we fit the measured data with the exponential function:

$$A_{\mathrm{echo}} = A \cdot \exp\left(\frac{-2\tau}{T_2}\right) + A_0, \tag{5.16}$$

where A is the amplitude and A_0 denotes an offset. From the fit, we obtain $T_2 = (80 \pm 14)\,\mu\text{s}$, which is in the correct order of magnitude for comparable samples [12].

The spin coherence time can be increased in three ways. First, using isotopically purified ^{28}Si samples with phosphorous donors instead of $^{\text{nat}}$Si:P increases T_2 significantly [12]. The reason for this increase is the reduction of the isotope ^{29}Si, which has a natural abundance of 4.7% in natural silicon. ^{29}Si exhibits a magnetic moment and therefore contributes to the dephasing dipole fluctuations affecting the spins of phosphorous. Another way to increase T_2 is by reducing the concentration of phosphorous dopants in silicon [5]. A lower density of addressable spins consequently leads to lower spin-spin interactions among them, thereby reducing the dephasing effects. Finally, reducing the temperature also increases the spin coherence time, although saturation has been observed at temperatures few Kelvin [5, 104].

5.3 Summary

Finally, we want to summarize the main results of this chapter. We first presented cwESR measurements using a NbTiN transmission type resonator chip at liquid helium temperatures and a Nb reflection type chip at millikelvin temperatures on $^{\text{nat}}$Si:P samples with a concentration of $[\text{P}] = 2 \times 10^{17}\,\text{cm}^{-3}$. We stressed the importance of ensuring good contact between sample and resonator as a prerequisite for cwESR measurements. By using DPPH as a spin marker, we calibrated the magnetic field of the liquid helium temperature setup. We then discussed the method of cwESR using the two materials, resonator geometries and temperature regimes stated above. From these measurements, we could extract the working points for pESR experiments and the collective coupling rate g_{eff} between resonator and spin ensemble. Furthermore, we were able to assign the hybrid system measured at elevated temperature to the weak coupling regime with a cooperativity $C \approx 0.1$ and the one measured at millikelvin temperature to the strong coupling regime with $C \approx 2$. We identified the thermal spin polarization $P(T)$ as the main reason for that [57]. We also investigated the influence of the applied incident microwave power on g_{eff}. Here, we saw the effect of saturation setting in. The main difference between the two setups was identified to lay in the different spin-lattice relaxation times T_1 [59], which is larger at lower temperatures and favors saturation at lower incident microwave powers. The same quantity was estimated by using the method of saturation recovery [97], where we obtained an estimation value of $T_1 \approx 33\,\text{s}$.

We then presented pESR as the second measurement technique at liquid helium temperatures using the NbTiN transmission chip. First, we discused the measurement setup and its calibration. Following that, we explained the Hahn-Echo pulse sequence [10]. We then demonstrated the storage and retrieval of a single pulse. Additionally, we explored the crucial characteristic of multimode storage, which is of importance for quantum memory applications [11]. Here, we stored two pulses and retrieved them in inverted order in form of two spin echoes. Finally, we used the Hahn-Echo pulse sequence to measure the spin-spin relaxation time T_2 of the spin system. We obtained $T_2 = (80 \pm 14)\,\mu\text{s}$, which is in good agreement for comparable samples [12].

Differences of the two Resonator Geometries in Signal to Noise Ratio Finally, we want to address the difference of both resonator geometries in terms of signal to noise ratio. As suggested from the theory presented in Chapter 2.1.2, reflection type resonators promise to exhibit a signal to noise ratio greater by a factor of two compared to transmission geometry due to every signal coupling back from the resonator being measured [8]. In general, we would have liked to measure this difference and thereby investigate the postulated factor of two. Unfortunately, doing so turned out to be non-trivial and quite challenging. The main idea is to fabricate two chips with identical resonators that only differ in feedline geometry and compare the measured cwESR spectra and amplitudes of the pESR spin echoes. However, there are two reasons that make the realization of this strategy complicated.

On the one hand, it proved to be very difficult to actually fabricate resonators with identical properties but different feedline geometries. We discussed this at the example of the chips "JF001" and "JF002" in Chapter 4.3.1. These two chips were fabricated as parallel as possible but still differed in terms of resonance frequencies and quality factors. Especially matching the external coupling rate κ_{ext} of both geometries would require multiple attempts and therefore would be very time consuming.

On the other hand, the identical sample preparation is very sensitive. Assuming we have successfully fabricated two chips with identical resonator properties but different feedline geometries, we also need to mount the same $^{\mathrm{nat}}$Si:P sample on the resonators. As shown in [9], the filling factor ν that is connected to the effective collective coupling rate via $g_{\mathrm{eff}} \propto \sqrt{\nu}$ is extremely sensitive to the vertical spacing between resonator and spin ensemble sample. It is therefore evident, that mounting the same sample twice with the same vertical spacing is highly challenging.

Chapter 6

Nuclear Magnetic Resonance

In this chapter, we first discuss the concept of nuclear magnetic resonance (NMR), its differences to ESR and the combination of both techniques applied on phosphorous donors in silicon. In the second part, we introduce different possibilities to realize the experimental implementation of NMR on our resonator-spin-ensemble system.

6.1 Basics of NMR and Combination with ESR

Basics of NMR Nuclear magnetic resonance was first measured by Purcell et al. and Bloch et al. in 1946 [105, 106]. It is mostly applied in chemistry to detect changes in the chemical environment of nuclei and is also used for e.g. structure determination in the field of organic chemistry [107, 108].

In order to measure NMR, the nucleus of interest must exhibit a non-vanishing nuclear spin I resulting in a nuclear magnetic moment μ_n. Therefore, only nuclei with an odd mass number A can be probed with NMR [19]. Such nuclei are for example ^{29}Si and ^{31}P with a nuclear spin of $I = \frac{1}{2}$. The latter is the nucleus of our interest.

In an external magnetic field $\vec{B}_0 = B_0\vec{e}_z$, the nuclear spin $\vec{I}$ of phosphorous is affected by the nuclear Zeeman effect, which is exactly analogue to the Zeeman effect acting on the unbound electron system of Si:P with spin $\vec{S}$. The energy splitting of the ^{31}P spin states caused by just this interaction between nuclear spins and external magnetic field is given by:

$$E_{m_I} = -\vec{\mu}_\mathrm{n} \cdot \vec{B}_0 = -g_\mathrm{n}\mu_\mathrm{N}B_0 m_I, \;\; m_I = \pm\frac{1}{2}. \tag{6.1}$$

Here, $g_\mathrm{n} = 2.2632$ is the nuclear Landé factor of phosphorous and μ_N is the nuclear magneton [38]. In contrast to the electron spin, the $m_I = +\frac{1}{2}$ state is energetically more favorable for the nuclear spin.

The energy difference between those two levels, that is simultaneously the resonance condition for NMR, is given by [19]:

$$\hbar\omega_\mathrm{L,N} = g_\mathrm{n}\mu_\mathrm{N}B_0, \tag{6.2}$$

where ω_L is the Larmor frequency for the nuclear spins. The frequencies required to drive NMR transitions at a given magnetic field B_0 are way lower than the one of ESR due to the nuclear magneton μ_N being three orders of magnitude smaller than the Bohr magneton μ_B.

Concerning the nuclear spin dynamics of ^{31}P, the situation is identical to the one of electron

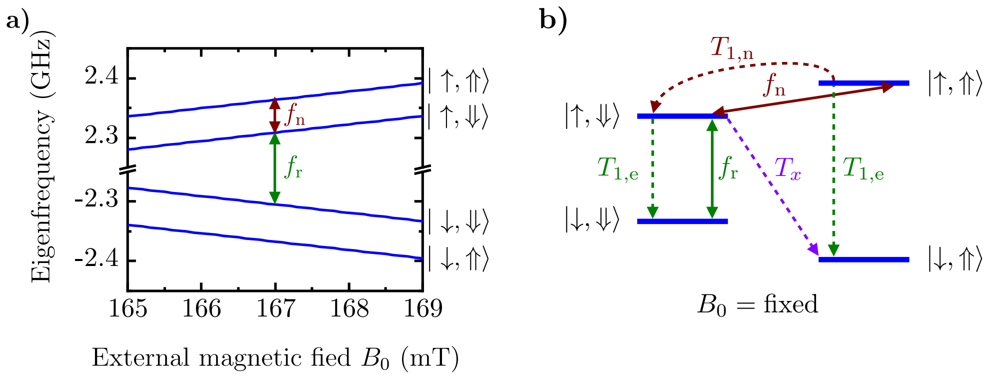

Figure 6.1.1: Exemplary demonstration of the combination of ESR and NMR transitions of Si:P. **a)** Breit-Rabi diagram showing the Si:P spin state energies as a function of the external magnetic field. First, the ESR transition from the $|\downarrow,\Downarrow\rangle$ to the $|\uparrow,\Downarrow\rangle$ state is driven with the microwave resonance frequency f_r. Second, a radio frequency pulse excites the nuclear spins from the $|\uparrow,\Downarrow\rangle$ to the $|\uparrow,\Uparrow\rangle$ state. **b)** Schematic of the spin states, ESR and NMR transitions in a given magnetic field B_0. The dashed lines indicate the spin-lattice relaxations T_1 trying to reestablish the equilibrium state. The spin-exchanging relaxation process with the characteristic time T_x is caused by the Overhauser-effect [109].

spins discussed in Chapter 5.2.2, but with the relation

$$\vec{M} = +\gamma_\mathrm{N}\vec{L}, \tag{6.3}$$

where γ_N is the nuclear gyromagnetic ratio. Due to the positive nuclear Landé factor g_n of ^{31}P, the sense of precession is contrary to the one of the electron spins [60, 62]:

$$\frac{d\vec{M}}{dt} = +\gamma_\mathrm{n}(\vec{M} \times \vec{B}_0). \tag{6.4}$$

Combination with ESR We now discuss how we can conceptually combine our existing measurement technique as discussed in the previous chapters with the NMR technique for possible quantum memory applications. Given our hybrid system of a resonator coupled to a Si:P solid-state spin ensemble, the magnetic fields as well as the ESR transition frequencies are already determined by the fixed resonance frequency of the resonator. In general, it is clear that the pulse protocol must consist of two subsequent excitations. As a consequence, we can only address the high field ESR transition, as shown in figure 6.1.1.

In principle, we have the choice of either driving the ESR transition first followed by the NMR one or vice versa. We choose the former option based on two favorable properties: On the one hand, the quantum memory should be easily integrable in quantum information circuitry. Fortunately, the frequencies of ESR transitions are in the microwave regime and therefore ideally suited. On the other hand, the second transition represents the actual storage unit. The spin coherence time of the nuclear spins $T_{2,\mathrm{n}}$ is larger than the one of the electron spins $T_{2,\mathrm{e}}$. Hence, one naturally exploits this property of the nuclear spin system and chooses the latter as the actual

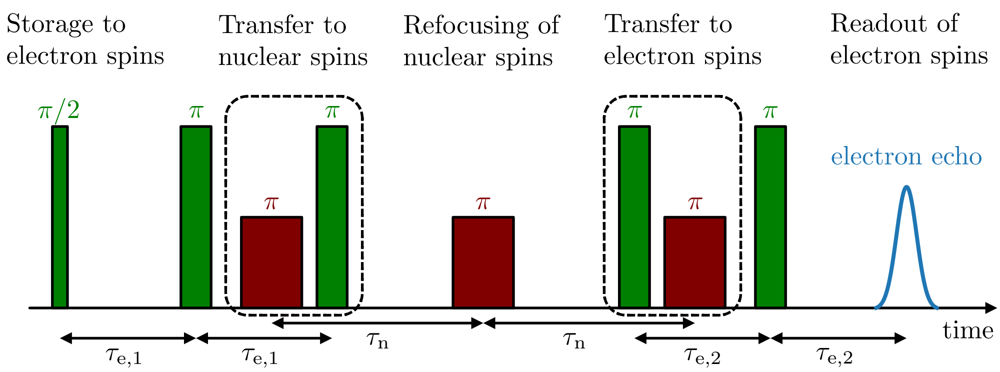

Figure 6.1.2: Pulse-sequence for demonstration of the storage of a coherent microwave state in a nuclear spin state via an intermediate electron spin state and retrieval [13]. The pulse sequence is $\pi/2$-π-π(RF)-π-π(RF)-π-π(RF)-π-readout. The three NMR π-pulses represent a Hahn-echo-like sequence used for actual storage of the information transferred via the electron spin system in the nuclear spin system. Figure adapted from [13].

storage unit for increased storage times of up to a few minutes [110].

The different spin states of Si:P together with the mentioned transitions and spin-lattice relaxation times are shown in figure 6.1.1 b). The spin-lattice relaxation times of the electron $T_{1,\mathrm{e}}$ and nuclear spins $T_{1,\mathrm{n}}$ strive to reestablish the equilibrium state. However, since these times are significantly larger than their dephasing times, the limiting factor for the storage time is given by the latter ones [13]. However, since $T_{1,\mathrm{e}} < T_{1,\mathrm{n}}$, the electron spin-lattice relaxation can also provide an upper limit for the storage time. Additionally to the mentioned relaxation processes, there is another one where the electron and nuclear spin relax by exchanging spin orientation. This is the so-called Overhauser-effect and its characteristic time T_x is in the order of hours, thereby negligible [98, 109].

A possible quantum memory pulse protocol has been demonstrated by Morton et al. on Si:P and is shown in figure 6.1.2 [13]. The pulse sequence effectively consists of three interwoven Hahn-echo sequences and is used to coherently store and retrieve quantum information.

A coherent microwave state is first transferred to an electron spin state by an initial $\pi/2$-pulse with given phase ϕ. This phase represents the information that is to store and retrieve. The coherence of the electron spin state is refocused by applying a π-pulse. Following that, the spin state is transferred and stored to the nuclear spin by subsequent nuclear and electron π-pulses of which the latter is applied at the time of the electron spin echo. After half of the storage time, a refocusing π-pulse is applied to the nuclear spin state. The transfer back to the electron spin-state is done with the inverse pulse sequence. Finally, a π-pulse is applied to refocus the back-transferred spin state and the following electron spin echo is measured. The latter exhibits the same phase ϕ of the initial $\pi/2$-pulse and therefore proves the coherent storage of information.

Morton et al. reported a nuclear spin coherence time of $T_{2,\mathrm{n}} = 1.75\,\mathrm{s}$ at $T = 5.5\,\mathrm{K}$ using repetitive dynamic decoupling sequences during the storage time $2\tau_{\mathrm{n}}$ [13]. This value is significantly higher than our measured electron spin coherence time $T_{2,\mathrm{e}} \approx 80\,\mu\mathrm{s}$, supporting the choice of the nuclear spins as the storage unit. Similar memory pulse sequences using different measurement and readout techniques have been demonstrated by [111, 112].

6.2 Possible Realizations of NMR

We now discuss how to experimentally realize the addition of NMR to our existing hybrid system of a planar superconducting microwave resonator coupled to the Si:P spin ensemble. As already mentioned in the previous chapter, the ESR resonance frequencies are in the microwave regime of a few gigahertz whereas NMR transition frequencies are in the range of tens of megahertz. In general, there exist tunable microwave resonators, whose frequency can be adjusted by applying magnetic flux or a dc bias [88, 113]. However, the shift of the resonance frequency is insufficient to drive both ESR and NMR transitions with the same tunable microwave resonator. Hence, NMR transitions must be driven with the magnetic field $\vec{B}_2$ provided by an additional device. In the following, we present possible candidates for this purpose.

Planar Conducting Loop In theory, the most convenient and simplest implementation consists of an on-chip solution. We therefore explore the properties and influence of a superconducting loop enclosing the resonator by simulations using CST Microwave Studio. The modelled chip is shown in figure 6.2.1 a). The loop is designed as an CPW identical to the feedline with the dimensions $w = 20\,\mu\mathrm{m}$ and $s = 12\,\mu\mathrm{m}$. It replaces the separating stripe and passes between feedline and resonator.

In order to simulate its magnetic field B_2 at the spot of the spin ensemble, it is driven with a NMR typical frequency of $60\,\mathrm{MHz}$. The resulting magnetic field distribution on a plane that cuts the feedline and the inductor of the resonator perpendicularly is shown in figure 6.2.1 b). We note the overall amplitude of the magnetic field B_2 being two orders of magnitude lower than the magnetic field B_1 of the resonator shown in figure 3.1.5. A strong field B_2 is crucial for the duration of NMR pulses, since the rotational Larmor frequency is given by:

$$\omega_{\mathrm{L,N}} = \frac{\mu_{\mathrm{N}}}{\hbar} B_2. \tag{6.5}$$

We once again stress that μ_{N} is three orders of magnitude smaller than μ_{B} for ESR. Assuming the addressed spins to be located about $20\,\mu\mathrm{m}$ above the substrate, the simulated field amplitude is about $0.1\,\mathrm{mT}$. Consequently, we estimate the duration of a π-pulse to be $t_{\pi,\mathrm{N}} \approx 650\,\mu\mathrm{s}$. This is large compared to our measured electron spin coherence time of $T_2 \approx 80\,\mu\mathrm{s}$. Hence, the electron spins would have already dephased in the memory sequence discussed in the previous chapter due to the free evolution time of the electron spins needing to fulfill $\tau_{\mathrm{e},1} > t_{\pi,\mathrm{N}}$.

We also simulate the S_{21}-parameter of the bare resonator chip and the one with the conducting loop enclosing the resonator to examine the influence of the loop on the coupling between resonator and feedline. The data is shown in figure 6.2.1 c). We observe that instead of a single resonance, four high amplitude resonance-like signatures are present in the simulated data with the conducting loop around the resonator. A possible reason for this is the fact that signal coming from the resonator can also couple into the conducting loop instead of the feedline. This makes the whole situation effectively a four-port problem instead of a two-port as for just

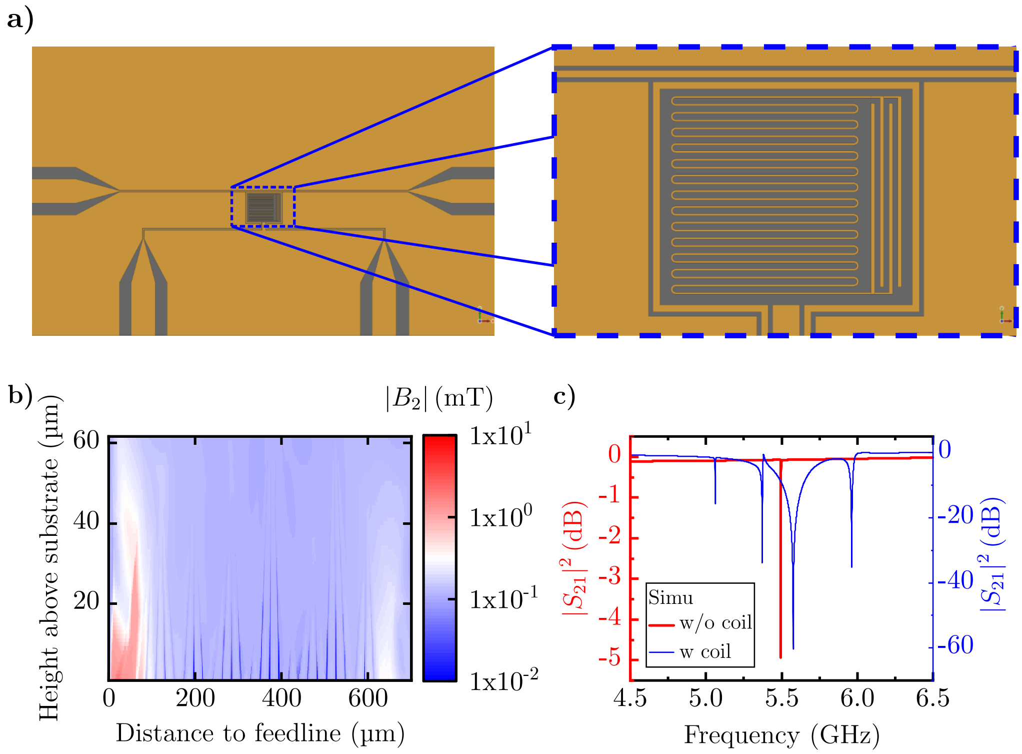

Figure 6.2.1: Design and simulation results for realizing NMR by placing a conducting loop around the resonator. **a)** A CPW with the same dimensions as the feedline encloses the resonator and is driven at megahertz frequencies. **b)** Simulated $|B_2|$ field caused by the conducting loop on a plane that cuts perpendicularly through the feedline and the inductor of the resonator. The driving frequency is set to 60 MHz. **c)** Simulated $|S_{21}|^2$ data of the resonator without and with the conducting loop enclosing it. The presence of the loop leads to four resonance-like and deeper signatures in the data.

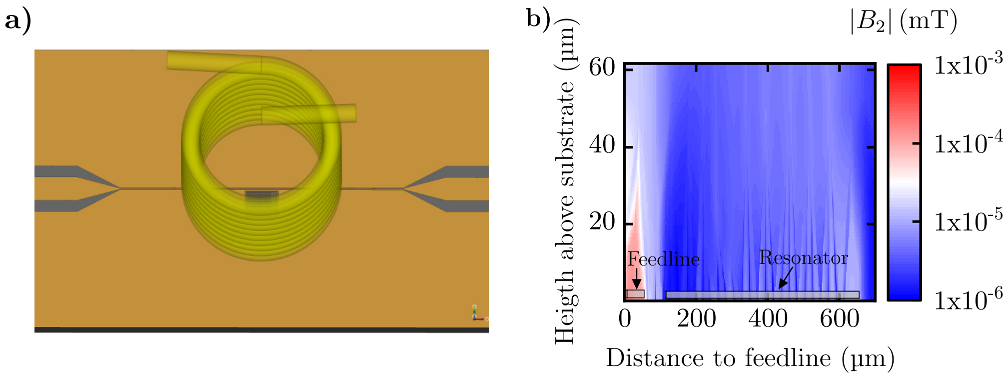

Figure 6.2.2: Simulation of an air coil placed on top of the resonator chip. **a)** CST model of an air coil made of copper (depicted in yellow) on to of the resonator chip for NMR. **b)** Simulated B_2 distribution of the air coil for a typical NMR driving frequency an an applied Power of $0.5\,\mathrm{W}$. The amplitude of the magnetic field is very low.

a transmission type feedline.

While this NMR implementation seems to be a convenient solution at first glance, it unfortunately yields a too small magnetic field B_2 and potentially also leads to signal losses. It is therefore not suited for our system.

Coil Placed on top of Resonator Another possibility to generate the B_2 field at the spot of the sample for NMR is by using a small cylindrical air coil made of copper. The idea is to place it on top of the Si:P sample located on the resonator as shown in the CST model in figure 6.2.2 a). The modelled coil has 10 windings, a coil diameter of $3\,\mathrm{mm}$, a wire diameter of $400\,\mathrm{\mu m}$ and a height of about $5\,\mathrm{mm}$, which are dimensions comparable to commercially available air coils.

The simulated B_2 field distribution is shown in figure 6.2.2. We notice an even lower field amplitude compared to the conducting loop discussed previously. There are two possible reasons for that.

On the one hand, the relative placement of coil and resonator is not optimal. Ideally, one would like to place the resonator together with the spin ensemble inside of the coil where the magnetic field of the latter is the strongest and most homogeneous. Obviously, this is not feasible due to the geometric dimensions of both resonator chip and coil. Consequently, the spin ensemble is exposed to the stray magnetic field just outside of the coil, where it naturally fans out and exhibits a weaker amplitude [114].

On the other hand, there might be more suited simulation software for this kind of problem. In CST Microwave Studio, we cannot set the current of the driving field and the applied power is always fixed to $0.5\,\mathrm{W}$. One would potentially like to explore the results from other simulation software, where one varies the applied current to enhance the field amplitude before ruling out this option. However, one also needs to keep in mind that these resistive coils heat up at high enough currents, which might make their employment in cryostats not reasonable.

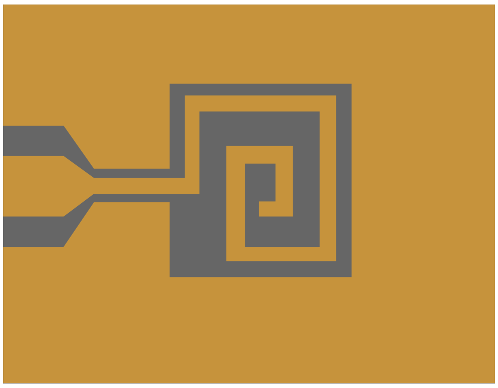

Figure 6.2.3: Sketch of a the top chip hosting a planar spiral coil for NMR in flip-chip geometry.

Planar Coil on a second Chip in Flip-Chip Geometry Finally, we want to conceptually sketch a more complex experimental realization of NMR on our hybrid system. Since NMR can be measured by using planar superconducting RF coils [115, 116], we propose to also employ such. Obviously, we need the magnetic field B_2 to overlap with the sample that is already placed on top of the planar superconducting microwave resonator, so a placement of the coil next to the latter is unreasonable. Instead, the coil should be fabricated on a second chip that is placed in a flip-chip geometry above the resonator chip, thereby clamping the spin ensemble between the two chips.

The field magnitude of the planar coil could be resonantly enhanced, by designing it as a spiral resonator coupled to a feedline as in [9]. Obviously, the resonance frequency must be drastically reduced for NMR purposes, but since this type behaves like a $\lambda/2$-resonator, one can easily do this by extending the length of the resonant strip. The reason why one would choose this design instead of other sub-gigahertz lumped-element resonators as in [117], is the magnetic field distribution. The spiral resonator exhibits a higher field homogeneity and also decays on a larger scale than the resonator design that we use for ESR. Due to this characteristic, the magnetic field could be sufficiently large at the spot of the sample for NMR.

However, since the transition frequencies of Si:P at a given magnetic field B_0 are well defined, the choice of a setup consisting of two resonators is unreasonable since one simply cannot precisely fabricate matching resonance frequencies. Hence, one cannot employ a spiral resonator and needs to use a simple planar coil as sketched in Figure 6.2.3, which can be driven with any frequency and therefore can be manually matched to the NMR frequency by the driving source [118].

Chapter 7

Summary and Outlook

In this thesis, we have studied superconducting lumped element microwave resonators for electron spin resonance spectroscopy. In addition, these resonators can reach the so-called strong coupling regime, where the subsystems microwave resonator and the spin resonance transition hybridize, which is of interest for quantum state storage. This motivated us to discuss the physics of the coupled systems using the input-output formalism, which allows to describe the hybridization of the microwave photonic and the spin excitation mode [20].

Notably, we discuss this formalism for hanger type resonators, where the lumped element microwave resonator is coupled to a microwave transmission line and reflection type resonators, which results in some subtle differences regarding the spectra. The reflection type resonators should principally improve the signal recovered from the spin system, as all of the signal is used for analysis and hence improve the the signal-to-noise ratio [8]. We then discussed the spin Hamiltonian of phosphorous donors in silicon and how we can drive ESR transitions with a single microwave resonator at two well-defined magnetic fields B_0. Key for the understanding of the coupling of microwave mode and spin ensemble is the Tavis-Cummings Hamiltonian. We reviewed the underlying concepts and derived the scattering parameters that characterize the hybrid system in terms of coupling rates.

Essential for the realization of the hybrid system is the understanding of the microwave resonator. In Chapter 3, we gave insight on how we model and simulate our resonators using finite element modeling tools, in particular CST Microwave Studio [22]. The resonator model, simulation settings and discrepancies between simulation and reality were addressed, pointing out the main reason for differences to be the modelling of the superconducting layer by perfectly electric conducting material. We also detailed the fabrication procedure based on e-beam lithography and reactive ion etching for microwave resonators made of either NbTiN or Nb.

In Chapter 4, we systematically studied the performance of the superconducting materials NbTiN and Nb. Here, DC transport measurements were employed to determine the critical temperatures of $T_{\mathrm{c,NbTiN}} \approx 16\,\mathrm{K}$ and $T_{\mathrm{c,Nb}} \approx 7.9\,\mathrm{K}$. While the value obtained for NbTiN is in good agreement with literature values, the one of Nb is about $1\,\mathrm{K}$ lower than expected [83, 84]. The smaller width of transition $\Delta T_{\mathrm{Nb}} = 0.0107\,\mathrm{K}$ of Nb compared to NbTiN with $\Delta T_{\mathrm{NbTiN}} = 0.0718\,\mathrm{K}$ hinted a higher quality of Nb thin films. Unfortunately, the NbTiN thin films decreased in quality over the course of this work due to degradation of the sputter deposition target.

We then compared lumped-element resonators based on the design of [9] coupled to feedlines in transmission and reflection geometry. The reflection type feedline is terminated in open circuit geometry and leads to a position dependent external coupling rate κ_{ext} due to the forming of standing waves. The external quality factors Q_{ext} of these resonators ranged from 6000 to 80000 at a temperature of $4\,\mathrm{K}$. Subsequently, we investigated the behavior of the resonators under conditions relevant for electron spin resonance spectroscopy. In particular, we investigated the robustness of the resonators against external magnetic fields, temperature, and their behavior as function of the incident microwave power. All performance limiting mechanisms can be either related to the kinetic inductivity of the materials or the two-level systems present in the structures. The NbTiN resonators proved to be more robust towards external magnetic fields than Nb as expected [18]. The internal quality factor of Nb drastically decreases from 270000 at zero magnetic field to 50000 at $200\,\mathrm{mT}$ measured at millikelvin temperatures. From measurements conducted at various temperatures in the Kelvin regime, we observed high stability of NbTiN at elevated temperatures due to its high critical temperature of $16\,\mathrm{K}$. For variations of the temperature in the millikelvin regime, the influence of highly detuned TLS on the resonance frequency and the internal quality factor were observed. The contribution of these TLS to the Q_{int} were determined to be $Q_{\text{TLS}} = 2.9 \times 10^6$ for a NbTiN resonator [54]. We also investigated the behavior of the microwave resonators for different incident microwave powers. For powers above $-20\,\mathrm{dBm}$ at liquid helium temperatures, the lineshape of the resonance becomes asymmetrical and shows the characteristic of a duffing oscillator [90]. At millikelvin temperatures and low powers down to the single photon regime, we observed the influence of unsaturated TLS on Q_{int} of the resonators. Here we yielded the TLS quality factors to be $Q_{\text{TLS,NbTiN}} = 285 \times 10^3$ and $Q_{\text{TLS,Nb}} = 1471 \times 10^3$ for the employed materials NbTiN and Nb.

In order to adjust the external and internal coupling rate of the resonators, we varied different geometric parameters in the design. We noted that by increasing the width of the separating stripe w_{sep} between resonator and signal line leads to a decrease of κ_{ext}. In contrast to that, the measurement of resonators width different widths of the inductor w_{ind} unfortunately did not yield a reliable results on how this parameter affects κ_{int}.

In Chapter five, we employed our resonators in ESR experiments on phosphorous donors in natural silicon with a donor concentration of $[\mathrm{P}] = 2 \times 10^{17}\,\mathrm{cm}^{-3}$. We discussed cwESR experiments using a NbTiN resonator coupled to a tansmission type feedline at liquid helium temperatures and also using a Nb resonator coupled to a reflection type feedline at millikelvin temperatures. The former configuration showed a cooperativity of $C \approx 0.1$ in the weak coupling regime and the latter configuration exhibited a cooperativity of $C \approx 2$ and thus, strong coupling between resonator and spin ensemble. We identified the thermal spin polarization $P(T)$ as the main reason for this difference in C. Furthermore, we investigated the saturation of the spin ensemble by varying the incident microwave power at the sample. The setup at millikelvin temperatures saturated at lower powers due to the larger spin-lattice relaxation time T_1 [59]. By using the method of saturation recovery, we were able to estimate $T_1 \approx 33\,\mathrm{s}$ at millikelvin temperatures [97]. In the second part of this chapter, pulsed ESR experiments on the same Si:P sample using the NbTiN resonator coupled to a transmission type feedline measured at liquid helium temperatures were discussed. We measured spin echoes using the Hahn-echo pulse sequence and also demonstrated the storage and retrieval of multiple pulses in the spin ensemble [10]. For the spin coherence time of Si:P, we obtained $T_2 \approx 80\,\mu\mathrm{s}$, which agrees with comparable samples [12].

In the final chapter, we conceptually discussed electron nuclear magnetic resonance concepts for transferring the excitation in the spin system to the nuclear subsystem and back. This would allow to store information in the nuclear spin ensemble with larger spin coherence times of

$T_{2,\mathrm{n}} = 1.75\,\mathrm{s}$ at $T = 5.5\,\mathrm{K}$, which is of high interest for potential quantum memory applications [13]. We then analyzed different possibilities to realize the addition of NMR experimentally to our existing hybrid system. Here, a flip-chip geometry with a planar coil on the top chip seemed promising in theory, as its magnetic field B_2 should be sufficiently large at the spot of the sample to efficiently drive NMR transitions.

Finally, we want to provide an outlook on how one can continue on from the results of this work. Since we encountered a decreasing in quality of the NbTiN thin films, one should strive to optimize the thin films after and reestablish the original quality that has been achieved in Ref. [18]. Resonators made of NbTiN thin films with high enough quality should outperform Nb ones in terms of Q_{int} in external magnetic fields relevant for electron spin resonance at millikelvin temperatures.

In this work, we only discussed pulsed electron spin resonance measurements at elevated temperatures using resonators coupled to a transmission type feedline. One still has to also do these measurements using the new chip design of resonators coupled to a reflection type resonators at liquid helium and millikelvin temperatures. An obvious next step is to move to isotopically engineered ^{28}Si:P to yield higher spin coherence times [12]. Since our maximal spin cooperativity $C \approx 2$ is neither in the critical nor deep in the strong coupling regime, one wants to achieve $C = 1$ and $C \gg 1$ to compare the efficiency of storage and readout processes between resonator and spin ensemble for quantum memory applications.

Lastly, the ideas to experimentally implement NMR on our hybrid system needs to be further developed. As already mentioned in the last chapter, the option of generating the driving magnetic field B_2 by using a small air coil needs to be further investigated before ruling it out completely. More appropriate simulation software should be employed to simulate the magnetic field distribution of such a coil. Otherwise, one can proceed by modelling and simulating the planar coil in flip-chip geometry and thereby test its applicability for NMR applications.

Besides the optimization of a ^{28}Si:P based quantum memory, we want to also look one step further. Until now, we have only demonstrated the storage and retrieval of classical microwave pulses in our spin ensemble. However, for quantum computing based on transmons and fluxonium qubits, quantum memories are also required. The idea of a random access quantum memory has been already demostrated for a spin ensemble [15]. The next step would be to demonstrate the actual transfer of information between transmon and quantum memory. Our approach towards a quantum memory uses NbTiN resonators coupled to a spin ensemble in an external magnetic field. In contrast to that, transmon qubits and their readout resonators are mostly made of Nb. Therefore the coherence time of the transmon qubit as well as the quality factor of the resonator suffer from significant losses in an external magnetic field that is necessary for the functionality of the quantum memory [119]. To avoid these qubit losses while simultaneously utilizing the magnetic field robustness of NbTiN resonators for the quantum memory, a setup of two chips might be reasonable. Here, one Nb chip would host the qubit and its readout resonator and the other NbTiN chip would host the quantum memory. These chips would then need to be electrically connected while magnetically shielding the qubit chip.

In conclusion, we further developed the resonator design to enhance the readout signal, which is another important aspect towards storage and retrieval of quantum states in a spin-based quantum memory.

Appendix A

Fabrication Recipe

The fabrication steps inside the clean room, which are described in chapter 3.2, are presented here in a step-by-step manner. The chips are handled with a pair of tweezers with teflon tips to prevent causing scratches in the surface. Every step is executed on clean room wipes to minimize contamination and the chips are transported in concave plastic sample boxes with the surface facing down.

Cleaning the Chip for HF Treatment

1. Loose the silicon chip of your choice from the pre-cut wafer by pushing the backside of the foil on which it is sticking with your finger until you can grab the chip with the tweezers. Carefully remove the chip.

2. Prepare a hotplate by setting the temperature to 120 °C.

3. Fill a beaker with technical grade acetone and put the chip in it. Place the beaker in the ultrasonic bath for 2 minutes at medium power level.

4. Repeat step 3 twice with p.a. grade acetone.

5. Repeat step 3 once with p.a. grade isopropanol.

6. Remove the chip from the beaker filled with isopropanol and rinse it with p.a. grade isopropanol.

7. Place the chip on the clean room wipe while still holding it with the tweezers and carefully blow dry the surface of the chip with nitrogen gas.

8. Put the chip on the preheated hotplate for approximately 2 minutes.

9. Check the surface of the chip with a microscope for scratches, residues of protective coating etc. If necessary, clean the chip again by starting from step 4. If there are too many scratches, discard the chip.

10. Proceed with HF treatment.

Cleaning the Chip for Spin Coating

1. Prepare a hotplate by setting the temperature to $70\,^{\circ}\mathrm{C}$.
2. Prepare two beakers of p.a. acetone and p.a. isopropanol each and place one beaker of each chemical on the hotplate. Wait for the chemicals to heat up.
3. Put the chip in the beaker with room temperature acetone and place it into the ultrasonic bath at medium power level for 5 minutes.
4. Repeat the previous step with the other three beakers in the following order: hot acetone, hot isopropanol and room temperature isopropanol.
5. Remove the chip from the beaker filled with isopropanol and rinse it with p.a. grade isopropanol.
6. Place the chip on the clean room wipe while still holding it with the tweezers and carefully blow dry the surface of the chip with nitrogen gas.
7. Proceed with spin coating.

Spin Coating

1. Prepare the hotplate for bakeout by setting up a program that applies a temperature of $150\,^{\circ}\mathrm{C}$ for 1 minute with the vacuum function active. Start the program and the hotplate starts heating until it reaches the set temperature.
2. Activate the vacuum function of the spin coater and open its lid. Carefully mount the chip onto the spin coater. The vacuum pump sucks the chip onto the O-ring. Center the chip with help of the aligner shape or carefully with the tweezers. In case of the latter, it is recommended to execute a lever movement with the tweezers to be able to push the chip with high precision.
3. Close the lid after successful alignment.
4. Get a suitable tip for the pipette. Its volume should be suitable for $40\,\mu\mathrm{L}$ of resist. Blow the tip at each opening with nitrogen gas. Mount the tip to the pipette.
5. Extract $40\,\mu\mathrm{L}$ of CSAR "AR-P 6200.18" resist. Be careful to not dip the tip too deep into the resist. Otherwise, thin film of resist accumulates on the outside of the tip will drop.
6. Insert the pipette into the spin coater via the opening on the top of the lid. It is recommended to use both hands for stabilization and steadiness of the movement. There is an edge on which you can rest the pipette. This serves as a first orientation point. Carefully approach the surface of the chip until the distance between chip and tip is about $0.5\,\mathrm{cm}$ to $1\,\mathrm{cm}$.
7. When in position, press the button of the pipette down in a slow and steady motion and keep holding it down.

8. If there happens to form a bubble of air, you can either try to carefully pop it with the tip or try to extract it with the pipette, where you still hold the button down. In case of the latter option, aim for the bubble and carefully lower the pressure on the button until the bubble is sucked into the tip. There will also be some resist sucked into the tip, but do not try to put it back to the chip.

9. Remove the pipette and discard the tip into the trash bin.

10. Start the spin coater program that runs with $8000\,\mathrm{rpm}$ for 1 minute.

11. Open the lid, deactivate the vacuum function and carefully remove the chip from the spin coater.

12. Check whether the film of resist is distributed homogeneously except for some wall of resist in two of the four edges. If that is not the case and/or there are scratches in the resist layer due to mishandling the chip with the tweezers, you need to remove the resist layer according to the instruction "Removal of Resist" and start over at "Cleaning the Chip for Spin Coating".

13. Place the chip onto the wafer of the hotplate and place the wafer on the hotplate. Close the lid and start the program.

14. Open the lid and remove the wafer and subsequently the chip. Place the chip with the surface facing up on the tray of the sample box.

15. Get a watch glass, a tooth pick, the bottle of liquid containing gold nanoparticles and a pipette made of glass. Shake the bottle a few times. Extract some fluid from the bottle with the glass pipette and place one to two droplets onto the watch glass. The remaining liquid in the pipette can be put back into the bottle.

16. Dip the tooth pick in the droplet of gold nanoparticles and carefully place a small droplet in a corner of the surface of the chip by gently pressing the tooth pick onto the surface. Hold the toothpick vertical for this step. Note on NbTiN chips: Try to place the droplet on the NbTiN thin film and not on the silicon boundary around it.

17. Repeat the previous step for the other three corners.

18. Proceed with e-beam lithography.

Developing Exposed Resist

1. Prepare the hotplate for post-exposure bakeout by setting up a program that applies a temperature of $130\,^{\circ}\mathrm{C}$ for 1 minute with the vacuum function active. Start the program and the hotplate starts heating until it reaches the set temperature.

2. Prepare three beakers: One with the developer chemical "AR 600-546" and two with p.a. grade isopropanol.

3. Hold the chip with tweezers and gently move it in the developer chemical for 2 minutes. Make sure to not hit the beaker wall. It is recommended to move the chip in the shape of the number 8.
4. Dip the chip for about 10 seconds in the first beaker filled with p.a. grade isopropanol and move it just like in the previous step.
5. Place the chip in the second beaker filled with p.a. grade isopropanol. Place the beaker in the ultrasonic bath at low power level for 2 minutes.
6. Remove the chip from the beaker and rinse it with p.a. grade isopropanol.
7. Place the chip on the clean room wipe while still holding the former with the tweezers and carefully blow dry the surface of the chip with nitrogen gas.
8. Check the surface of the chip with a microscope for flakes or residues of resist. If necessary start over from step 2 but reduce the time of development (e.g. only 30 seconds).
9. Place the chip onto the wafer and place it wafer on the hotplate. Close the lid and start the program.
10. Open the lid and remove the chip.
11. Proceed with reactive ion etching.

Removal of Resist

1. Prepare three beakers: One with the remover chemical "AR 600-71" and two with p.a. grade isopropanol.
2. Place the chip in the beaker with remover chemical for about 10 minutes. Move the chip at times with the tweezers.
3. Dip the chip for about 10 seconds in p.a. grade isopropanol and move it just like in the previous step.
4. Place the chip in the other beaker filled with p.a. grade isopropanol. Place the beaker in the ultrasonic bath at low power level for 2 minutes.
5. Remove the chip from the beaker filled with isopropanol and rinse it above the latter with p.a. grade isopropanol.
6. Place the chip on the clean room wipe while still holding the former with the tweezers and carefully blow dry the surface of the chip with nitrogen gas.
7. Check the surface of the chip with a microscope for flakes or residues of resist. If necessary, start over at step 2. Optional: Heat the remover up to $40\,^{\circ}\mathrm{C}$ by placing the beaker on a hotplate.
8. The chip is finished.

Appendix B

Further Transport Measurements

As mentioned in chapter 4.2, we conduct additional transport measurements on NbTiN thin films after exchanging the target of the ULTRADISK. The films are grown on silicon substrates with a thermal oxide layer on top, i.e. these chips are not treated with HF. The process parameters as well as the results of the transport measurements are listed in table B.0.1 and the data is shown in the following.

Sample	T_{depo} (°C)	Ar/N_2	I_{depo} (mA)	RRR	Method	T_c (K)	ΔT (K)
NbTiN06	20	36.2/3.8	200	0.9021	fit	10.159	0.313
					mean value	10.306	0.263
NbTiN07	500	36.2/3.8	200	1.0640	fit	15.739	0.201
					mean value	15.912	0.260
NbTiN08	500	37/3	200	1.1876	fit	15.215	0.061
					mean value	15.219	0.043
NbTiN09	500	35/5	200	1.0897	fit	15.974	0.054
					mean value	16.010	0.043
NbTiN10	500	35/5	400	1.1024	fit	14.611	0.040
					mean value	14.615	0.044
NbTiN11	500	34/6	400	/	fit	15.705	0.030
					mean value	15.714	0.035

Table B.0.1: Summary of the deposition parameters and determined characteristics for sputtered NbTiN thin films. The deposition procedure is explained in chapter 3.2. The performed transport measurements and the according data analysis is addressed in chapter 4.2.

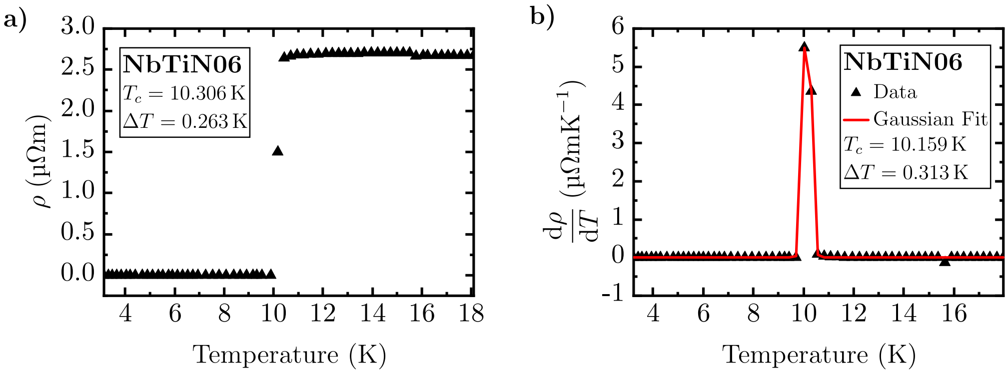

Figure B.0.1: T_c measurement of sample NbTiN06. **a)** Raw data. **b)** Numerical derivative with gaussian fit. The critical temperature is far below the expected value of 16 K, hinting that this film does not have the desired composition. This film has insufficient quality.

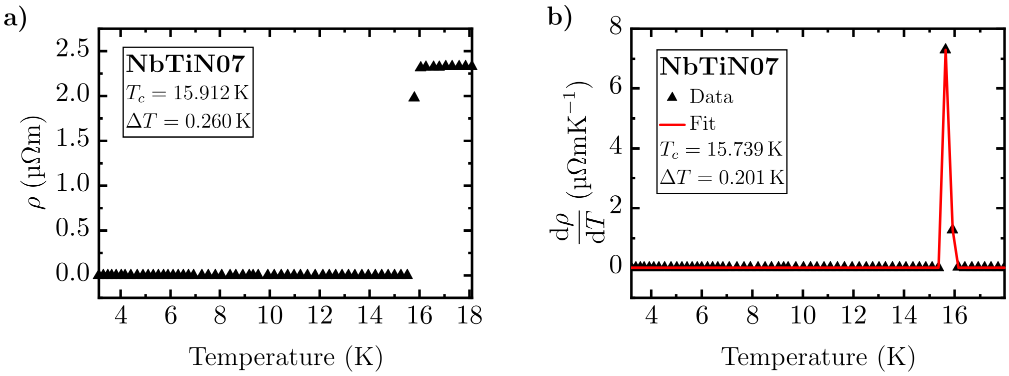

Figure B.0.2: T_c measurement of sample NbTiN07. **a)** Raw data. **b)** Numerical derivative with gaussian fit. The transition temperature seems very good, but the transition width is rather large compared to other films. Based on this large width, this film seems not be of sufficient quality.

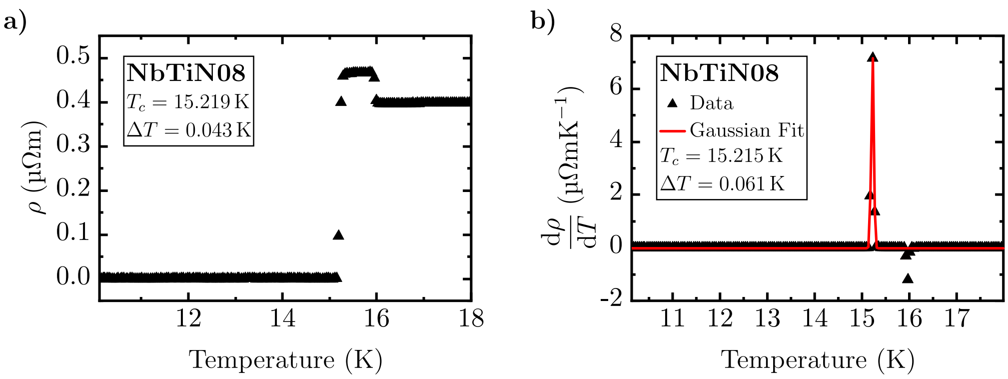

Figure B.0.3: T_c measurement of sample NbTiN08. **a)** Raw data. **b)** Numerical derivative with gaussian fit. The critical temperature is good and the width of the transition is very small. However, the drop in ρ after passing T_c is irritating.

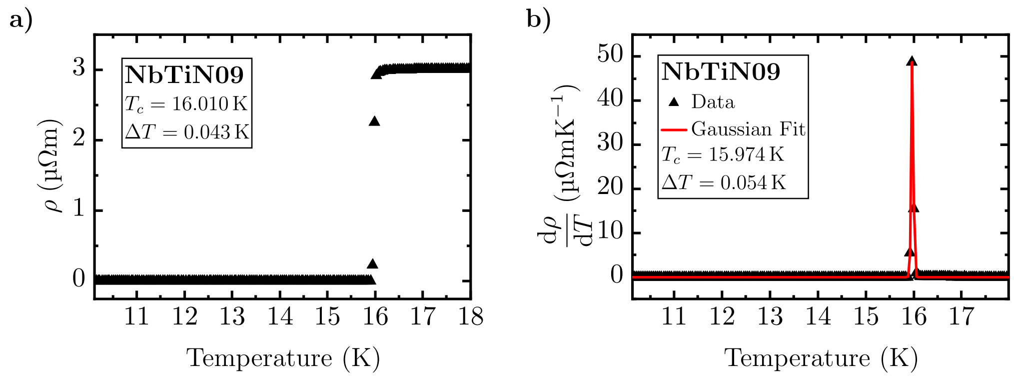

Figure B.0.4: T_c measurement of sample NbTiN09. **a)** Raw data. **b)** Numerical derivative with gaussian fit. Both critical temperature and the transition width show promising values of high quality films.

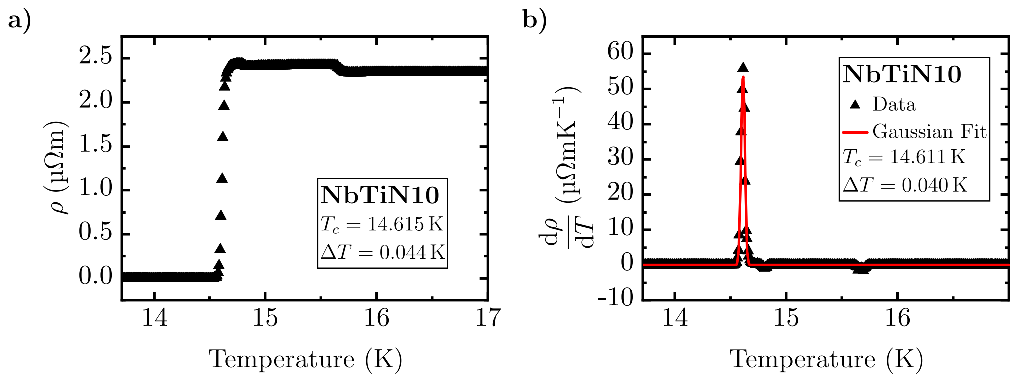

Figure B.0.5: T_c measurement of sample NbTiN10. **a)** Raw data. **b)** Numerical derivative with gaussian fit. The transition is very sharp, but the critical temperature is rather low, which is not satisfactory.

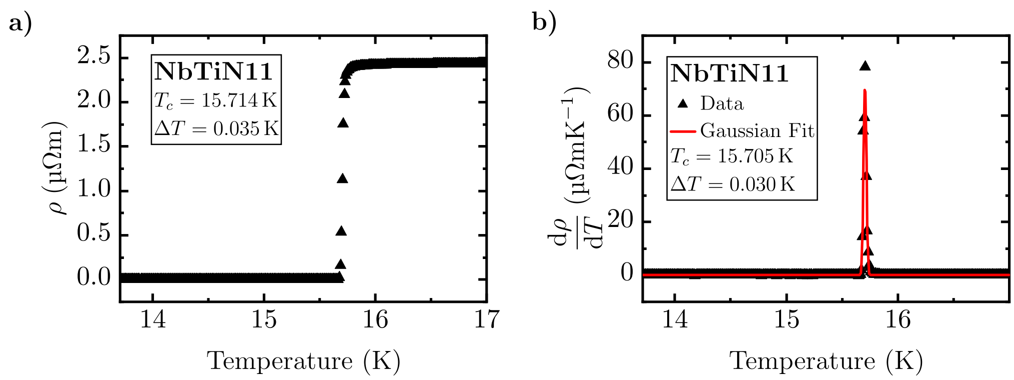

Figure B.0.6: T_c measurement of sample NbTiN11. **a)** Raw data. **b)** Numerical derivative with gaussian fit. The values for T_c and ΔT also look very promising and hint for a high quality thin film.

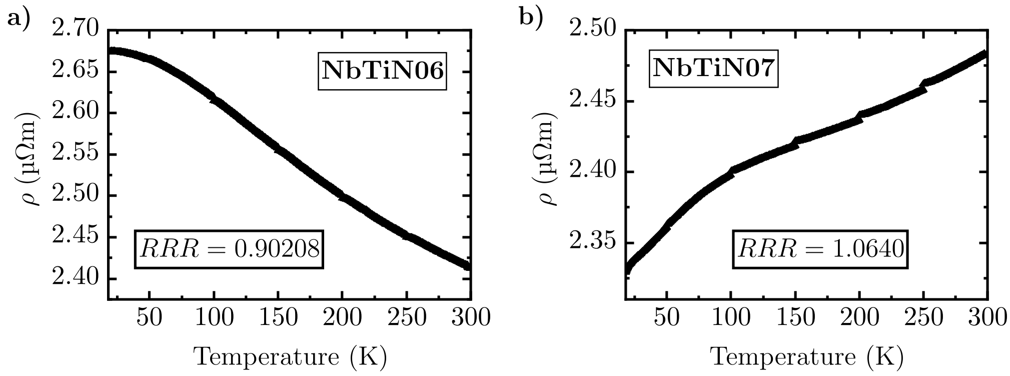

Figure B.0.7: Measured $\rho(T)$ curves of samples **a)** NbTiN06 and **b)** NbTiN07. The decline of ρ for NbTiN06 hints that this film does not fulfill the required composition of the three components.

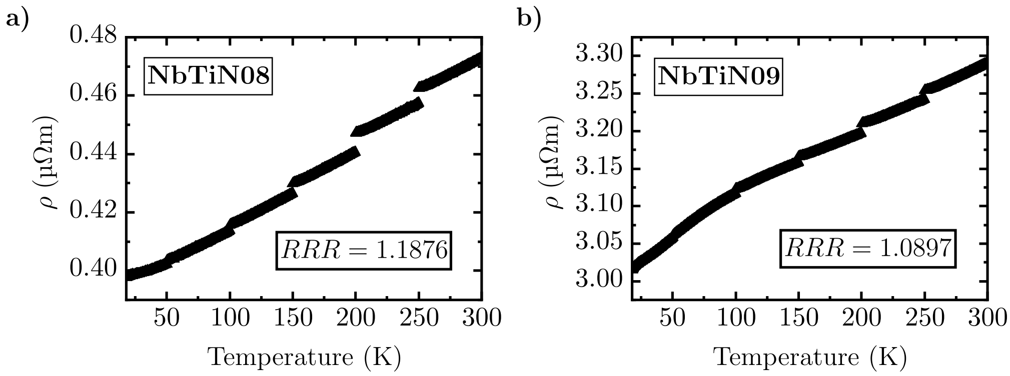

Figure B.0.8: Measured $\rho(T)$ curves of samples **a)** NbTiN08 and **b)** NbTiN09. The jumps in the data are a consequence of the measurement procedure, which was done in intervals of $50\,\mathrm{K}$.

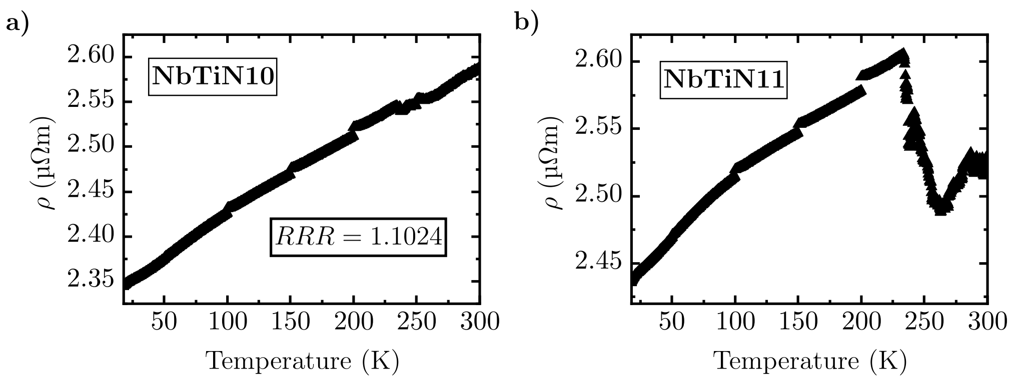

Figure B.0.9: Measured $\rho(T)$ curves of samples **a)** NbTiN10 and **b)** NbTiN11. For the latter, no RRR value was extracted due to the unusual behavior of ρ for temperatures above $225\,\mathrm{K}$.

Bibliography

[1] H. J. KIMBLE, *The Quantum Internet*, Nature **453**, 1023 (2008).

[2] S. FILIPP, in *Chancen und Risiken von Quantentechnologien: Praxis der zweiten Quantenrevolution für Entscheider in Wirtschaft und Politik*, edited by A. Wilms and F. Neukart (Springer Fachmedien, Wiesbaden, 2022) pp. 21–30.

[3] M. A. NIELSEN, *Quantum Computation by Measurement and Quantum Memory*, Physics Letters A **308**, 96 (2003).

[4] A. MORELLO, J. J. PLA, P. BERTET, AND D. N. JAMIESON, *Donor Spins in Silicon for Quantum Technologies*, Advanced Quantum Technologies **3**, 2000005 (2020).

[5] A. M. TYRYSHKIN, S. TOJO, J. J. L. MORTON, H. RIEMANN, N. V. ABROSIMOV, P. BECKER, H.-J. POHL, T. SCHENKEL, M. L. W. THEWALT, K. M. ITOH, AND S. A. LYON, *Electron Spin Coherence Exceeding Seconds in High-Purity Silicon*, Nature Materials **11**, 143 (2012).

[6] K. SAEEDI, S. SIMMONS, J. Z. SALVAIL, P. DLUHY, H. RIEMANN, N. V. ABROSIMOV, P. BECKER, H.-J. POHL, J. J. L. MORTON, AND M. L. W. THEWALT, *Room-Temperature Quantum Bit Storage Exceeding 39 Minutes Using Ionized Donors in Silicon-28*, Science **342**, 830 (2013).

[7] S. WEICHSELBAUMER, M. ZENS, C. W. ZOLLITSCH, M. S. BRANDT, S. ROTTER, R. GROSS, AND H. HUEBL, *Echo Trains in Pulsed Electron Spin Resonance of a Strongly Coupled Spin Ensemble*, Physical Review Letters **125**, 137701 (2020).

[8] H. WANG, S. SINGH, C. R. H. MCRAE, J. C. BARDIN, S.-X. LIN, N. MESSAOUDI, A. R. CASTELLI, Y. J. ROSEN, E. T. HOLLAND, D. P. PAPPAS, AND J. Y. MUTUS, *Cryogenic Single-Port Calibration for Superconducting Microwave Resonator Measurements*, Quantum Science and Technology **6**, 035015 (2021).

[9] S. WEICHSELBAUMER, P. NATZKIN, C. W. ZOLLITSCH, M. WEILER, R. GROSS, AND H. HUEBL, *Quantitative Modeling of Superconducting Planar Resonators for Electron Spin Resonance*, Physical Review Applied **12**, 024021 (2019).

[10] E. L. HAHN, *Spin Echoes*, Physical Review **80**, 580 (1950).

[11] C. GREZES, Y. KUBO, B. JULSGAARD, T. UMEDA, J. ISOYA, H. SUMIYA, H. ABE, S. ONODA, T. OHSHIMA, K. NAKAMURA, I. DINIZ, A. AUFFEVES, V. JACQUES, J.-F. ROCH, D. VION, D. ESTEVE, K. MOELMER, AND P. BERTET, *Towards a Spin-Ensemble Quantum Memory for Superconducting Qubits*, Comptes Rendus Physique Quantum Microwaves / Micro-ondes Quantiques, **17**, 693 (2016).

[12] E. Abe, A. M. Tyryshkin, S. Tojo, J. J. L. Morton, W. M. Witzel, A. Fujimoto, J. W. Ager, E. E. Haller, J. Isoya, S. A. Lyon, M. L. W. Thewalt, and K. M. Itoh, *Electron Spin Coherence of Phosphorus Donors in Silicon: Effect of Environmental Nuclei*, Physical Review B **82**, 121201 (2010).

[13] J. J. L. Morton, A. M. Tyryshkin, R. M. Brown, S. Shankar, B. W. Lovett, A. Ardavan, T. Schenkel, E. E. Haller, J. W. Ager, and S. A. Lyon, *Solid-State Quantum Memory Using the 31P Nuclear Spin*, Nature **455**, 1085 (2008).

[14] M. Pompili, S. L. N. Hermans, S. Baier, H. K. C. Beukers, P. C. Humphreys, R. N. Schouten, R. F. L. Vermeulen, M. J. Tiggelman, L. dos Santos Martins, B. Dirkse, S. Wehner, and R. Hanson, *Realization of a Multinode Quantum Network of Remote Solid-State Qubits*, Science **372**, 259 (2021).

[15] J. O'Sullivan, O. W. Kennedy, K. Debnath, J. Alexander, C. W. Zollitsch, M. Šimėnas, A. Hashim, C. N. Thomas, S. Withington, I. Siddiqi, K. Mølmer, and J. J. L. Morton, *Random-Access Quantum Memory Using Chirped Pulse Phase Encoding*, Physical Review X **12**, 041014 (2022).

[16] A. Bienfait, P. Campagne-Ibarcq, A. H. Kiilerich, X. Zhou, S. Probst, J. J. Pla, T. Schenkel, D. Vion, D. Esteve, J. J. L. Morton, K. Moelmer, and P. Bertet, *Magnetic Resonance with Squeezed Microwaves*, Physical Review X **7**, 041011 (2017).

[17] J. J. L. Morton and P. Bertet, *Storing Quantum Information in Spins and High-Sensitivity ESR*, Journal of Magnetic Resonance **287**, 128 (2018).

[18] M. Müller, T. Luschmann, A. Faltermeier, S. Weichselbaumer, L. Koch, G. B. P. Huber, H. W. Schumacher, N. Ubbelohde, D. Reifert, T. Scheller, F. Deppe, A. Marx, S. Filipp, M. Althammer, R. Gross, and H. Huebl, *Magnetic Field Robust High Quality Factor NbTiN Superconducting Microwave Resonators*, Materials for Quantum Technology **2**, 015002 (2022).

[19] J. A. Pople, *High-Resolution Nuclear Magnetic Resonance* (McGraw-Hill, New York, 1959).

[20] D. Walls and G. J. Milburn, in *Quantum Optics*, edited by D. Walls and G. J. Milburn (Springer, Berlin, Heidelberg, 2008) pp. 127–141.

[21] M. Tavis and F. W. Cummings, *Exact Solution for an N -Molecule—Radiation-Field Hamiltonian*, Physical Review **170**, 379 (1968).

[22] *CST Studio Suite 3D EM Simulation and Analysis Software* (2023), available online at https://www.3ds.com/products-services/simulia/products/cst-studio-suite/, last accessed: 03/06/2023.

[23] L. J. van der Pauw, *A Method of Measuring the Resistivity and Hall Coefficient on Lamellae and Arbitrary Shape*, Philips Technical Review **20**, 220 (1958).

[24] F. J. Rosenbaum, *Dielectric Cavity Resonator for ESR Experiments*, Review of Scientific Instruments **35**, 1550 (1964).

[25] D. M. Pozar, *Microwave Engineering*, 3rd ed. (Wiley, Hoboken, NJ, 2005).

[26] E. R. Eisenach, J. F. Barry, M. F. O'Keeffe, J. M. Schloss, M. H. Steinecker, D. R. Englund, and D. A. Braje, *Cavity-Enhanced Microwave Readout of a Solid-State Spin Sensor*, Nature Communications **12**, 1357 (2021).

[27] R. Narkowicz, D. Suter, and I. Niemeyer, *Scaling of Sensitivity and Efficiency in Planar Microresonators for Electron Spin Resonance*, Review of Scientific Instruments **79**, 084702 (2008).

[28] P. Russer, *Electromagnetics, Microwave Circuit and Antenna Design for Communications Engineering*, 2nd ed., Artech House Antennas and Propagation Library (Artech House, Boston, Mass., 2006).

[29] M. Göppl, A. Fragner, M. Baur, R. Bianchetti, S. Filipp, J. M. Fink, P. J. Leek, G. Puebla, L. Steffen, and A. Wallraff, *Coplanar Waveguide Resonators for Circuit Quantum Electrodynamics*, Journal of Applied Physics **104**, 113904 (2008).

[30] P. Natzkin, *Superconducting Microwave Resonator Designs for Electron Spin Resonance Applications*, Master's thesis, Technische Universität München, Garching (2017).

[31] M. Greifenstein, *Elektronenspinresonanz mit supraleitenden Mikrowellenresonatoren bei Millikelvin-Temperaturen*, Master's thesis, Technische Universität München, Garching (2012).

[32] C. W. Gardiner and M. J. Collett, *Input and Output in Damped Quantum Systems: Quantum Stochastic Differential Equations and the Master Equation*, Physical Review A **31**, 3761 (1985).

[33] A. Bohm, in *Quantum Mechanics: Foundations and Applications*, Texts and Monographs in Physics, edited by A. Bohm (Springer, Berlin, Heidelberg, 1986) pp. 310–327.

[34] S. Probst, F. B. Song, P. A. Bushev, A. V. Ustinov, and M. Weides, *Efficient and Robust Analysis of Complex Scattering Data under Noise in Microwave Resonators*, Review of Scientific Instruments **86**, 024706 (2015).

[35] M. S. Khalil, M. J. A. Stoutimore, F. C. Wellstood, and K. D. Osborn, *An Analysis Method for Asymmetric Resonator Transmission Applied to Superconducting Devices*, Journal of Applied Physics **111**, 054510 (2012).

[36] G. Feher, *Electron Spin Resonance Experiments on Donors in Silicon. I. Electronic Structure of Donors by the Electron Nuclear Double Resonance Technique*, Physical Review **114**, 1219 (1959).

[37] H. MORISHITA, L. S. VLASENKO, H. TANAKA, K. SEMBA, K. SAWANO, Y. SHIRAKI, M. ETO, AND K. M. ITOH, *Electrical Detection and Magnetic-Field Control of Spin States in Phosphorus-Doped Silicon*, Physical Review B **80**, 205206 (2009).

[38] N. J. STONE, *Table of Nuclear Magnetic Dipole and Electric Quadrupole Moments*, Atomic Data and Nuclear Data Tables **90**, 75 (2005).

[39] J. A. WEIL, *Electron Paramagnetic Resonance*, A Wiley-Interscience Publication (Wiley, New York u.a., 1994).

[40] E. JAYNES AND F. CUMMINGS, *Comparison of Quantum and Semiclassical Radiation Theories with Application to the Beam Maser*, Proceedings of the IEEE **51**, 89 (1963).

[41] R. BENNETT, T. M. BARLOW, AND A. BEIGE, *A Physically Motivated Quantization of the Electromagnetic Field*, European Journal of Physics **37**, 014001 (2015).

[42] G. S. AGARWAL, *Rotating-Wave Approximation and Spontaneous Emission*, Physical Review A **4**, 1778 (1971).

[43] P. L. KNIGHT AND L. ALLEN, *Rotating-Wave Approximation in Coherent Interactions*, Physical Review A **7**, 368 (1973).

[44] R. H. DICKE, *Coherence in Spontaneous Radiation Processes*, Physical Review **93**, 99 (1954).

[45] T. HOLSTEIN AND H. PRIMAKOFF, *Field Dependence of the Intrinsic Domain Magnetization of a Ferromagnet*, Physical Review **58**, 1098 (1940).

[46] Y. Hirayama, K. Ishibashi, and K. Nemoto, eds., *Hybrid Quantum Systems*, Quantum Science and Technology (Springer Nature, Singapore, 2021).

[47] R. MESERVEY AND P. M. TEDROW, *Measurements of the Kinetic Inductance of Superconducting Linear Structures*, Journal of Applied Physics **40**, 2028 (1969).

[48] R. GROSS AND A. MARX, *Festkörperphysik* (De Gruyter, 2018).

[49] E. F. C. DRIESSEN, P. C. J. J. COUMOU, R. R. TROMP, P. J. DE VISSER, AND T. M. KLAPWIJK, *Strongly Disordered TiN and NbTiN S-Wave Superconductors Probed by Microwave Electrodynamics*, Physical Review Letters **109**, 107003 (2012), comment: 5+4 pages, 3 + 2 figures, arxiv:1205.2463 [cond-mat] .

[50] H. ALPERN, E. KATZIR, S. YOCHELIS, N. KATZ, Y. PALTIEL, AND O. MILLO, *Unconventional Superconductivity Induced in Nb Films by Adsorbed Chiral Molecules*, New Journal of Physics **18**, 113048 (2016), comment: 12 pages and 5 figures, arxiv:1612.02239 [cond-mat] .

[51] D. XU, S. K. YIP, AND J. A. SAULS, *Nonlinear Meissner Effect in Unconventional Superconductors*, Physical Review B **51**, 16233 (1995).

[52] J. LISENFELD, A. BILMES, A. MEGRANT, R. BARENDS, J. KELLY, P. KLIMOV, G. WEISS, J. M. MARTINIS, AND A. V. USTINOV, *Electric Field Spectroscopy of Material Defects in Transmon Qubits*, npj Quantum Information **5**, 1 (2019).

[53] C. MÜLLER, J. H. COLE, AND J. LISENFELD, *Towards Understanding Two-Level-Systems in Amorphous Solids: Insights from Quantum Circuits*, Reports on Progress in Physics **82**, 124501 (2019).

[54] D. P. PAPPAS, M. R. VISSERS, D. S. WISBEY, J. S. KLINE, AND J. GAO, *Two Level System Loss in Superconducting Microwave Resonators*, IEEE Transactions on Applied Superconductivity **21**, 871 (2011).

[55] C. R. H. MCRAE, R. E. LAKE, J. L. LONG, M. BAL, X. WU, B. JUGDERSUREN, T. H. METCALF, X. LIU, AND D. P. PAPPAS, *Dielectric Loss Extraction for Superconducting Microwave Resonators*, Applied Physics Letters **116**, 194003 (2020), arxiv:1909.07428 [physics, physics:quant-ph] .

[56] T. LUSCHMANN, A. JUNG, S. GEPRÄGS, F. X. HASLBECK, A. MARX, S. FILIPP, S. GRÖBLACHER, R. GROSS, AND H. HUEBL, *Surface Acoustic Wave Resonators on Thin Film Piezoelectric Substrates in the Quantum Regime*, Materials for Quantum Technology **3**, 021001 (2023).

[57] C. W. ZOLLITSCH, K. MUELLER, D. P. FRANKE, S. T. B. GOENNENWEIN, M. S. BRANDT, R. GROSS, AND H. HUEBL, *High Cooperativity Coupling between a Phosphorus Donor Spin Ensemble and a Superconducting Microwave Resonator*, Applied Physics Letters **107**, 142105 (2015).

[58] T. FLIESSBACH, *Statistische Physik: Lehrbuch zur Theoretischen Physik IV* (Springer, Berlin, Heidelberg, 2018).

[59] R. S. ALGER, *Electron Paramagnetic Resonance* (Interscience Publ., New York, 1968).

[60] F. BLOCH, *Nuclear Induction*, Physical Review **70**, 460 (1946).

[61] M. A. BERNSTEIN, *Handbook of MRI Pulse Sequences* (Academic Press, Amsterdam, 2004).

[62] C. KITTEL, *Einführung in Die Festkörperphysik*, 13th ed. (Oldenbourg, München [u.a.], 2002).

[63] R. N. SIMONS, *Coplanar Waveguide Circuits, Components, and Systems* (John Wiley & Sons, 2004).

[64] *CST Studio Suite Help* (2020), available online at https://space.mit.edu/RADIO/CST_online/cst_studio_suite_help.htm, last accessed: 03/02/2023.

[65] V. KRYMOV AND G. J. GERFEN, *Analysis of the Tuning and Operation of Reflection Resonator EPR Spectrometers*, Journal of Magnetic Resonance **162**, 466 (2003).

[66] W. DEMTRÖDER, *Experimentalphysik*, 9th ed., Springer-Lehrbuch (Springer, Berlin [u.a.], 2021).

[67] J. GAO, *The Physics of Superconducting Microwave Resonators*, Ph.D. thesis, California Institute of Technology (2008).

[68] J. BRAUMUELLER, J. BREHM, M. PFIRRMANN, S. PROBST, A. SCHNEIDER, Y. SCHÖN, A. STEHLI, M. WILDERMUTH, AND H. ROTZINGER, *Qkit*, Karlsruher Institut für Technologie (2023), available online at https://github.com/qkitgroup/qkit. last accessed: 04/01/2023.

[69] *Application Notes for Photolitografy with Technical Informations for Photoresists, Solvents, Developers and Etchants*, available online at https://www.microchemicals.com/downloads/application_notes.html, last accessed: 02/24/2023.

[70] G. W. TRUCKS, K. RAGHAVACHARI, G. S. HIGASHI, AND Y. J. CHABAL, *Mechanism of HF Etching of Silicon Surfaces: A Theoretical Understanding of Hydrogen Passivation*, Physical Review Letters **65**, 504 (1990).

[71] *Thin Film Technology - WMI/BAdW* (2020), available online at https://www.wmi.badw.de/research/Thin%20Film%20Technology, last accessed: 02/25/2023.

[72] I. V. TUDOSE, F. COMANESCU, P. PASCARIU, S. BUCUR, L. RUSEN, F. IACOMI, E. KOUDOUMAS, AND M. P. SUCHEA, in *Functional Nanostructured Interfaces for Environmental and Biomedical Applications*, Micro and Nano Technologies, edited by V. Dinca and M. P. Suchea (Elsevier, 2019) pp. 15–26.

[73] A. FALTERMEIER, *Optimierung supraleitender Schichten aus Niob, Niobnitrid und Niobtitannitrid für den Einsatz in Mikrowellenresonatoren*, Master's thesis, Technische Universität München, Garching (2019).

[74] *E-Beam Resist AR-P 6200-Serie (CSAR 62)* (2021), available online at https://www.allresist.de/portfolio-item/e-beam-resist-ar-p-6200-serie-csar-62/, last accessed: 02/20/2023.

[75] A. TSENG, K. CHEN, C. CHEN, AND K. MA, *Electron Beam Lithography in Nanoscale Fabrication: Recent Development*, IEEE Transactions on Electronics Packaging Manufacturing **26**, 141 (2003).

[76] *Entwickler AR 600-546*, available online at https://www.allresist.de/portfolio-item/entwickler-ar-600-546/, last accessed: 02/20/2023.

[77] S. FRANSSILA AND L. SAINIEMI, in *Encyclopedia of Microfluidics and Nanofluidics*, edited by D. Li (Springer US, Boston, MA, 2008) pp. 1772–1781.

[78] H. JANSEN, H. GARDENIERS, M. DE BOER, M. ELWENSPOEK, AND J. FLUITMAN, *A Survey on the Reactive Ion Etching of Silicon in Microtechnology*, Journal of Micromechanics and Microengineering **6**, 14 (1996).

[79] *Remover AR 600-71*, available online at https://www.allresist.de/portfolio-item/remover-ar-600-71/, last accessed: 02/20/2023.

[80] E. BEMPORAD, F. CARASSITI, M. SEBASTIANI, G. LANZA, V. PALMIERI, AND H. PADAMSEE, *Superconducting and Microstructural Studies on Sputtered Niobium Thin Films for Accelerating Cavity Applications*, Superconductor Science and Technology **21**, 125026 (2008).

[81] A. JUNG, *Development of Surface Acoustic Wave Resonators Based on Thin-Film Lithium Niobate for Circuit Quantum Acoustics Platforms*, Master's thesis, Technische Universität München, Garching (2022).

[82] S. WEICHSELBAUMER, *Spin Dynamics in Strongly Coupled Spin-Photon Hybrid Systems*, Ph.D. thesis, Technische Universität München, Garching (2020).

[83] C. M. YEN, L. E. TOTH, Y. M. SHY, D. E. ANDERSON, AND L. G. ROSNER, *Superconducting Hc-Jc and Tc Measurements in the Nb–Ti–N, Nb–Hf–N, and Nb–V–N Ternary Systems*, Journal of Applied Physics **38**, 2268 (1967).

[84] A. I. GUBIN, K. S. IL'IN, S. A. VITUSEVICH, M. SIEGEL, AND N. KLEIN, *Dependence of Magnetic Penetration Depth on the Thickness of Superconducting Nb Thin Films*, Physical Review B **72**, 064503 (2005).

[85] K. MAKI AND M. SAKURAI, *Microwave Response of Superconducting Thin Films in Magnetic Fields*, Journal of Low Temperature Physics **4**, 515 (1971).

[86] E. F. KUESTER, *Theory of Waveguides and Transmission Lines* (Taylor & Francis Group, Boca Raton, UNITED STATES, 2020).

[87] G. J. REDDY AND T. J. PRASAD, *Basics of Electromagnetics and Transmission Lines* (Taylor & Francis Group, Milton, UNITED KINGDOM, 2020).

[88] M. XU, X. HAN, W. FU, C.-L. ZOU, AND H. X. TANG, *Frequency-Tunable High-Q Superconducting Resonators via Wireless Control of Nonlinear Kinetic Inductance*, Applied Physics Letters **114**, 192601 (2019).

[89] S. K. YIP AND J. A. SAULS, *Nonlinear Meissner Effect in CuO Superconductors*, Physical Review Letters **69**, 2264 (1992).

[90] B. ABDO, E. SEGEV, O. SHTEMPLUCK, AND E. BUKS, *Nonlinear Dynamics in the Resonance Line Shape of NbN Superconducting Resonators*, Physical Review B **73**, 134513 (2006).

[91] J. WENNER, R. BARENDS, R. C. BIALCZAK, Y. CHEN, J. KELLY, E. LUCERO, M. MARIANTONI, A. MEGRANT, P. J. J. O'MALLEY, D. SANK, A. VAINSENCHER, H. WANG, T. C. WHITE, Y. YIN, J. ZHAO, A. N. CLELAND, AND J. M. MARTINIS, *Surface Loss Simulations of Superconducting Coplanar Waveguide Resonators*, Applied Physics Letters **99**, 113513 (2011).

[92] H. J. HOWE, *Stripline Circuit Design* (Artech House, 1974).

[93] C. POOLE AND I. DARWAZEH, *Microwave Active Circuit Analysis and Design*, illustrated edition ed. (Academic Press, San Diego, 2015).

[94] N. D. YORDANOV, *Is Our Knowledge about the Chemical and Physical Properties of DPPH Enough to Consider It as a Primary Standard for Quantitative EPR Spectrometry*, Applied Magnetic Resonance **10**, 339 (1996).

[95] P. BERTRAND, *Electron Paramagnetic Resonance Spectroscopy: Fundamentals* (Springer International Publishing, Cham, 2020).

[96] P. F. HERSKIND, A. DANTAN, J. P. MARLER, M. ALBERT, AND M. DREWSEN, *Realization of Collective Strong Coupling with Ion Coulomb Crystals in an Optical Cavity*, Nature Physics **5**, 494 (2009).

[97] S. S. EATON AND G. R. EATON, in *Biomedical EPR, Part B: Methodology, Instrumentation, and Dynamics*, Biological Magnetic Resonance, edited by S. R. Eaton, G. R. Eaton, and L. J. Berliner (Springer US, Boston, MA, 2005) pp. 3–18.

[98] G. FEHER AND E. A. GERE, *Electron Spin Resonance Experiments on Donors in Silicon. II. Electron Spin Relaxation Effects*, Physical Review **114**, 1245 (1959).

[99] J. P. GORDON AND K. D. BOWERS, *Microwave Spin Echoes from Donor Electrons in Silicon*, Physical Review Letters **1**, 368 (1958).

[100] W. KESTER AND A. D. INC, *Data Conversion Handbook* (Newnes, 2005).

[101] L. M. PHAM, N. BAR-GILL, D. LE SAGE, C. BELTHANGADY, A. STACEY, M. MARKHAM, D. J. TWITCHEN, M. D. LUKIN, AND R. L. WALSWORTH, *Enhanced Metrology Using Preferential Orientation of Nitrogen-Vacancy Centers in Diamond*, Physical Review B **86**, 121202 (2012).

[102] M. A. NIELSEN AND I. L. CHUANG, *Quantum Computation and Quantum Information: 10th Anniversary Edition*, 10th ed. (Cambridge University Press, Cambridge ; New York, 2010).

[103] H. MALISSA, D. I. SCHUSTER, A. M. TYRYSHKIN, A. A. HOUCK, AND S. A. LYON, *Superconducting Coplanar Waveguide Resonators for Low Temperature Pulsed Electron Spin Resonance Spectroscopy*, Review of Scientific Instruments **84**, 025116 (2013).

[104] A. M. TYRYSHKIN, S. A. LYON, A. V. ASTASHKIN, AND A. M. RAITSIMRING, *Electron Spin Relaxation Times of Phosphorus Donors in Silicon*, Physical Review B **68**, 193207 (2003).

[105] E. M. PURCELL, H. C. TORREY, AND R. V. POUND, *Resonance Absorption by Nuclear Magnetic Moments in a Solid*, Physical Review **69**, 37 (1946).

[106] F. BLOCH, W. W. HANSEN, AND M. PACKARD, *Nuclear Induction*, Physical Review **69**, 127 (1946).

[107] D. D. LAWS, H.-M. L. BITTER, AND A. JERSCHOW, *Solid-State NMR Spectroscopic Methods in Chemistry*, Angewandte Chemie International Edition **41**, 3096 (2002).

[108] T. D. W. CLARIDGE, *High-Resolution NMR Techniques in Organic Chemistry* (Elsevier, 2016).

[109] A. W. OVERHAUSER, *Polarization of Nuclei in Metals*, Physical Review **92**, 411 (1953).

[110] M. STEGER, K. SAEEDI, M. L. W. THEWALT, J. J. L. MORTON, H. RIEMANN, N. V. ABROSIMOV, P. BECKER, AND H.-J. POHL, *Quantum Information Storage for over 180 s Using Donor Spins in a 28Si "Semiconductor Vacuum"*, Science **336**, 1280 (2012).

[111] D. R. MCCAMEY, J. VAN TOL, G. W. MORLEY, AND C. BOEHME, *Electronic Spin Storage in an Electrically Readable Nuclear Spin Memory with a Lifetime >100 Seconds*, Science **330**, 1652 (2010).

[112] S. FREER, S. SIMMONS, A. LAUCHT, J. T. MUHONEN, J. P. DEHOLLAIN, R. KALRA, F. A. MOHIYADDIN, F. E. HUDSON, K. M. ITOH, J. C. MCCALLUM, D. N. JAMIESON, A. S. DZURAK, AND A. MORELLO, *A Single-Atom Quantum Memory in Silicon*, Quantum Science and Technology **2**, 015009 (2017).

[113] S. MAHASHABDE, E. OTTO, D. MONTEMURRO, S. DE GRAAF, S. KUBATKIN, AND A. DANILOV, *Fast Tunable High- Q -Factor Superconducting Microwave Resonators*, Physical Review Applied **14**, 044040 (2020).

[114] N. DERBY AND S. OLBERT, *Cylindrical Magnets and Ideal Solenoids*, American Journal of Physics **78**, 229 (2010).

[115] T. PECK, R. MAGIN, J. KRUSE, AND M. FENG, *NMR Microspectroscopy Using 100 Mm Planar RF Coils Fabricated on Gallium Arsenide Substrates*, IEEE Transactions on Biomedical Engineering **41**, 706 (1994).

[116] C. MASSIN, G. BOERO, F. VINCENT, J. ABENHAIM, P. A. BESSE, AND R. S. POPOVIC, *High-Q Factor RF Planar Microcoils for Micro-Scale NMR Spectroscopy*, Sensors and Actuators A: Physical Selected Papers from Eurosenors XV, **97–98**, 280 (2002).

[117] Q.-M. Chen, P. Singh, R. Duda, G. Catto, A. Keränen, A. Alizadeh, T. Mörstedt, A. Sah, A. Gunyhó, W. Liu, and M. Möttönen, *Compact Inductor-Capacitor Resonators at Sub-Gigahertz Frequencies* (2023), arxiv:2304.12744 [physics, physics:quant-ph] .

[118] M. Gupta and P. Agarwal, in *2017 International Conference on Inventive Computing and Informatics (ICICI)* (2017) pp. 490–494.

[119] A. Schneider, T. Wolz, M. Pfirrmann, M. Spiecker, H. Rotzinger, A. V. Ustinov, and M. Weides, *Transmon Qubit in a Magnetic Field: Evolution of Coherence and Transition Frequency*, Physical Review Research **1**, 023003 (2019).

Acknowledgements/Danksagung

Das vergangene Jahr, in welchem ich am WMI diese Arbeit machen durfte, war zu großen Teilen sehr anstrengend und leider auch von tiefen persönlichen Krisen gezeichnet. Ich möchte mich im Folgenden bei den Personen an und außerhalb des WMIs bedanken, die direkt und indirekt maßgeblich dazu beigetragen haben, dass diese Arbeit so entstehen konnte. Ich bitte um Entschuldigung, falls ich jemanden vergessen haben sollte. Danke an:

- **Prof. Rudolf Gross**, der mich damals beim Proseminarvortrag betreut und anschließend den Kontakt zu den einzelnen Arbeitsgruppen des WMIs hergestellt hat, wodurch diese Arbeit zustande kam.

- **Dr. Hans Hübl**, der mir das Vertrauen schenkte und mir diese spannende Masterarbeit über supraleitende Mikrowellenresonatoren anvertraute. Danke, dass du auch immer prinzipiell ein offenes Ohr hattest für alle Angelegenheiten und Probleme. Deine Ratschläge und Korrekturen haben mir immer sehr geholfen.

- **Patricia Oehrl**, die unermüdlich diese Arbeit mitbetreut hat. Patricia, danke dass du mich immer gefordert und gefördert hast. Deine offene, akribische, freundliche und immer lösungsorientierte Art hat mich stets motiviert und dafür gesorgt, das Beste aus mir rauszukitzeln. Herzlichen Dank auch dafür, dass ich immer mit dir offen über alles reden kann, mit und ohne Bezug zur Arbeit. Das ist alles andere als selbstverständlich und es tat ganz besonders in dunklen Momenten unfassbar gut zu wissen, dass da jemand ist, der einen versteht. Ich hoffe, dass ich auch etwas zurückgeben konnte.

- **Manuel Müller**, der mich in die Fabrikation eingelernt hat und bei sämtlichen Transportmessungen half. Danke, dass du immer einen Ratschlag hattest, wenn beispielsweise die wunderbare ULTRADISK ihr Ding abgezogen hat. Auch hat dein Sarkasmus in wohldosierten Mengen stets für Erheiterung gesorgt, auch wenn einem eigentlich nicht zum Lachen war.

- **Thomas Luschmann**, der immer für Fragen zur Fabrikation, Resonatorfitting und insbesondere Angelegenheiten mit der Nanobeam erreichbar war.

- **Dr. Matthias Althammer**, der immer bei Problemen mit der ULTRADISK und Kryostaten half.

- **Leon Koch und Niklas Bruckmoser**, die zufälligerweise immer in der Nähe waren, wenn es Probleme im Reinraum gab.

- **Kedar Honasoge** for numerous HF dips.

- **Monika Scheufele und Korbinian Rubenbauer**, die auch immer für Fragen und nette Unterhaltungen verfügbar waren.
- **Das technische Personal des WMI**, das täglich das Institut versorgt.
- **Alexander Jung**, der immer offen für die aktuellen Probleme war und sie mitunter annahm, als seien sie seine eigenen. Vielen Dank für deine Hilfsbereitschaft und viel Erfolg in Schweden.
- **Lukas Niekamp**, mit dem ich auch über alles reden konnte, vor allem, wenn wir beide mal wieder vom Laboralltag frustriert waren. Danke für all die guten Gespräche.
- **Marius Strassner**, der zwar nur begrenzte Zeit hier war, in dieser jedoch zu einem guten Freund wurde.
- **Franz Weidenhiller, Johannes Weber, Maria Sigl und Christian Mang**, die immer Zeit hatten für einen Plausch zwischendurch, der oftmals in Memes ausgeartet ist. Danke für all die zahlreichen Gespräche und Lacher, die so wichtig sind vor allem dann, wenn wenig funktionierte.
- **Franziska Wilfinger, Catharina Broocks, Florian Kollmannsberger, Owen Huisman, Jan Wozniak, Florian Maier, Raphael Hoepfl, Julius Feigl und Georg Mair**, mit denen ich ein großes Büro teilen durfte. Danke für all die guten Unterhaltungen, Lacher und dass ihr meinen Schmarrn und die Memes ausgehalten habt.
- Meine guten Freunde **Konstantin Seidenfus, Patrick Missale, Clemens Lippmann, Julian Rumpfinger und Adrian Wittmeier**, die für dringend nötige Ablenkung beim wöchentlichen Stammtisch und zwischendurch sorgten und auch immer ein offenes Ohr hatten, wenn es mir schlecht ging oder ich sehr frustriert war.
- **Petra Lindig und Silvia Seebauer**, die für den viel zu oft benötigten seelischen Beistand sorgten. Durch eure Worte konnte ich oftmals wieder Hoffnung schöpfen, als ich sehr mit mir zu kämpfen hatte. Von Herzen Danke dafür!
- Meinen Opa **Erich Seider**, der immer an mich geglaubt hat. Opa ist innerhalb des Zeitraums der Masterarbeit nach langer, schwerer Krankheit im hohen Alter von 84 Jahren verstorben. Ich weiß, wie gerne du noch diesen Abschluss deines "Professors" miterleben wolltest, aber ich weiß, dass du mich durch die restliche Zeit begleitet hast und von oben stolz auf mich herab blickst. Ruhe in Frieden.
- Meinen **Vater**, der nach seinen Möglichkeiten vermehrt versucht hat für mich da zu sein und mich zunehmend besser versteht. Danke, dass du immer an mich geglaubt hast.
- Die wohl wichtigsten Menschen in meinem Leben, meine **Mutter** und meine **Schwester**. Worte können nicht beschreiben wie unendlich dankbar ich bin, dass ich euch habe. Ihr habt auch immer an mich geglaubt, meine Sorgen und Ängste angehört und versucht zu helfen wo es nur ging, besonders in den dunkelsten Stunden, die es leider viel zu oft gab. Ohne euch würde ich heute nicht hier stehen. Von ganzem Herzen, DANKE!